FACULTY OF SCIENCE
DEPARTMENT OF CHEMISTRY
MOLECULAR IMAGING AND PHOTONICS
Celestijnenlaan 200D box 2425
B-3001 HEVERLEE, BELGIUM

Thien Tai Luong

KU LEUVEN
ARENBERG DOCTORAL SCHOOL
FACULTY OF SCIENCE

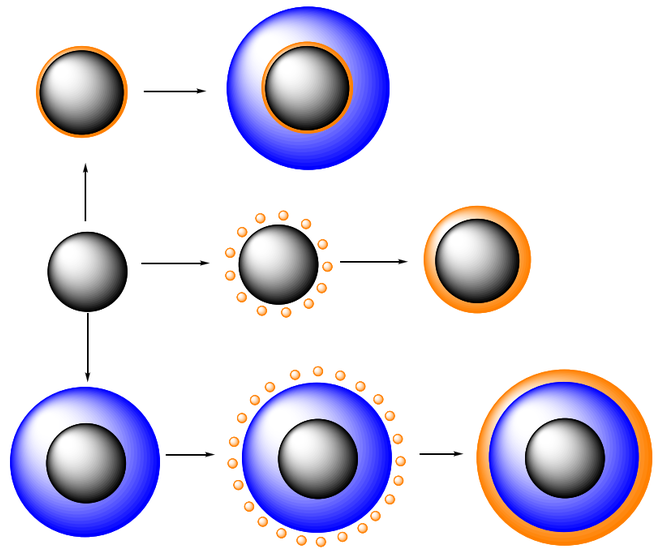

IRON OXIDE BASED MULTIFUNCTIONAL CORE-SHELL NANOPARTICLES FOR BIOMEDICAL APPLICATIONS

Iron oxide based multifunctional core-shell nanoparticles for biomedical applications

Thien Tai Luong

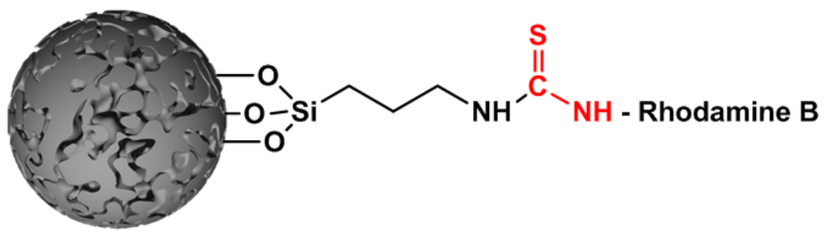

August 2016

Dissertation presented in partial fulfilment of the requirements for the degree of Doctor in Science

August 2016

Iron oxide based multifunctional core-shell nanoparticles for biomedical applications

Thien Tai Luong

Examination committee:
Prof. Dr. S. De Feyter, chair
Prof. Dr. T. Verbiest, promoter
Dr. S. Knoppe, co-promoter
Prof. Dr. K. Clays
Prof. Dr. G. Koeckelberghs
Prof. Dr. T. Vogt
Prof. Dr. M. Van der Veen (TU Delft)

Dissertation presented in partial fulfillment of the requirements for the degree of Doctor in Science

August 2016

Preface

Pursuing a PhD is a great adventure and is the most difficult task that I have been faced. Three first years of my PhD are the best time when I was excited to explore new things, learned many techniques and operated myself some really big machines such as Vibrating Sample Magnetometer (VSM), Scanning Electron Microscopy (SEM) and Transmission Electron Microscopy (TEM). That feeling is really great. When the time was running out, the fourth year turned more stressful. More and more experiments were carried on but little positive results came out. Sometimes I thought that it was very close to the goal, and then things turned down. In that case, there is the only way to overcome all touch challenges: be patient and keep hard working. One more thing, I was very lucky to receive many help from people around and I would like to seize this opportunity to say thanks to everyone.

First and foremost, I would like to thank Prof. Thierry Verbiest for his talented guidance, big encouragement and unconditional finance supports. He is always able to find the smallest positive things and encourage me a lot. These are very meaningful to me. For me, he is simply the nicest professor.

I would like to send the special thanks to my co-promoter, Dr. Stefan Knoppe. Absolutely, I could not have finished my PhD without his help. I learned a lot from him. Also thanks for very careful proof reading.

I also would like to express my gratitude to the jury members: Prof. Steven De Feyter (KU Leuven), Prof. Koen Clays (KU Leuven), Prof. Guy Koeckelberghs (KU Leuven), Prof. Tatjana Vogt (KU Leuven) and Prof. Monique van der Veen (TU Delft). Thanks for valuable comments and remarks that help me a lot to improve my dissertation.

I also received many helps from my colleagues, especially Maarten Bloemens, Ward Brullot, Stijn van Cleuvenbergen and Pieter-Jan Demeyer, from the first day till the last day. For Maarten, he is very generous to provide me the starting sample. For Ward, working together, chatting and discussing in the lab at the end of a working day

were so funny and fantastic. For Stijn van Cleuvenbergen, thanks for all nonlinear measurements and all ping pong games. Thanks PJ and Griet Depotter for sharing many good moments in our office.

Here in Leuven, I am very happy to spend the best time of my youth with my family and my beloved friends. I would like to say thanks to all for sharing sweet memories that I will keep deeply in my heart. Thank Mr. Cao The Anh, Mr. Pham Huy Hoang, Mr. Vu Ngoc Duy, Mr. Nguyen Cuong Luat, Mr. Nguyen Hoang Hai – all my "big brother" – who I learned the spirit of "work hard and play hard". Thank Mrs. Le Bich Ngoc and Mrs. Le Thi Hang for treating me so well with delicious foods. Many thanks sending to Mr. Ho Le Tuan Anh, Mrs. Dinh Thi Oanh, Mr. Duong Van Tu, Mr Tran Minh Cuong for the truly friendship. Also many thanks to VFC (VinaKUL Football Club). Last but not least, a thousand times of thanks I would love to send to my parents, my wife and my kids for being beside me in all difficult time as well as happy moments. I cannot wait more to see you again.

Thank you all !!!

Abstract

Iron oxide nanoparticles have been intensively studied in biomedical applications because of their low toxicity, biocompatibility and their high response to an external magnetic field. Recently, such particles are considered as potential candidates for many advanced applications such as hyperthermia, magnetically guided drug delivery and release and theranostic nanomedicines. However, most of these studies are ended at the preclinical step due to the limitations of current nanomaterials and numerous challenges at different stages of the development of these nanomaterials. So, the search of new versatile nanostructures which might be exploited in human therapy is urgent.

In this dissertation, we focus on the functionalization of iron oxide-based nanoparticles and the utilization of the obtained multifunctional core-shell nanostructures for several biomedical applications.

In the first part, we study the functionalization of iron oxide nanoparticles with various coating agents. The functionalization renders particles water-dispersible and provides functional moieties such as polyethylene glycol, carboxyl and amino groups, gold and silica shells, and fluorescent tags. With a wide range of functionalities, the particles are beneficial for various purposes. Carboxyl-functionalized iron oxide nanoparticles were studied as bio-entity coupling agents while amine functionalization was used as a first step for gold coating preparation.

Core-shell nanostructures possess many interesting properties as compared with single compositions because of the interaction between each component. Therefore, we synthesized (multilayer) core-shell nanoparticles in order to combine several functions into one single structure: magnetic properties, plasmonic properties, mesoporous silica properties and fluorescent properties. In particular, we investigated the utilization of these core-shell nanostructures as drug release carriers. The payload was covalently bound to the particles, then its controlled release was induced by an oscillating magnetic field. Finally, we describe the utilization of the core-shell nanoparticles as nonlinear optical imaging agent.

Samenvatting

Ijzeroxide nanodeeltjes kennen heel wat biomedische toepassingen. Met hun lage toxiciteit, biocompatibiliteit en superparamagnetische eigenschappen kunnen ze beschouwd worden als potentiële kandidaten voor toepassingen zoals magnetisch geïnduceerde hyperthermie en magnetische drug delivery. De laatste jaren is er dan ook heel wat onderzoek verricht in dit domein, maar de meeste studies worden echter beëindigd bij de preklinische stap als gevolg van de beperkingen van de huidige nanomaterialen en talrijke uitdagingen in verschillende stadia van de ontwikkeling van deze nanomaterialen. Dus, de zoektocht naar nieuwe veelzijdige nanostructuren die kunnen gebruikt worden voor biomedische toepassingen is zeer actueel en relevant.

In dit proefschrift richten we ons in eerste instantie op de functionalisering van ijzeroxide gebaseerde nanodeeltjes om multifunctionele kern-schil nanostructuren te bereiden voor meerdere biomedische toepassingen. We bestudeerden de functionalisering van ijzeroxide nanodeeltjes met diverse materialen zoals polyethyleenglycol, carboxyl- en aminogroepen, goud en silica schillen, en fluorescerende labels. Het maakt de deeltjes niet alleen waterdispergeerbaar maar levert ook verschillende andere functionaliteiten. Kern-schil nanostructuren combineren immers niet alleen de eigenschappen van de samenstellende materialen, maar kunnen ook nieuwe eigenschappen vertonen. In dit werk ontwikkelden wij kern-schil nanostructuren die magnetische, plasmonische, mesoporeuze en fluorescerende eigenschappen combineren. Dit illustreerden we vervolgens mbv twee toepassingen, nl. magnetisch gecontroleerde drug release en multifoton visualisatie.

Abbreviations

2-PF	two photon fluorescence
acac	acetylacetonate
APTMS	(3-aminopropyl)trimethoxysilane
BSA	Bovine serum albumin
COOH-silane	(Trimethoxysilylpropyl)ethylenediaminetriacetic acid trisodium salt
CTAB	Cetyltrimethylammonium bromide
cup	N-nitrosophenylhydroxylamine
DLS	Dynamic light scattering
EDC	1-Ethyl-3-(3-dimethylaminopropyl)carbodiimide
ESI	Electronic supplementary information
FDA	Food and Drug Administration
FITC	Fluorescein isothiocyanate
HRS	Hyper-Rayleigh scattering
LSPR/SPR	(Localized) surface plasmon resonance
MES	2-(N-morpholino)ethanesulfonic acid
MFNPs	Magneto-fluorescent nanoparticles
mp-SiO_2	Mesoporous silica
MNP	Magnetic nanoparticle
MRI	Magnetic resonance imaging
MS	Magnetic separation
MSNPs	Mesoporous nanoparticles
MuNPs	Multifunctional nanoparticles

NHS	N-hydroxysuccinimide
NLO	Nonlinear optical
NPs	Nanoparticles
PEG	Polyethylene glycol
PEG-silane	Methoxy(polyethyleneoxy)propyltrimethoxysilane (9-12 PE-units)
Rho-MNPs	Rhodamine B functionalized iron oxide/mesoporous silica core/shell nanoparticles
RITC	Rhodamine B isothiocyanate
SONLO	Second-order nonlinear optical
SQUID	Superconducting quantum interference device magnetometer
SEM	Scanning electron microscopy
SHG	Second-harmonic generation
SI	Supporting information
TEOS	tetraethylorthosilicate
TEM	Transmission electron microscopy
THF	Tetrahydrofuran
THPC	tetrakis(hydroxymethyl)phosphonium chloride
THS	Third-harmonic scattering
UV–Vis	Ultraviolet-Visible
VSM	Vibrating sample magnetometry
ZP	Zeta potential

Table of contents

Chapter 1

General introduction to magnetic core-shell nanoparticles and their biomedical applications

Today, the development of economics and science enables people to explore new lands, going deep underground, flying into space to seek life beyond the Earth and investigate small particles like atoms, molecules, nano-sized materials. We talk about new technology every day: smartphones, laptops, self-driving cars, and some of them have drastically changed the way we are living. However, the cost we have to pay is unsustainable development, especially in the third world countries, resulting in many environmental disasters including global warming, air pollution, water pollution. Consequently, people also face both old and new health problems. There are still many incurable diseases (Ebola, HIV/AIDS, cancer), new viruses (or virus evolution) and contagious diseases. One of the most dangerous diseases is cancer, and many research efforts have been devoted to curing cancer.

In this chapter, we will briefly discuss cancer and applications of nanotechnology (particularly magnetic core-shell nanoparticles) in biomedicine in general and cancer treatment in particular. Because these advanced applications rely on the unique properties of multifunctional nanoparticles (MuNPs), the structure of MuNPs and their properties will also be presented. At the end of this chapter, we give an overview of several characterization methods of nanomaterials.

Generally, this dissertation focuses on the design of different types of MuNPs based on a magnetic iron oxide core, various nanoshells and functionalization. Several applications of MuNPs in the biomedical field were also explored, suggesting that these materials can be potential candidates for future applications in disease/cancer

diagnostic and therapy such as biomedical imaging or drug delivery and release. First of all, we need to know what is cancer and why cancer is so dangerous?

1.1 Overview of cancer

What is cancer?

Cancer is a very common condition and a serious health problem. It is estimated that more than one in three people will develop some forms of cancer during their life [1]. So what is cancer? Cancer is a group of diseases that all share an uncontrolled division of abnormal cells in some part of the body. Normally, cells in the body grow and divide for a certain time and then stop growing and dividing. They only reproduce themselves when the body needs them, for example, for replacement of old cells. In the case of cancer, the cancer cells are able to ignore signals that tell the cells to stop dividing and therefore these cells grow and reproduce in an uncontrolled manner. They can then invade other normal tissues and organs, and eventually spread throughout the body. The extra cells caused by cancer may form tumors. Based on the characteristics of tumors, we can classify cancer into 2 types: malignant tumors and benign tumors.

Type of cancer: malignant tumor and benign tumor

Cancer can start almost everywhere in the human body, so there are over a hundred distinct types of cancer, which are mainly different in their behavior and response to treatment. Most cancers form masses of tissue called tumors (except in case of leukemias). A tumor can come in two forms: benign and malignant. A benign tumor is a cancerous tumor that remains confined to its original location and demonstrates limited growth. It does not spread into, or invade nearby tissues. Benign tumors are usually not life threatening. They may be removed surgically. After being removed, they usually do not grow back.

A malignant tumor, however, is able to invade and spread to surrounding normal tissue, resulting in destruction of healthy tissue and organs. In addition, the capability of traveling from the initial tumor site to other parts of the body known as metastasis makes malignant tumors resistant to localized treatments such as surgery. Therefore, they become more dangerous.

Although there are many kinds of cancer, only a few occur frequently (Table 1.1). Cancers of 10 different body sites account for more than 75% of all cancers.

How dangerous is cancer?

To illustrate how dangerous cancer is, one could consider the following data: Every year, more than a million cases of cancer are diagnosed in the United States, and the number of Americans that die of cancer can reach 500,000 [2]. In an estimate, 196,900 new cases of cancer and 78,000 deaths from cancer occurred in Canada in 2015.

Table 1.1: Ten Most Frequent Cancers in the United States (source: American Cancer Society, Cancer Facts and Figures—2000 [2]).

Cancer site	Cases per year	Deaths per year
Breast	184,200 (15.1%)	41,200 (7.5%)
Prostate	180,400 (14.8%)	31,900 (5.8%)
Lung	164,100 (13.4%)	156,900 (28.4%)
Colon/rectum	130,200 (10.7%)	56,300 (10.2%)
Lymphomas	62,300 (5.1%)	27,500 (5.0%)
Bladder	53,200 (4.4%)	12,200 (2.2%)
Uterus	48,900 (4.0%)	11,100 (2.0%)
Skin (melanoma)	47,700 (3.9%)	7,700 (1.4%)
Kidney	31,200 (2.6%)	11,900 (2.2%)
Leukemias	30,800 (2.5%)	12,100 (2.2%)
Subtotal	933,000 (76.5%)	368,800 (66.8%)
All sites	1,220,100 (100%)	552,200 (100%)

Cancer is the leading cause of death in Canada and is responsible for 30% of all deaths (see Fig. 1.1) [3]. In Vietnam, 110,000 new cases of cancer are reported annually with death rate of 73 % - one of the highest rates in the world. According to WHO, the world's average mortality rate of cancer patients is just 59.7 %: the average death rate in the developing countries is 67.8 % whereas in developed countries, it is much lower, only 49.4 % [4].

Why is cancer so dangerous?

There are four main reasons why cancer is a deadly disease:

i) Invading normal tissues and organs: The rapid and uncontrollable growth of cancer cells, leads to less room for the cells we need (e.g., red and white blood cells). Furthermore, the tumor also uses a lot of blood, and as a consequence the hemoglobin in the blood can decrease drastically.

ii) Metastasis: Metastasis is a process whereby cancer cells travel from the initial tumor site to other parts of the body. This spread of cancer cells make cancer become a more serious health problem. For example: initially, melanoma (see Fig. 1.2, a cancer of pigmented cells) can arise in the skin, but some of the cancer cells can enter the bloodstream and spread to distant organs such as the liver or brain. Cancer cells in the liver would be called metastatic melanoma, not liver cancer. Melanoma cells growing in the brain or liver can disrupt the functions of these vital organs and are potentially life threatening:

iii) The limitation of current treatments: Current treatments including chemotherapy, radiation therapy, surgery, gene therapy, immunotherapy face many difficulties because of the metastasis of cancer. These therapies, if successful, might

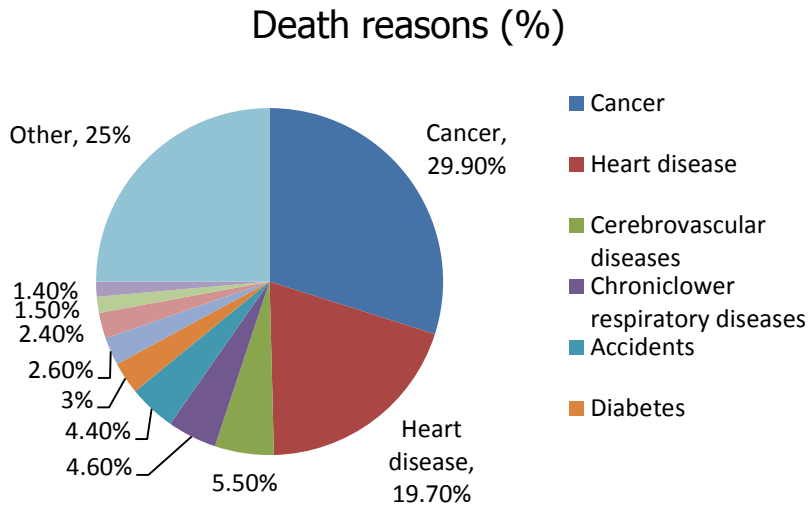

Figure 1.1: Proportion of deaths due to cancer and other causes, Canada, 2011.

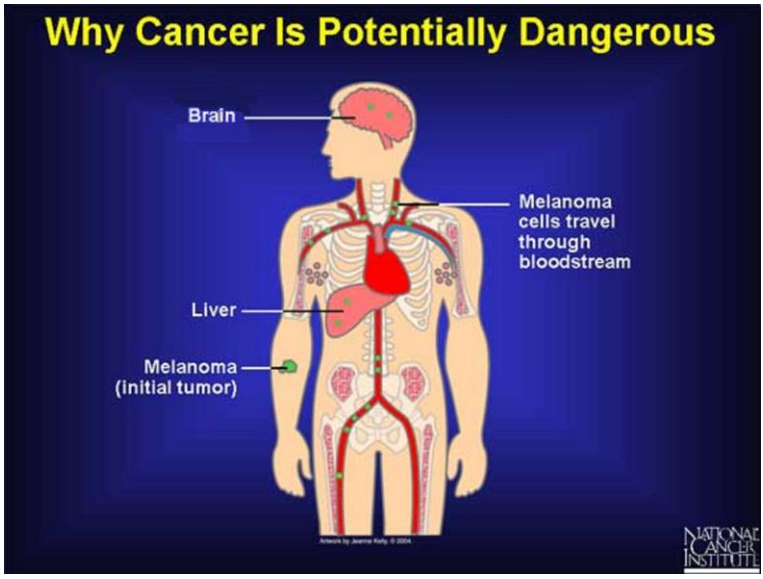

Figure 1.2: Cancer cells (green dots) of a tumor, arising in the skin, can enter the blood stream and spread to distant parts of the body such as liver, brain (source: national cancer institution, USA, www.cancer.gov).

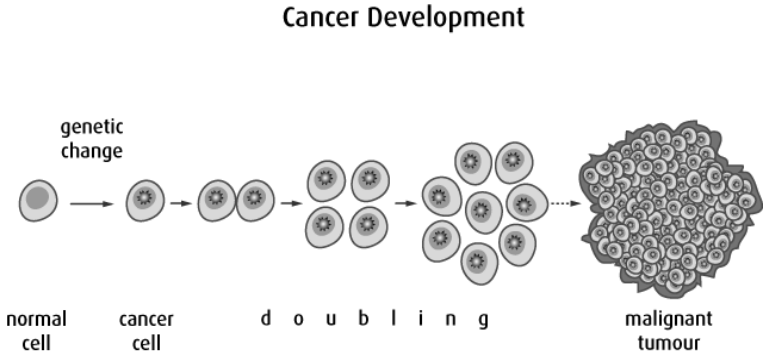

Figure 1.3: Schematic of cancer development. Cancer starts when normal cells undergo a genetic change when they are exposed to a cancer risk, then each cancer cell is divided incessantly into two cancer cells and group together to form a tumor. Source: Canadian cancer society (www.cancer.ca).

extend the life time of patients but we never know whether cancer will come back again one day when the metastatic cells grow to become a tumor somewhere in the body. In addition, these treatments are not specific. They do not only kill cancer cells but also kill healthy cells and tissue.

iv) Late diagnosis: generally, a long time is required for cancer to develop. The period between the exposure to a carcinogenic agent and cancer actually developing is usually many years (up to 30 years). This time frame is called the latency period, or lag time. On the contrary, when the number of cancer cells is large enough, cancer cells grow very fast. Therefore, the early stage of cancer quickly turns to the late stage. For this reason, when someone is diagnosed with cancer, he/she might be in the final stages of cancer with a large number of cancer cells in the body. Therefore, the treatment is often not as efficient as expected.

1.2 How nanotechnology can help with therapeutic applications

1.2.1 Tumor targeting agents – a powerful tool of nanotechnology

As mentioned above, the difficulties in cancer treatment are not only the requirement for specific medicines but also a low efficiency of the treatment. Current treatments

Table 1.2: FDA approved cancer targeting antibodies and small molecules

Name	Brand name	Type	Cancer type
Bevacizumab	Avastin	Antibody	Colorectal, breast non-small cell lung,
Trastuzumab	Herceptin	Antibody	Breast
Tositumomab	Bexxar	Antibody	Lymphoma
Rituximab	Rituxan	Antibody	Lymphoma
Imatinib	Gleevec	Small molecules	Leukemia, Gastrointestinal
Bortezomib	Velcade	Small molecules	Myeloma, Lymphoma
Gefitinib	Iressa	Small molecules	Non-small cell lung
Sorafenib	Nexavar	Small molecules	Kidney, liver
Tamoxifen	Nolvadex	Small molecules	Breast

include surgery chemotherapy, radiation therapy, gene therapy, hyperthermia, immunotherapy, but each method has its own limitations [5], [6]. The main limitations of current cancer therapies are that they are far too invasive, painful, toxic and associated with too many acute and chronic side effects. Furthermore, the biggest drawback of cancer diagnostics and therapy is that healthy tissues surrounding the tumor are also affected by treatment, leading to a weakened immune system. In fact, there are many cases where the cancer patients die shortly after their cancer treatment because the immune system is severely weakened.

For this reason, the most important requirement is the design of tumor targeting agents that can carry drugs directly and specifically to tumors. In this way, the treatment does not need a large dose of drugs and the healthy tissues do not significantly suffer from the treatment.

To achieve this goal, cancer cells need to be identified among trillions of healthy cells in the body. In other words, very specific binding between cancer cells and therapeutic agents is required. At the beginning of the 20th century, Paul Ehrlich defined the term “magic bullet” referring to the ability of an antibody to specifically target the surface of cells with great specificity [7]–[9]. Ideally, a ‘‘magic bullet’’ consists of a nanometer-sized delivery platform that is able to specific the targeting cancer cells, avoiding premature fragmentation and degradation [10]. The platform also facilitates the delivery of concentrated drug across the cell membrane. Thanks to the development of nanotechnology, nowadays antibody conjugated MuNPs can be used widely as tumor targeting agents because of the specific interaction between antibodies and antigens in cancer cells. Similar to the key-lock situation where only one key is able to open the lock, the antibody would exclusively and specifically bind to the

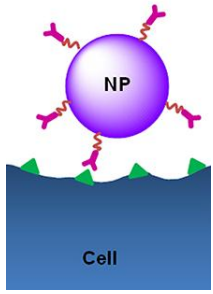

Fig. 1.4: A schematic representing the specific interaction between nanoparticle-bound antibodies and cancer cells. Reprinted with permission from Ref. [9].

tumor [11] (see Fig. 1.4). The specificity of the binding is due to the specific chemical composition of each antibody. Antigens are bound to antibodies through weak and non-covalent bonds such as electrostatic interactions, hydrogen bonds, Van der Waals forces, and hydrophobic interactions [12].

It is worth to note that some small molecules also have the same function as antibodies in cancer targeting. Table 1.2 shows some of the cancer targeting antibodies/small molecules approved for use in human cancer therapy by the Food and Drug Administration (FDA) [13]. Besides cancer, this method is also applied widely for other diseases and many commercial products based on antibodies were approved by the FDA for human therapy [14].

For all reasons mentioned above, the tumor targeting nanoparticles play a key role in highly efficient therapeutic applications. Antibodies are linkers to connect cancer cells and nanoparticles (NPs), whereas the different components of the NPs play exhibit many functions, such as providing contrast for imaging, act as a drug delivery/release platform, or act as a therapeutic agent. To achieve this multifunctionality, nanoparticles of the core-shell type should be ideal. These structures will be discussed in the next section, followed by an overview of the applications of tumor targeting antibody MuNPs in cancer diagnostic and therapy.

1.2.2 Multifunctional nanoparticles

Nanomaterials are defined as materials with at least one external dimension in the range of 1-100 nanometers [15]. Nanoparticles are objects with all three external

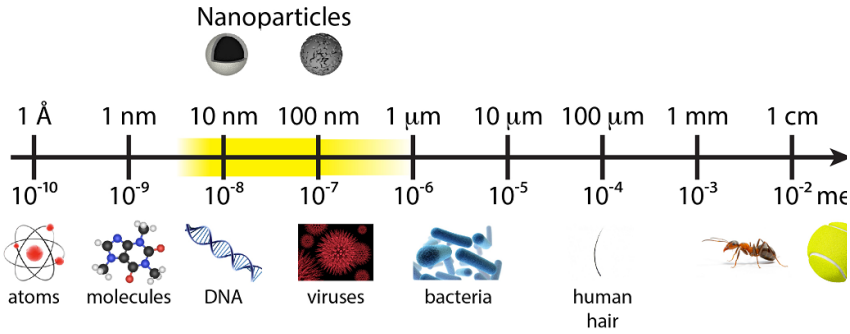

Fig. 1.5: One dimension of a nanomaterial should be in the 1-100 nm range. As a comparison, other typical sizes of everyday objects and organisms are shown. Reprinted with permission from Ref. [15].

dimensions at the nanoscale. Fig. 1.5 shows the size range of nanoparticles in comparison with other well-known objects such as atoms, molecules, viruses and bacteria. The most important characteristics, among many others, on the nanoscale are as follows: First, the small size of the particles leads to physical properties that are governed by quantum phenomena [16]. Second, the increasing surface area to volume ratio leads to an increase in the dominance of the surface atoms of the nanoparticle over those in its interior.

Advanced applications of NPs require multifunctional nanoparticles – particles that exhibit different functions. For example, MuNPs in biomedical applications can be utilized for many purposes such as an imaging agent, a targeting agent and a therapeutic medicine. These particles are often composed of large NPs ($\leq$ 100 nm) at the center and functional moieties/molecules/shells which are conjugated to NPs. Using large particles allows particles to carry many functional components. Moreover, in some cases, bare NPs themselves can also possess many interesting properties and acts as a functional component. Some typical bare NPs are magnetic iron oxide nanoparticles (IONPs), plasmonic gold NPs and mesoporous silica NPs.

The first studies of nanomaterials started with single (metallic/metal oxide) NPs because these particles showed different properties than bulk materials. Later, scientists found that certain types of semiconductor composite NPs performed much better in comparison with the single semiconductors [17]–[19]. These results opened a new chapter of nanomaterials in which the combination of two or more components can lead to the enhancement of their single components and develop new properties in some cases [20], [21]. There are many ways to combine different components into one nanostructure, however core-shell nanostructures have been given much more

attention because the maximal interaction between components is achieved in this kind of structure.

Core–shell nanomaterials have a combination of different properties from different material compositions in a single particle. Therefore, this kind of nanostructure can offer multifunctionality. They represent a novel class of hybrid materials, where composition and structure vary in the radial direction [22]. The addition of nanoshells brings a number of possibilities and opportunities for different purposes. Some of the direct benefits are:

- *Protection:* The presence of the shell can protect the core from environmental effects, especially in cases where the core is very sensitive [23]–[25]. The protection is also required when the cores are toxic (e.g., quantum dot, cobalt NPs). In these cases, nanocores are coated by biocompatible ligands in order to reduce their toxicity [26], [27].
- *Reduction of nanomaterial cost*: Expensive nanomaterials can be formed as shells around inexpensive core nanomaterials. This is particularly useful in catalysis [28], [29].
- *Enhancement of the properties of single components*: The dimensions and composition of the shell can be modulated in order to influence the properties of the core and similarly the core dimensions can be modulated to influence the properties of the shell [20], [30]–[32].
- *Surface bio-functionalization*: The formation of nanoshells like silica enables versatile ways to achieve the surface bio-functionalization that might be difficult or impossible to perform on a core surface [25], [33], [34].

More importantly, multiple functions such as detection and treatment modalities or multiple treatment options can be incorporated in a single core–shell particle [35], [36]. Although MuNPs are potential candidates for highly efficient human therapy, utilization of multifunctional core-shell NPs is relatively new. So far, many *in vitro* and *in vivo* experiments were carried out and showed promising results, but most of them have stopped at preclinical trials [5], [7], [11]. There are only few clinical trials reported, including the utilization of IONPs coated with aminosilane for hyperthermia treatment of tumors (MagForce Nanotechnologies AG, German company).

For these reasons, utilization of MuNPs for biomedical applications in general and cancer theranostics in particular has been a hot topic and there is still a lot of room for development and improvement. Fig. 1.6 shows a possible structure of functionalized core-shell NPs for biomedical applications [9]**.** Depending on the application, different kinds of functionalities can be incorporated into a nanoparticle. For example, the stealth property of polyethylene glycol (PEG) can help to improve the biocompatibility of the NPs and it also increases the circulation time of the NPs [37], [38]. The incorporation of an imaging contrast agent (MRI, fluorescent, radionuclide agents) into NPs allows the nanostructures to be tracked by imaging techniques [7],

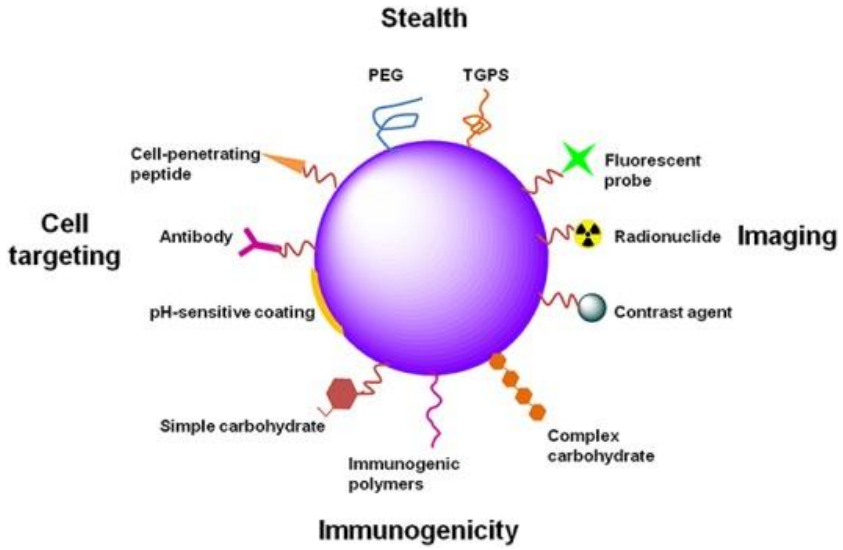

Figure 1.6: Possible structure of functionalized core-shell nanoparticles for biomedical applications. One or some functionalization can be performed, depending on the applications of the nanoparticles. Note that the figure does not show the actual ratio between particle and functionalities (E.g. antibody). Reprinted with permission from Ref. [9].

[38]. The most common agents that are coupled to NPs are fluorescent dyes, which are covalently bound to the NPs. This functionalization is often used to study the cellular uptake of the NPs [7]. Also, immunogenic polymers and several simple and complex carbohydrates can provide the immunogenicity for MuNPs [40]. The functionalization of NPs with antibodies (or several molecules) can be used for cell targeting [41], [42]. The principle is based on the specific interaction of antibodies and antigens on cell. pH-sensitive coating agents can be exploited to control the release of drugs which are loaded inside NPs [43], [44].

1.2.3 Tumor targeting antibody conjugated multifunctional NPs for cancer therapeutic applications

Cellular uptake

Here we discuss how MuNPs can help with cancer diagnosis and therapy. As mentioned in Section 1.2.1, the utilization of tumor targeting antibody conjugated NPs is the key for the improvement of current theranostics. By using these cancer targeting NPs, more particles are able to approach cancer cells. Consequently, the cellular

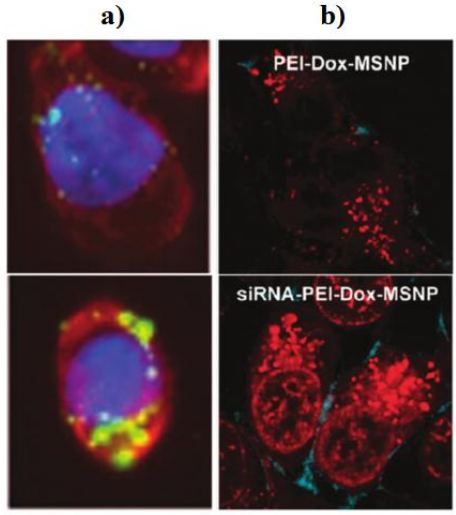

Fig. 1.7: Examples of the enhancement of cellular uptake for tumor targeted MSNPs. (a) Fluorescence microscopy images of particles taken up by a metastatic cancer cell line MDA-MB435, showing the enhancement of cellular uptake for tumor targeted MSNPs (lower) compared to particles without any targeting group (upper). Green/yellow fluorescence indicates FITC-labeled MSNPs (FITC: fluorescein isothiocyanate). (b) Fluorescence microscopy images showing significant increase in cellular uptake for tumor targeted MSNPs in KB-V1 cancer cells (lower). MSNPs were loaded with anticaner drug Doxorubicin which also acts as red fluorescent agent. Adapted with permission from Ref. [7].

uptake of these NPs is also increased as compared the uptake of free drug or naked nanoparticles [7]. Fig. 1.7 shows two examples of the enhancement of cellular uptake for tumor targeting nanoparticles as compared with the cellular uptake for non-targeting NPs. The bare nanoparticles in these two examples were mesoporous silica NPs (MSNPs). The particles were labeled with fluorescent agents, allowing to determine the location of tumor targeting NPs by fluorescence microscopy.

Early disease diagnostics: Many diseases, including liver cancer, can only be diagnosed when they are at the very last stage. In this case, surgery is not possible any more and other therapies only have limited success. Thus, early diagnosis is required and the utilization of MuNPs is a feasible solution [1], [39]. One interesting challenge is the search for new enhanced contrast imaging agents (MRI, fluorescent imaging, nonlinear imaging). In this way, the sensitivity of current diagnostic methods can be

significantly improved. For example, current agents in MRI techniques are based on Gd^{3+} chelates with high stability. These small gadolinium containing molecules work by shortening the T1 relaxation time of atoms (such as water protons) in body tissues, therefore improve the visibility of tissues in MRI scanner. However, these MRI methods are not sensitive enough to observe unusual tissue in the early stage. Moreover, gadolinium is also toxic: Gd-based MRI agents cause blood-brain barrier defects [45]. Contrary to small Gd-based molecules, several nanoparticles such as superparamagnetic IONPs, superparamagnetic iron platinum NPs have been shown to be sensitive MRI agents because of good T2 relaxivities [46]–[48]. These particles work by reducing the T2 signals of absorbing tissues.

Besides disease diagnostics based on imaging agents, there are other methods based on the determination of specific compounds/bio-entities generated by the presence of the disease. At the early stage of any disease, the amount of pathogenic entities is too small for current assays to determine. Then, MuNPs do not interfere in the assay method but increase the concentration of these entities. The most convenient method is magnetic separation with the aid of antibody conjugated NPs. For example, Legionella pneumophila bacteria, known to cause the Legionnaires' disease or legionellosis, a serious form of pneumonia [49], [50], can be magnetically separated by using antibody conjugated IONPs [50]. In this way, the detection limit of current methods is significantly increased. This strategy can be exploited in pre-concentration protocols for numerous other pathogens.

Cancer therapy

Current cancer treatments include surgery, hyperthermia, chemotherapy, radiation therapy, surgery, gene therapy and immunotherapy. Except for surgery, all treatments can be significantly improved when combining them with tumor targeting nanoparticles.

***Hyperthermia**:*

Nanomedicines that relied on hyperthermia were the first to be used in cancer therapy. The approach involves raising the temperature of the local environment of a tumor resulting in a change of the physiology of diseased cells finally leading to apoptosis [51]. Nanoparticles can be strongly heated under the influence of an oscillating magnetic field (in case of magnetic core) [52] or light irradiation (in case of plasmonic NPs or nanoshells). Cell death can occur when the temperature of the region increases above 41 ^{o}C while necrosis occurs at 50 ^{o}C and above [5], [13].

***Targeting drug delivery and release**:*

Herein, 'drug' can be understood as an specific anticancer medicine or therapeutic agent such as a radioactive isotope. The payload is loaded inside MuNPs designed in such a way to gradually release the payload or controllably release the payload under a physical/chemical stimulus. In the case of very toxic drugs (such as 5-fluorouracil

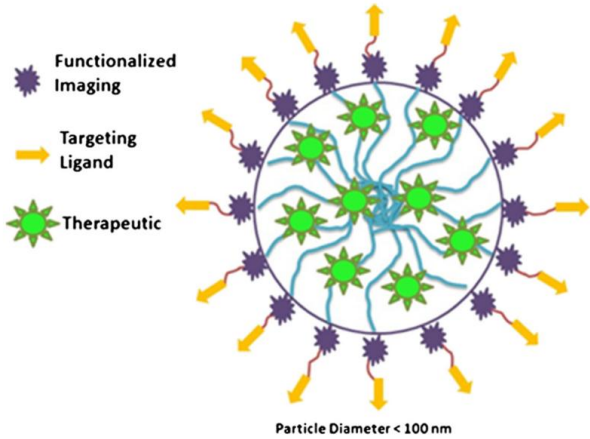

Fig. 1.8: Schematic of a theranostic agent, including a nanoparticle at the core, an imaging component, targeting ligands, and therapeutic agents. Reprinted with permission from Ref. [59].

hydroxycamptothecin, docetaxel, and gemcitabine), hiding drugs inside NPs limits the exposure of healthy tissue to the drug and consequently decrease the toxicity of therapeutics [53]–[56]. In addition, the efficiency of chemotherapy is improved.

Moreover, the loading of drugs inside NPs is especially important with water insoluble drugs. These drugs show high efficiency against cancer, however their low solubility does not allow to transfer a high dose of drugs to tumors. This problem was solved by using mesoporous silica shell as the carrier that is able to load high concentrations of water insoluble drugs [57].

Theranostic nanomedicine:

MuNPs provide agents for cancer diagnostics and therapy. Moreover, **thera**py agents and diag**nostic** agents can be present together in the same formulation– named **theranostic** agents [58]. Firstly, the theranostic agents need to consist of a nanoparticle core. Secondly, it is essential that there is a tumor targeting ligand present as mentioned in Section 1.2.1. Moreover, theranostic NPs often consist of a diagnostic imaging domain and therapeutic agents [59] (see Fig. 1.8). Theranostic agents also need to be smaller than 150 nm, because bigger particles will not penetrate into tissue and they will also be recognized as an alien object by the immune system.

Both organic and inorganic NPs can be used as the core to build the theranostic NPs. Among them, polymers, lipids, proteins (organic materials) and iron oxide, gold, silica (inorganic materials) are the most commonly used [7] . Interestingly, in the case of

hyperthermia treatment, the iron oxide core or gold NPs/nanoshells do not only act as therapeutic agent but also hold the function of diagnostic imaging domain. In addition, in the case of drug delivery and release, iron oxide core or gold NPs/nanoshells also can act as a stimulus source to release therapeutic payload.

1.3 Magnetic materials and iron oxide nanoparticles

1.3.1 Magnetic materials

Magnetism is a class of physical phenomena that are mediated by magnetic fields. Electric currents and the magnetic moments of elementary particles give rise to a magnetic field, which acts on other currents and magnetic moments.

When applying a magnetic field to materials, the materials will interact with the magnetic field and their magnetic properties are characterized by the magnetization M (the magnetic moment per volume). A plot of the magnetization against the field strength is called a magnetization curve.

The magnetization depends on the magnetic field strength (H) and the nature of each material [60]. This is expressed by Eq. 1.1:

$$M = \chi H \qquad \text{(Eq.1.1)}$$

(χ is the susceptibility of the material)

Based on the sign and the size of χ, magnetism can be classified as follows:

- Diamagnetism (χ negative, small)
- Paramagnetism (χ positive, small)
- Ferromagnetism(χ positive, large)
- Antiferromagnetism (χ positive, rather small)
- Ferrimagnetism (χ positive, rather large)

Diamagnetism: Materials can have or not have intrinsic electron magnetic moments, depending on the electron state of materials. In case the materials do not have electron magnetic moments (all electrons are paired), magnetic dipoles will be formed that oppose the applied magnetic field. Magnetism here is diamagnetic, and χ is negative and small (see Fig. 1.9). [61]

Paramagnetism: In a paramagnet, there are unpaired electrons in atomic or molecular orbitals. These unpaired electrons are free to align their magnetic moment in any direction. When an external magnetic field is applied, these magnetic moments will tend to weakly align themselves in the same direction as the applied field. Therefore, χ is positive and small.

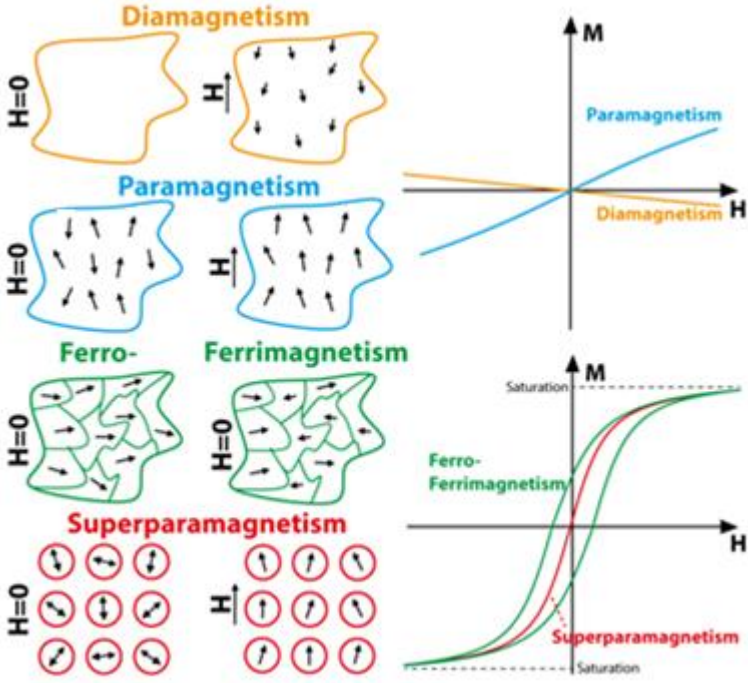

Fig. 1.9: Visualization of magnetic orderings and their magnetization responses (M) as a function of applied magnetic field strength (H). Note that for ferro- and ferri-magnetism, materials are assumed to be magnetized first. Adapted with permission from Ref. [61].

Ferromagnetism: A ferromagnet, like a paramagnet, has unpaired electrons. However, the intrinsic electron magnetic moments have a tendency to be parallel to an applied field and be parallel to each other to maintain a lowered-energy state (see Fig. 1.9). Thus, even in the absence of an applied field, the magnetic moments of the electrons in the material spontaneously line up parallel to one another. In this case, χ is positive and large.

Every ferromagnetic substance has its own individual temperature, called the Curie temperature, above which it loses its ferromagnetic properties and becomes a paramagnet. This is because the thermal tendency to disorder destroys the ferromagnetic order. Ferromagnetism only occurs in a few substances; the common ones are iron, nickel, cobalt, their alloys, and some alloys of rare earth metals.

***Magnetic domain**:* The magnetic moments in a ferromagnetic material are localized in small regions called magnetic domains (Weiss domain) (see Fig. 1.9). In each domain, magnetic moments stick together and align themselves in the same direction. When exposed to a magnetic field, the domain boundaries move so that the domains align parallel with the magnetic field and dominate the structure. When the external magnetic field is removed, the domains still remain in their positions. So, the ferromagnetic material is magnetized and becomes a permanent magnet.

Antiferromagnetism: In an antiferromagnet, unlike a ferromagnet, there is a tendency for the intrinsic magnetic moments of neighboring valence electrons to point in opposite directions. Antiferromagnets have a zero net magnetic moment, meaning no field is produced by them. Antiferromagnets are less common compared to the other types of magnetism, and are mostly observed at low temperatures.

Ferrimagnetism: Like antiferromagnets, neighboring pairs of electron spins like to point in opposite directions. However, these magnetic moments do not cancel completely (see Fig. 1.9). Therefore, a ferromagnetic material still retains its magnetization in the absence of a magnetic field, like a ferromagnetic material. Most ferrites are ferrimagnetic materials. The first discovered magnetic substance, magnetite, is a ferrite and was originally believed to be a ferromagnet.

Superparamagnetism: When the size of a ferromagnet or ferrimagnet is sufficiently small (smaller than single domain size), it exits as a single domain and acts like a single magnetic spin that is subject to Brownian motion. Magnetic moments can orient freely in all possible directions, resulting in a non-magnetized state of the material. When an external magnetic field is applied, the magnetic moments in all single domains align to the magnetic field. These properties are similar to those of a paramagnetic magnetism, and the material will return to the non-magnetized state when removing the external magnetic field. This kind of material is called a superparamagnetic material.

The estimated single domain size for spherical magnetite particles is 128 nm [62] whereas Fe_3O_4 NPs below 25 nm can exhibit characteristics of superparamagnetic NPs [63].

In general, to obtain a material with large magnetic susceptibilities, atoms with large magnetic moments (e.g., Fe, Ni, Co) need to be incorporated. We choose IONPs for our study due to several reasons. Firstly, Iron oxide (magnetite, maghemite) has large magnetic moments. Secondly, there are several rapid and economical methods allowing to prepare IONPs in large quantities. Thirdly, IONPs themselves show low toxicity, biocompatible, which is important for applications in biomedical field. And lastly, properties of IONPs including structural, chemical and physical properties are available in the literature [5], [64]–[68].

Table 1.3: Practical data on iron oxides [69].

Structure	**Magnetite** Fe_3O_4	**Maghemite** γ-Fe_2O_3	**Hematite** α-Fe_2O_3
Structural type	Inverse spinel	Defect spinel	Corundum
Crystallographic system	Cubic	Cubic	Hexagonal
M_s at 300 K (*emu/g*)	92-100	60-80	0.3
Curie temperature (K)	850	820-986	956
Density (g/cm^3)	5.15	4.9	5.3
Percentage iron (%)	72.4	69.94	69.94
Color in dispersion	Black	Dark brown	Blackish red

1.3.2 The iron oxides

IONPs can have different morphologies, such as hematite (α-Fe_2O_3), maghemite (γ-Fe_2O_3) or magnetite (Fe_3O_4).

Maghemite and Magnetite are ferrimagnetic materials whereas hematite is an antiferromagnetic material. So, we only describe the first two magnetic types of iron oxide. A summary of practical data on iron oxides is shown in Table 1.3 [69].

Magnetite, $Fe^{2+}(Fe_2{}^{3+}O_4)$, has a black color. It is a member of the cubic ferrites, also called ferrospinels because their structure is closely related to that of the mineral spinel, $MgO{\cdot}Al_2O_3$ [70], [71]. In the spinel structure, the larger oxygen ions are packed quite close together in a face-centered cubic arrangement and the much smaller metal ions occupy the spaces between them. There are two kinds of spaces available, tetrahedral *A* sites and octahedral *B* sites (see Fig. 1.10). In the normal spinel structure (e.g., $MgO{\cdot}Al_2O_3$), all Al^{3+} ions are located in octahedral B sites, and all Mg^{2+} ions are located in tetrahedral A sites.

Magnetite exhibits an *inverse spinel* structure. Half of the Fe^{3+} ions are located in the tetrahedral and a half of the Fe^{3+} are located in the octahedral lattice sites, while Fe^{2+} is only in the octahedral sites [72]. This arrangement causes the magnetic moments of Fe^{3+} to cancel each other out (tetrahedral and octahedral sites have opposite spins), leaving only the moment of Fe^{2+} contributing to the overall magnetic moment (see Fig. 1.11). As mentioned above, magnetite is a ferrimagnetic material.

Maghemite (γ-Fe_2O_3) has a dark brown color and a similar crystal structure as magnetite. The difference is that there are vacancies in the cation sublattice and the result can be called a defect spinel.

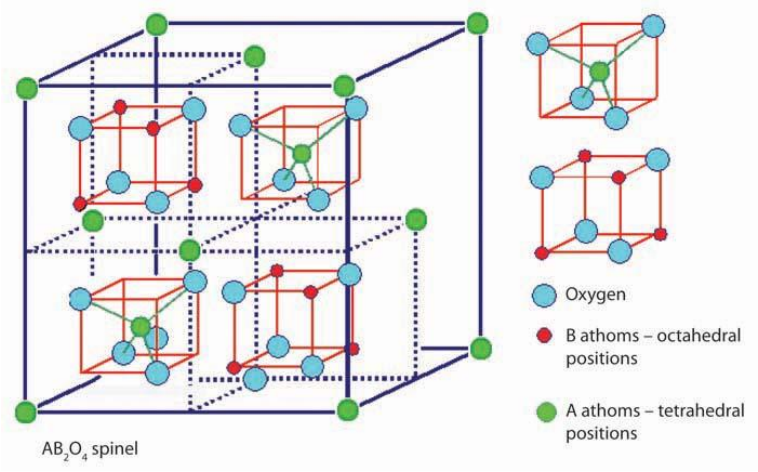

Fig. 1.10: AB_2O_4 spinel structure. Reprinted with permission from Ref. [71]

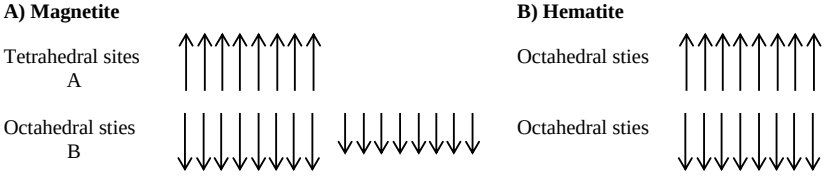

Fig. 1.11: Arrangement of magnetic moments in magnetite crystal and hematite crystal.

1.3.3 Synthesis method

Many studies on the synthesis of Fe_3O_4 nanoparticles have been reported so far [62], [63], [65], [73], [74]. The first and most widely used method is co-precipitation. Other methods include the polyol and thermal hydrolysis method, micro-emulsions, thermal decomposition, laser ablation, flow-injection. The properties of the most common methods are compared in Table 1.4 [62], [63], [65], [73], [74].

Although thermal decomposition occurs at high temperature, the procedure does not require any special equipment. This method also allows to achieve large quantities of the product with high quality. Therefore, IONPs were mainly synthesized by this method in this dissertation.

Table 1.4: Common methods for the fabrication of Fe_3O_4 NPs. Thermal decomposition method was preferred because it can produce high quality product (narrow size, good shape control) at the large scale. Adapted with permission from Ref. [15].

Method	co-precipitation	microemulsion	hydrothermal	thermal decomposition
Conditions	air	air	high pressure	air/inert gas
T (^{o}C)	20-95	20-50	180-220	180-350
Solvent	water	water in oil	water-alcohols	long hydrocarbons
Distribution	broad	medium	narrow	very narrow
Size	2-100	1-50	10-800	3-50
Shape control	not good	good	good	good
Scale (gram)	large (0.1-2)	small (0.1-0.3)	small (0.1-0.5)	large (1-40)

Thermal decomposition

The decomposition of iron precursors in the presence of hot organic surfactants results in samples with good size control, narrow size distribution and good crystallinity. Moreover, the obtained IONPs are well dispersed in the organic phase due to the presence of a coating layer. Initially, this method was used for the synthesis of semiconductor NPs. Later, the method was adapted for the synthesis of IONPs. Different organometallic precursors, solvents and surfactants can be used for the synthesis. However, the change of each of the above factors, together with reaction temperature and aging time, will result in a change of shape, size and magnetic properties of the obtained IONPs. Possible iron precursors are the complexes of acetylacetonate (acac), carbonyl, oleic acid/fatty acids, N-nitrosophenylhydroxylamine (cup). [62], [75]–[78].

Among the iron precursors mentioned above, iron oleate is the most inexpensive one and can be easily prepared from iron (III) chloride and sodium oleate. Another advantage is the nontoxicity of all reactants. Park *et al*. were able to synthesize up to 40 g of monodisperse IONPs in a single reaction batch [79].

Although the mechanism of the reaction is not fully described [80], the observation of some side products such as radicals and ketones give some hints for the mechanism. The most complete description has been published by Perez et al. [81]. Fig. 1.12 describes the mechanism with the formation of a radical under heating at the start. This step plays an important role because it provides the oxygen for the iron oxide

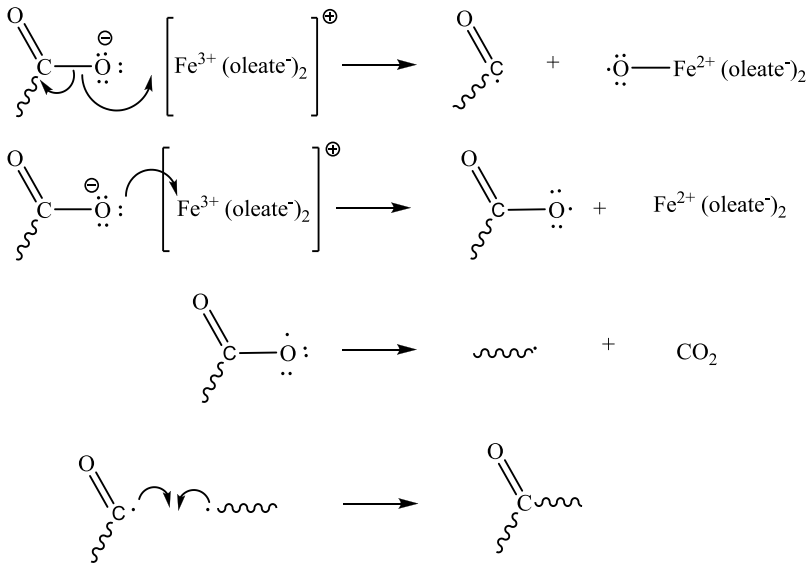

Fig. 1.12: The decomposition of iron-oleate at high temperature happens via a radical process. Carbon dioxide gas is released from the oleate molecules in one of these reaction steps. Adapted with permission from Ref. [15].

formation as well as the reduction of Fe^{3+} to Fe^{2+}. The observation of ketones at different stages in the reactions is explained by the combination of two radicals.

A drawback of this method is the low saturation magnetization of IONPs - typically 25 emu/g [75] whereas the value of bulk Fe_3O_4 is 92-100 emu/g [69] – which can be partly explained by the small size of the obtained particles.

Besides thermal decomposition, another method - called forced hydrolysis - is used to synthesize IONPs in this dissertation (only in Chapter 2). Basically, this method is a modification of the polyol and hydrothermal reactions [65], [82]. The technique is based on the dissolution of iron salts in a polyol solvent with subsequent heating or reflux in the present of a capping agent. Typical synthesis can lead to a yield of 1 gram of NPs with high magnetization [63]. The experimental route will be described briefly in Chapter 2.

After synthesis, obtained IONPs are coated with oleic acid. The particles are only dispersible in apolar solvents (e.g., hexane, chloroform). For further use in biomedical applications, the surface needs to be functionalized with a polar moiety. The surface functionalization does not only provide a functional group, but also improves the

stability of the colloidal IONPs. The following section will give an overview of the different functionalization strategies.

1.3.4 Surface functionalization of IONPs

IONPs are coated with protecting agents in order to improve the chemical or physical stability, as well as to provide functional groups for their applications [83]–[85]. Surface coating protects the NP from the environment and sustains the properties of the core. The improvement of the physical stability should be understood as the prevention of aggregation from colloidal dispersion - which will be discussed in the next section.

There are three strategies to functionalize IONP's surface: using i) organic molecules, ii) polymers or iii) inorganic shell as described in Fig. 1.13. Some detailed discussions about the surface functionalization of IONPs can be found in the literature [15], [65].

In iron oxide, the surface iron atoms act as Lewis acids and coordinate with molecules that donate lone-pair electrons. Therefore, interactions between IONPs and coating agents usually start with acid-base reactions. This can be easily seen in the case of functionalization by organic molecules, such as carboxylates (e.g., citric acid [86], dimercaptosuccinic acid (DMSA) [87], [88]) , phosphates [89]–[91], sulfates [62], derived catechol [92]–[94] and alkoxysilane [75], [95]. Another strategy is the use of polymers such as PEG, dextran, polyvinyl alcohol (PVA). IONPs are embedded in the matrix in which the interaction between iron atoms and oxygen atoms play an important role.

IONPs can be coated with silica/mesoporous silica (mp-SiO_2) [52], [96]–[99] or gold [100]–[102]. These coatings help in binding various biological ligands to the nanoparticle surface. An overview and experimental routes of the coating of IONPs by gold nanoshells will be discussed in detail in Chapter 3. Here, we only discuss the functionalization of IONPs with a SiO_2/mp-SiO_2 shell. The most popular method used to grow a silica shell is the Stöber method based on the hydrolysis and condensation of a silica precursor such as TEOS/EtOH in the presence of a base (NH_3, NaOH,…) [103]. The Stöber method is known as an effective method to synthesize silica NPs, and its modification can lead to the formation of silica nanoshells. In addition, during the growth of the silica shell, a large excess of surfactants (e.g., cetyltrimethylammonium bromide/chloride [7], [104], [105]) can be added to form mp-SiO_2 shells. Fig. 1.14 shows the pore system of mp-SiO_2 taken by transmission electron microscopy (TEM) and scanning electron microscopy (SEM) [106].

Mesoporous silica is a mesoporous form of silica and a recent development in nanotechnology. The most common types of mesoporous nanoparticles are MCM-41 and SBA-15 with a large pore size up to 30 nm [107], [108]. These pores are much larger than pores in microporous material. Research continues on the NPs/nanoshells,

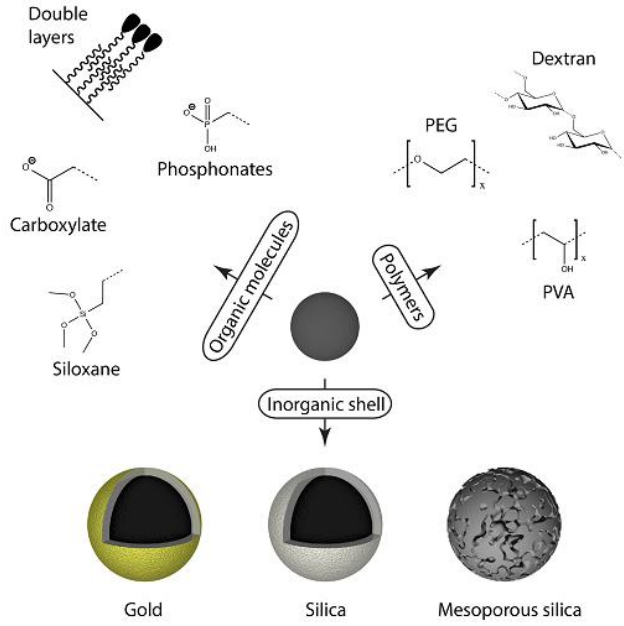

Fig. 1.13: Overview of surface functionalization of IONPs by polymers, organic molecules or inorganic shells. Reprinted with permission from Ref. [15].

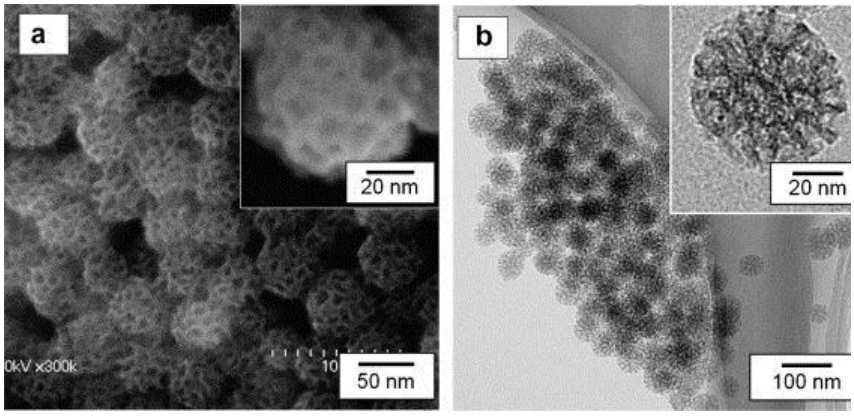

Fig. 1.14: SEM (a) and TEM (b) images of mesoporous silica nanoparticles. The insert image is a high-resolution electron microscopy image of a single silica particle. Reprinted with permission from Ref. [106].

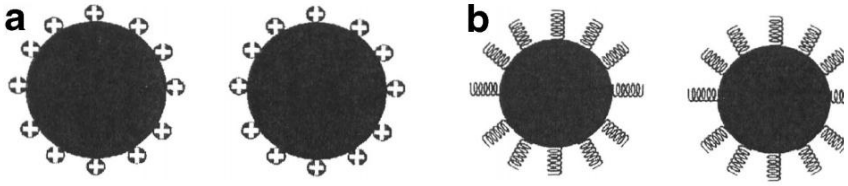

Fig. 1.15: (a) Particles stabilized by the electrostatic layer. (b) Particles stabilized by steric repulsion. Reprinted with permission from Ref [65].

which have applications in catalysis, drug delivery and imaging [109]. The large surface area of the pores allows the particles to be filled with a drug or a cytotoxin. Ordered mesoporous silica [106], [110]–[112] also shows potential to boost the in vitro and in vivo dissolution of poorly water-soluble drugs, such as itraconazole [113], [114].

1.3.5 Colloidal stability

The stabilization of IONPs in aqueous media is crucial for all advanced applications. The stability of a magnetic colloidal suspension depends on the relation between attractive and repulsive forces. There are four types of attractive/repulsive forces that are able to contribute to the interparticle potential in the colloidal system, including van der Waals forces, the electrostatic repulsive forces, magnetic dipolar forces and the steric repulsions. To be stable, colloidal NPs need to have repulsive forces that are more dominant than the attractive forces. This can be achieved by altering the electrostatic and steric forces (see Fig. 1.15). The steric force is very important when the particles are coated with a polymer [115]. In many cases, it plays a key role for the stability of the colloidal system [75]. The steric force depends on the molecular weight of the polymer and its density [116], [117]. The electrostatic repulsion can be estimated through the zeta potential (ZP) measurement [15], [118]. In the absence of steric stabilizers, the system is admitted as colloidal stable if the absolute value of the ZP is higher than 25 mV [15], [119]. However, a colloidal suspension with a low ZP value can still be highly stable if steric stabilizers are present [75].

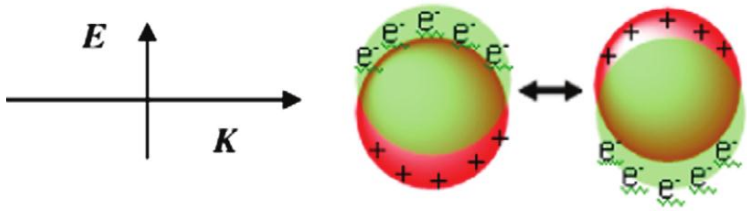

Figure 1.16: Schematic illustration of surface plasmon resonance in plasmonic nanoparticles, where E is the electric field and K is the wave vector (the direction of the light propagation). Reprinted with permission from Ref. [121].

1.4 Plasmonic properties

1.4.1 Interaction of metals with light – the Surface Plasmon Resonance

It is generally known that all interesting properties of metals are due to the presence of valence electrons. When light interacts with the metal, the electromagnetic field of light causes the electrons to move with respect to the positive cores, leading to the formation of a dipole oscillation (see Fig. 1.16). When the amplitude of this oscillation reaches a maximum at a certain wavelength, the oscillation is called a (localized) surface plasmon resonance (LSPR) [120]–[124].

The resonant frequency (or wavelength) plays an important role. If the frequency of the incident light is greater than the resonance frequency of the metal, light will be transmitted. Otherwise, light is reflected. Because most metals have a resonance in the UV region, visible light will be reflected by these metals. This explains the shiny surface of most metals. On the other hand, gold and copper have an optical resonance frequency in the visible region. This results in their distinct color.

Because the LSPR induces a strong absorption of the incoming light, the absorption can be recorded by using a UV–Vis spectrometer. Gold NPs (together with silver and copper NPs) exhibit a strong LSPR band in the visible region, while other metallic NPs exhibit a broad and weak band in the UV region [125], [126]. For example, Au NPs show an SPR band around 520 nm.

The SPR band is affected by the particle shape and size [120], [121], [127], hence Au NPs with different shape and size exhibit different colors and their colors differ from the color of bulk gold. Fig. 1.17 shows the color of bulk gold (left) and colloids of gold nanoparticles in a Gothic stained glass rose window of Notre-Dame de Paris (right) [128].

Figure 1.17: (left) color of bulk gold and (right) color of colloids of Au NPs in a Gothic stained glass rose window of Notre-Dame de Paris [128]

The position and intensity of the LSPR band is determined by the electron density on the surface of the metal. Hence, metal type, particle shape (nanosphere, nanorod…), size, structure (metallic NPs, metallic shells….) and the dielectric constant of the medium all affect the position of the plasmon band. All these factors can be described theoretically by Mie theory [121], [122], [129], [130]. The following section will discuss the effect of these parameters on the position of LSPR bands.

Another interesting property of LSPR comes from the enhancement of the amplitude of the field near metal surface. This field is highly localized at the metal surface (within 10 nm from the interface) and decays rapidly. So, any molecule present within this distance from the NP surface will experience these large fields [120][131]. This leads to several interesting applications in "surface-enhanced'' spectroscopies, including surface-enhanced Raman spectroscopy (SERS) [124], [132].

1.4.2 Position of the SPR band of Au NPs

Intensity and position of the SPR band can be predicted from Mie theory – which is the Mie solution to Maxwell's equation for the interaction of an electromagnetic plane wave with a nanoparticle. Different geometry of Au nanoparticles leads to different solutions. In the simplest case, spherical Au NPs, the extinction cross-section (C_{ext}) is determined by the following equation [121][129]:

$$C_{ext} = \frac{24\pi^2 R^3 \epsilon_m^{3/2}}{\lambda} \frac{\epsilon_2}{(\epsilon_1 + 2\epsilon_m)^2 + \epsilon_2^2} \qquad \text{(Eq. 1.2)}$$

Where: R is the radius of Au nanospheres,

ϵ_m is the dielectric constant of medium,

$\epsilon = \epsilon_1(\omega) + i\epsilon_2(\omega)$ is the dielectric constant of the metal.

Note that Eq. 1.2 is only valid when the size of Au NPs is much smaller than the wavelength of incident light and only dipole oscillator contributes to the extinction cross-section.

When C_{ext} is maximum, $\lambda = \lambda_{peak}$. This happens when:

$$\epsilon_1 + 2\epsilon_m = 0 \qquad \text{(Eq. 1.3)} \qquad \text{or} \quad \epsilon_1 = -2\epsilon_m \qquad \text{(Eq. 1.4)}$$

On the other hand, the position of SPR peak (λ_{peak}) is determined from following equation [130]:

$$\frac{\lambda_{peak}^2}{\lambda_p^2} = \epsilon^{\infty} + 2\epsilon_m \qquad \text{(Eq. 1.5)}$$

Where: λ_p is the bulk metal plasmon wavelength,

ϵ^{∞} is the dielectric constant of the bulk metal at infinitive wavelength.

Using Eq. (1.2) and Eq. (1.5), one can predict the change of LSP band when parameters such as particle size (R) and refractive index of the medium (n) change. ($n = \sqrt{\epsilon_o . \mu}$ where: μ is the relative permeability of the medium and ϵ_o is the vacuum dielectric constant of the medium)

In following paragraphs, experimental data will be discussed to confirm the prediction from Mie theory.

As mentioned above, the position of the SPR band of Au NPs firstly depends on the size of the NPs. E.g., spherical Au NPs show a SPR band around 520 nm whereas that of Au NPs smaller than 10 nm is largely damped. This is explained by the surface scattering of the conduction electrons [130] and by the phase change of Au NPs caused by the increased rate of electron-surface collisions compared to larger particles [121]. Some studies reported that 4 nm Au NPs still exhibit a weak SPR band at around 515 nm [120], however Au NPs smaller than 2 nm does not exhibit the SPR [133]. On the other hand, increasing particle size red-shifts the SPR wavelength and also increases the intensity (see Fig. 1.18a).

Secondly, the position of SPR bands depends on the shape of NPs (e.g., nanospheres [121], nanorods [120], [134], nanocages [135], nanorices [136]). Fig. 1.18b illustrates the optical properties of gold nanoparticles that change drastically with nanoparticle shape. The photograph shows an aqueous solution of 4 nm gold nanospheres (vial 0) and gold nanorods (1-5) with progressively higher aspect ratio. The optical spectra for the particles in vials 1–5 are also shown.

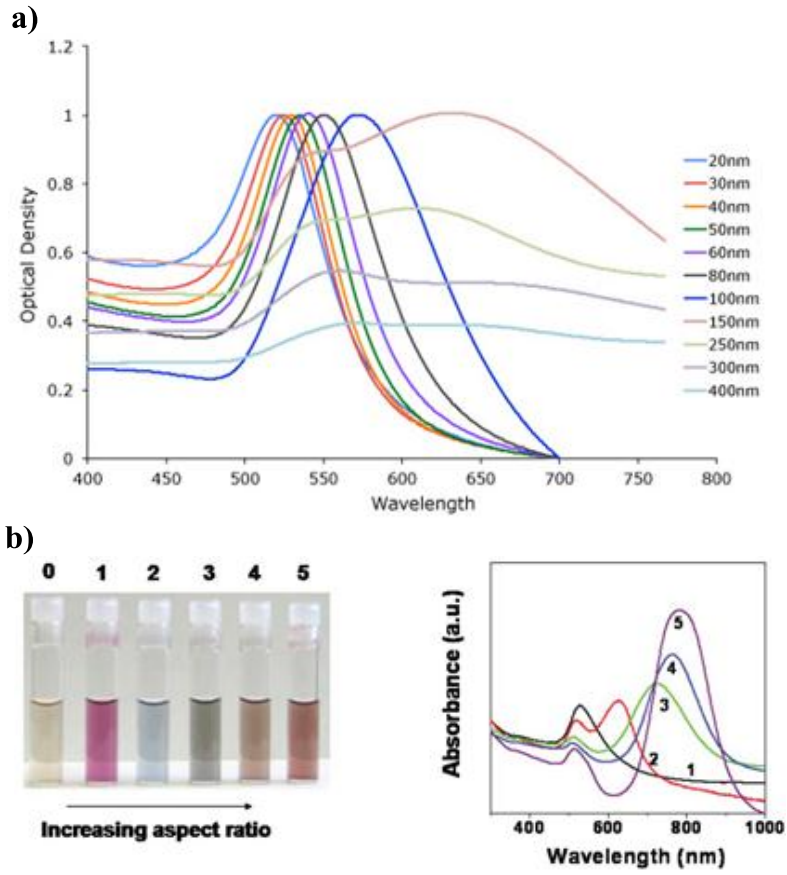

Fig. 1.18: The optical properties of gold nanoparticles change drastically with nanoparticle size (a) and shape (b). (a) SPR band of Au nanospheres is red-shifted when size increase, reprinted from Ref. [198]. At 150 nm, Au nanospheres exhibit two SPR bands corresponding to transversal and longitudinal SPRs (Au NPs are not completely spherical due to defects in their nanostructures). (b) The photograph shows aqueous solution of 4 nm gold nanospheres (vial 0) and progressively higher aspect ratio gold nanorods (1–5). Reprinted with permission from Ref. [120].

Thirdly, the position of the band depends on the colloidal stability of Au NPs. Aggregation of noble metal nanoparticles red-shifts and broadens plasmon bands. For colloidal 4 nm Au nanospheres, this results in a visual color change from orange–red to purple or blue (see Fig. 1.19). The aggregation depicted here resulted from an increased ionic strength in aqueous solution. Finally, the position also depends on the

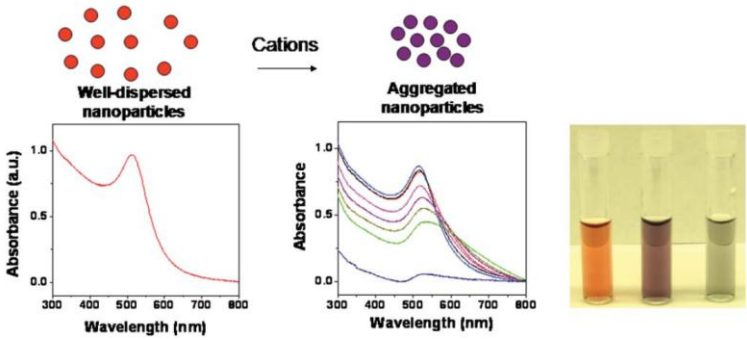

Fig. 1.19: Aggregation of 4 nm Au nanospheres induces the red-shift and the broadening of SPR band. This results in a visual color change from orange–red to purple or blue. Reprinted with permission from Ref. [120].

medium surrounding Au NPs, represented by the refractive index. Increasing the refractive index of the medium for Au NPs red-shifts the LSPR wavelength and strongly enhances the intensity of the resonance [61], pp. 24.

1.4.3 Position of the SPR band of Au nanoshells.

The combination of a magnetic iron oxide core and a plasmonic gold shell in a single nanostructure results in many interesting properties. The addition of a gold coating layer can be exploited in many advanced applications such as recoverable catalysts, bio-separation, diagnostics, photon-induced hyperthermia. The synthesis of iron oxide-gold core-shell NPs will be discussed in detail in Chapter 3. Here, we only discuss factors affecting the position of the SPR band of Au nanoshells.

Following Mie theory [122], the position depends firstly on the composition of the core. Different materials of the core with different permittivity can result in different positions of the SPR band. Secondly, the band depends on the core/shell ratio. On the other hand, with a given core, the position changes when the thickness of the Au shell changes. Following Levin et al., if the permittivity of the core is low (e.g., silica), the SPR band will blue-shift when the shell thickness increases. Otherwise, if the permittivity of the core is high (e.g., iron oxide), the band will red-shift to the NIR region when the shell thickness increases [101].

Note that when Au shell is thick enough, valence electrons on the surface of outer shell and inner shell are isolated, resulting in two different surface plasmonic resonances (see Fig. 1.20 and Fig. 1.21).

Fig. 1.20a describes the optical properties of a core-shell nanostructure consisting of 60 nm silica core and a gold shell. Shell thickness can vary from 5-20 nm. The

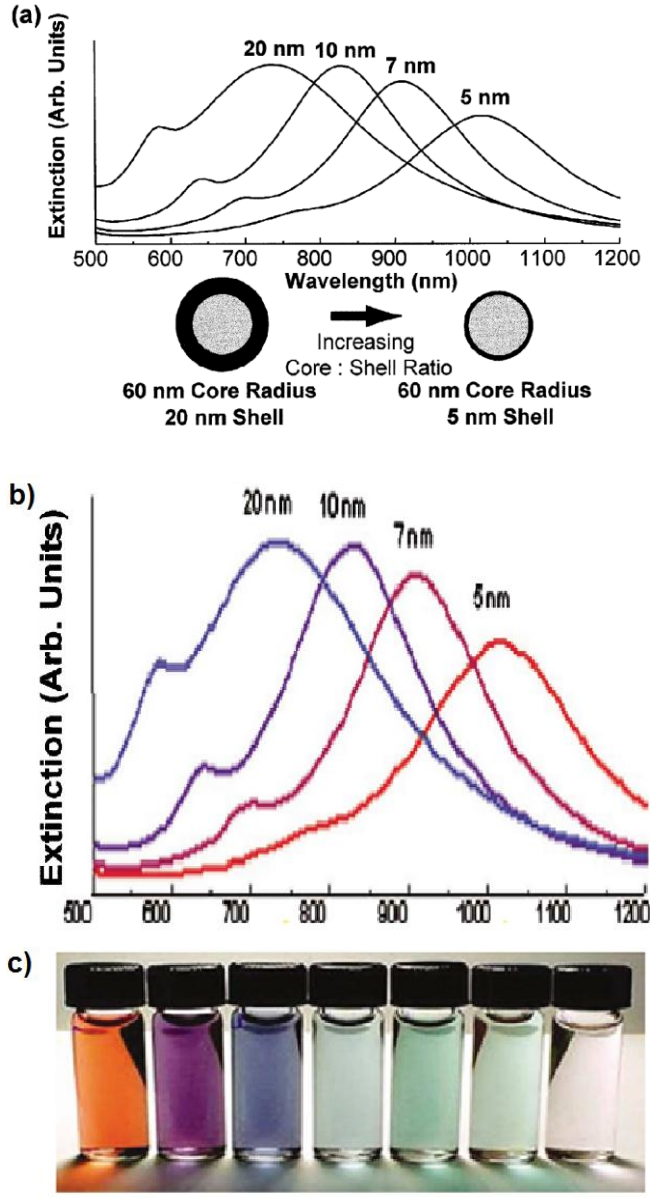

Fig. 1.20: Tunable optical properties of gold-coated 60 nm silica core by changing the shell thickness (5-20 nm). (a) Theoretical calculation of SPR bands, reprinted with permission from Ref. [195]. Practical absorption spectra (b) and physical appearance (c) of Au nanoshells with thickness varying from 5-20 nm. Reprinted with permission from Ref. [121].

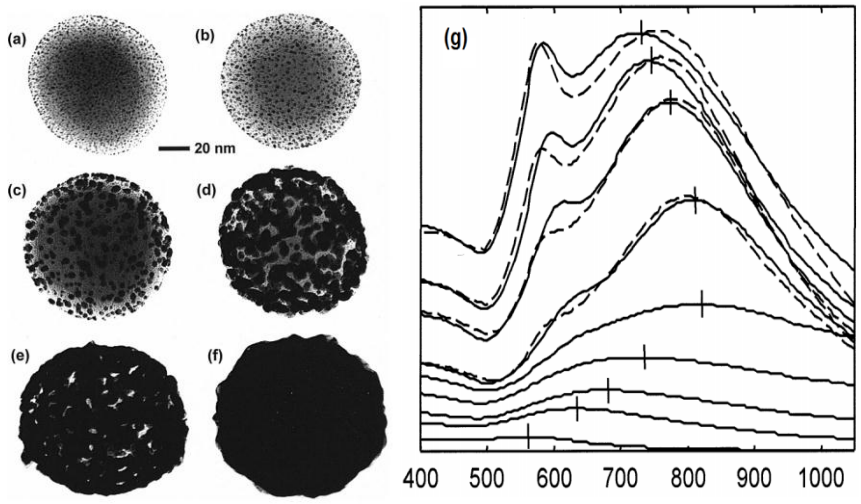

Fig. 1.21: (a – f) TEM images of nanoshell growth on 120 nm silica NPs. (a) Initial gold colloid-decorated silica nanoparticle, (b – e) gradual growth and coalescence of gold colloid on silica nanoparticle surface, (f) completed growth of metallic nanoshell. (g) UV-Vis spectra of colloidal dispersion during nanoshell growth indicate that the SPR bands tend to red-shift when the shell is incomplete and blue-shift when the shell is complete. Reprinted with permission from Ref. [195]

position of the SPR bands were theoretically calculated, showing a blue shift when the shell thickness increases. The experimental data in Fig. 1.20b,c also agree with the calculation.

Another example is the observation of gold nanoshell growth on the surface of 120 nm silica cores (see Fig. 1.21). Gold is gradually deposited on the silica surface, leading to the formation of incomplete Au nanoshells and then complete Au nanoshells. Their TEM images are shown in Fig. 1.21a-f whereas the absorption spectra of incomplete and complete gold shells are shown in Fig. 1.21g. The SPR bands tend to red-shift when the shell is incomplete and blue-shift when the shell is complete.

1.5 Nonlinear optics

When light with frequency ω interacts with a molecule, its oscillating electric field will induce a dipole moment in the molecule. In general, the induced dipole moment $\mu(\omega)$ can be described as a Taylor series [137]:

$$\mu_{ind} = \mu(1) + \mu(2) + \mu(3) + \ldots = \alpha E + \beta EE + \gamma EEE \qquad \text{(Eq. 1.2)}$$

Where: $\mu^{(1)}$, $\mu^{(2)}$ and $\mu^{(3)}$ is linear, quadratic and cubic, respectively, in the electric field. $\alpha(\omega)$ is the molecular first-order polarizability or linear polarizability. $\beta(\omega)$ and $\gamma(\omega)$ are the molecular second-order and third-order nonlinear polarizabilities. They are also called the first and the second hyperpolarizability. Since the induced dipole moment can be considered as the source of radiation, Eq. 1.2 can be used to describe all molecular optical properties.

However, when the intensity of the light is sufficiently low, $\mu^{(2)}$ and $\mu^{(3)}$ are very small and the induced dipole moment can be approximated as being linear in the electric field.

$$\mu_{ind} = \mu^{(1)} = \alpha(\omega)E(\omega) \qquad \text{(Eq. 1.3)}$$

In principle, this equation is sufficient to describe daily optical phenomena such as light scattering, absorption, etc.

At the macroscopic level, we consider the interaction of light with many molecules. In this case, we define the induced polarization of the entire medium as:

$$P_{ind} = P^{(1)} + P^{(2)} + P^{(3)} + \ldots = \chi^{(1)}E + \chi^{(2)}EE + \chi^{(3)}EEE \qquad \text{(Eq. 1.4)}$$

Where $\chi^{(1)}$, $\chi^{(2)}$ and $\chi^{(3)}$ are the first-, second- and third-order susceptibilities of the sample(also called the first and second nonlinear susceptibilities).

Both hyperpolarizabilities and susceptibilities are used to describe nonlinear optical phenomena that only occur at very strong light intensities (for example laser light). Well-known nonlinear optical phenomena are second-harmonic generation (SHG), hyper-Rayleigh scattering (HRS), two-photon fluorescence (2-PF), Third-harmonic generation (THG) and third-harmonic scattering (THS).

All of them are processes in which two or three photons are annihilated to create a new photon at a different frequency.

The interaction of the matter with two photons (SHG, HRS, 2-PF) or three photons (TGS, THS) can be visualized by the energy diagrams in Fig. 1.22. Note also that SHG (and HRS) and THG (and THS) can be non-resonant, while TPF has to be resonant in order to occur.

Whether or not a molecule or material exhibits strong nonlinear optical properties depends on several factors. However, an important one is symmetry of the medium under investigation. SHG and HRS only occur when the material or molecule is noncentrosymmetric, while THG, THS and 2-PF can occur in any material.

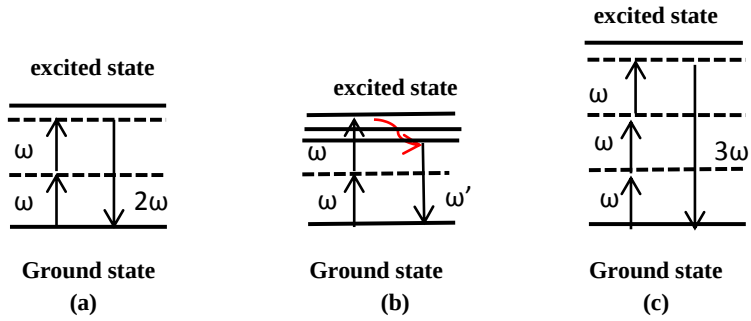

Fig. 1.22: The energy diagrams involve to multiphoton processes. In diagrams (a) and (c), matter interacts with two photons (a) or three photons (c) to form a virtual excited state (dashed lines), which is extremely short-lived. This leads to the emission of a photon with double or triple frequency. Energy diagram (b) refers to 2-photon fluorescence phenomenon in which matter absorbs two photons to reach its excited state (solid line). During the process, a part of the energy is lost and a photon ($\omega' < 2\omega$) light is released.

1.6 Objective and outline

The aim of this dissertation is to design versatile MuNPs based on IONPs and explore some potential applications of these materials in biomedical field. To be used in biomedical applications, the particles must be biocompatible and dispersable in water. Moreover, different properties need to be combined in one single particle for different purposes. Firstly, the particles gain interesting magnetic properties from iron oxide core, which can be exploited in bioseparations, MRI and magnetically induced hyperthermia. Besides, the particles might possess plasmonic properties for SPR-based biosensing and laser-induced hyperthermia, mesoporous silica shells for drug storage and delivery, or be conjugated to a fluorescent dye for imaging technique.

In order **to achieve the aim** stated above, we discuss first the synthesis of different core-shell structures of MuNPs. The nanostructure composes of a well-defined iron oxide core and a mono/multi-layer(s) nanoshell. The latter provides the colloidal stability, biocompatibility and more extra interesting properties. Next, we characterize the linear and nonlinear optical properties, as well as magnetic, plasmonic and mesoporous properties of synthesized materials. Finally, we explore several

applications of the MuNPs in some biomedical field, including protein coupling, nonlinear imaging, magnetically controlled drug release.

The outline of this dissertation is as follows:

The second and the third chapters focus on the functionalization of IONPs. In **Chapter 2**, IONPs are synthesized and are functionalized with carboxyl-terminated trialkoxysilane. Then, the ability of carboxyl functionalized IONPs to couple with bio-entities are tested with bovine serum albumin protein. The amount of protein coupling is quantified by the Bradford method.

Chapter 3 gives an overview of the synthesis of water-soluble iron oxide-gold core-shell NPs with different approaches. Gold nanoshells can be synthesized in an aqueous solvent or in an organic solvent. The syntheses of iron oxide-silica-gold and iron oxide-gold-silica multilayer nanoshells are also introduced in this chapter.

The next two last chapters focus on the applications of synthesized core-shell NPs. **Chapter 4** describes the design of rhodamine B bound iron oxide-mesoporous silica core-shell NPs as drug delivery agents. The hyperthermia-induced release of the payload is investigated under different magnetic fields.

Finally, nonlinear optical properties of iron oxide-mesoporous silica core-shell NPs are studied in **Chapter 5**. The possibility to exploit the system as nonlinear imaging/labeling is also discussed there.

Chapter 2

Synthesis of functional magnetic nanoparticles for protein coupling

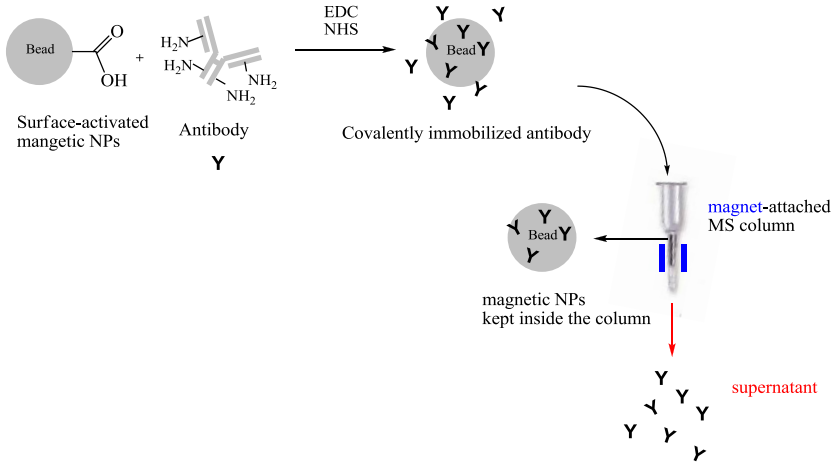

Author performed all experiments, measurements and analysis in this chapter.

Abstract

Superparamagnetic iron oxide nanoparticles (IONPs) were synthesized and their surface was carboxyl functionalized with COOH- terminated PEG-silane. Then, these magnetic nanoparticles were used as agents to bind bovine serum albumin (BSA) protein and the coupling was studied by Bradford assay. Generally, about 20 µg of protein could be bound to 1 mg of magnetic nanoparticles.

2.1 Introduction

In recent years, nano-sized magnetic particles have received considerable attention from researchers in the field of medicine and biotechnology [138]. Magnetic particles have been widely studied and used in many applications such as immobilization of enzymes [139], immunoassays [140], bioseparation [141], biosensor [142], targeting drugs [11][143], MRI reagents [144] and cancer hyperthermia treatment [145], [146]. These biomedical applications are due to the fact that tiny particles can penetrate the body without a specific reaction with antigens. Among magnetic materials, magnetite NPs are the most frequently chosen for the above studies, because these particles can be easily synthesized on a large scale and their magnetization is quite high allowing control by an external magnetic field.

Biomedical applications require magnetic nanoparticles (MNP) to be capped and surface functionalized. With the help of silane chemistry, a stable coating layer can be easily formed on the MNP surface and can provide many kinds of functional groups such as carboxyl, amine, hydroxyl, …[63], [147]–[149]. These functional groups are the basis for MNPs to make the coupling with many bioactive substances such as antibodies, enzymes. Owing to their magnetic properties, using protein - MNP conjugations is a promising approach for many bio-applications such as diagnostics and drug targeting.

For applications in bioseparation, IONPs perform as excellent materials. IONPs with different coating layers were used to separate target ions, molecules, cells or bacteria from aqueous solution [50], [150], [151]. The nanoparticles need to meet the following requirements: i) high colloidal stability, ii) high magnetic response and iii) high selectivity toward target. While all these criteria are important, the last one is the most difficult to achieve. Some studies report the utilization of IONP-antibody conjugate for bioseparation due to specific interactions between antibody and target. Recently, Bloemen et al. functionalized IONPs with customized PEG ligands and then with antibody for the selective separation of Legionella pneumophila bacteria [50]. The conjugate is hydrophilic and the antibody remains active to bacteria. However, the magnetization of IONPs should be improved to expand their potential applications in bioseparation.

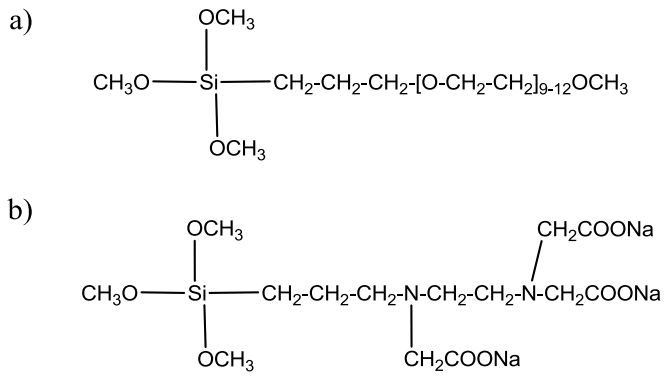

Fig. 2.1: The structures of PEG-silane (a) and COOH-silane (b).

(a) methoxy(polyethyleneoxy)propyltrimethoxysilane (9-12 PE-units)

(b) (Trimethoxysilylpropyl)ethylenediaminetriacetic acid trisodium salt.

In this chapter, we focus on a facile synthesis of carboxyl functionalized magnetite NPs with high colloidal stability and extremely high magnetic response and focus on the coupling of functional MNPs to BSA protein. The experiments described in this chapter lay a foundation for future functionalization of IONPs with targeting agents such as antibodies.

IONPs were synthesized by the forced hydrolysis method, and then carboxyl functionalized based on a silanization method. The advantages are: trialkoxysilanes can provide a more stable coating via covalent bonds and the IONP surface could be modified with a wide range of functional groups by applying various substituted silanes [63], [147]–[149]. A mixture of PEG-silane and COOH-silane (Fig. 2.1) was used as a coating reagent for the silanization. While PEG-silane was necessary to form a stable coating layer and increase the ability of the particles to disperse in many solvents, COOH-silane would provide carboxyl functionalized groups on the surface of IONPs. Functionalized IONPs could be covalently coupled with BSA protein via an amide bond [14], [50]. The reaction takes place between carboxylic groups on the magnetic particles surface and amine groups in BSA in the presence of activating substances: 1-Ethyl-3-(3-dimethylaminopropyl)carbodiimide (EDC) and hydroxysuccinimide (NHS) [152]. The reaction is illustrated in Fig. 2.2.

There are several methods to determine the amount of protein coupled to IONPs. In this study, we used Bradford assay, one of the most common assays for protein quantification because of its rapid and sensitive characteristics [153], [154] (see Section 2.5, SI). The principle of this method relies on the strong attraction (1:1 ratio)

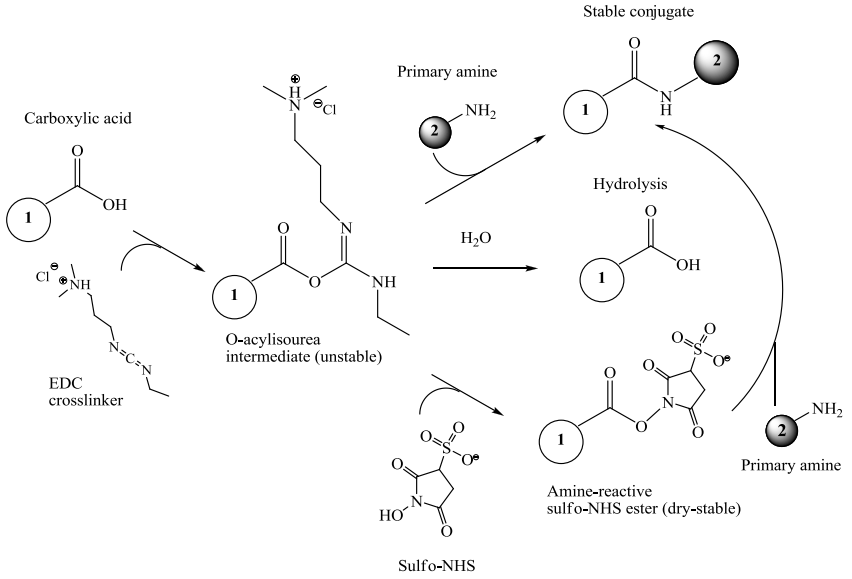

Fig. 2.2: Mechanism of reaction between carboxylic and amine groups with the activation of EDC and NHS [152]. EDC reacts with a carboxyl group on molecule #1, forming an amine-reactive O-acylisourea intermediate. This intermediate may react with an amine group on molecule #2, forming a conjugate of the two molecules joined by a stable amide bond. However, the intermediate is very susceptible to hydrolysis (rate constant measured in seconds), making it unstable and short-lived in aqueous solutions. The addition of NHS stabilizes the amine-reactive intermediate by converting it to an amine-reactive NHS ester, thus increasing the efficiency of EDC-mediated coupling reactions 1,2. The amine-reactive NHS ester intermediate has sufficient stability to permit two-step cross-linking procedures, which allows the carboxyl groups on one protein to remain unaltered. Besides, there are some side reactions of O-acylisourea ester, however these reactions do not affect to the main reactions because of the lack of activity.

between protein and Bradford reagent (CBB-Coomassie Brilliant Blue G-250) which leads to an increase of the solution absorbance at 595 nm. The amount of protein present was determined by the amount of CBB bound to protein – which can be determined photometrically.

2.2 Experimental section

2.2.1 Synthesis of superparamagnetic IONPs

n-Octylamine-coated IONPs were synthesized following a published protocol with minor modifications [63]. Details can be found in the SI. Briefly, Ferric chloride ($FeCl_3$) is used as a salt precursor, ethylene glycol as both solvent and reductant. n-Octylamine functions as both a capping agent and a preliminary coating layer.

2.2.2 Synthesis of carboxyl functionalized IONPs

The functionalization of the IONP surface was performed by a silanization method described by Brullot *et al.* with some modifications [63]. In detail, newly synthesized IONPs (100 mg of) were dispersed in 100 mL of toluene by sonicating for two hours. After that, 0.5 mL of two silanes (PEG-silane and COOH-silane) with different volume ratios was added sequentially to the suspension, followed by the addition of one drop of pure acetic acid. The functionalization can be facilitated by one of the two following methods: a) sonication for two hours or b) magnetic stirring for 24 hours. After the reaction, an sufficient amount of heptane was added to induce precipitation and functionalized IONPs were collected by a magnet. Finally, the particles were washed three times with acetone and dried in a vacuum for 30 minutes.

A series of carboxyl functionalized IONPs was formed by varying the volume ratio of PEG-silane, from 10 % to 100 %, and samples were named by the percentage of COOH-silane used and the method (a or b) of synthesis. For instance, the C10a sample refers to IONPs coated by 10 % volume of COOH-silane (and 90 % volume of PEG-silane) and prepared by functionalization method a. The sample C10b was used for further study of the coupling process later.

2.2.3 Coupling functionalized magnetic nanoparticles to BSA protein

For the preparation of all solutions in this experiment, 2-(N-morpholino)ethanesulfonic acid (MES) buffer solution (50 mM, pH=5.5) was used as a solvent. Typically, 3 mg of functionalized MNPs were dispersed in 1 mL of MES buffer solution. To this suspension, 50 μL of EDC/MES (20 mg/mL) and 50 μL of NHS/MES (20 mg/mL) were sequentially added. Notice that the EDC solution must be used immediately after the preparation. Next, the reactants were mixed by vortexing, followed by addition of 40 μL of BSA protein MES (2.5mg/mL). Finally, the reaction mixture was mixed (by shaking or magnetic stirring) at room temperature for two hours. After reaction, the

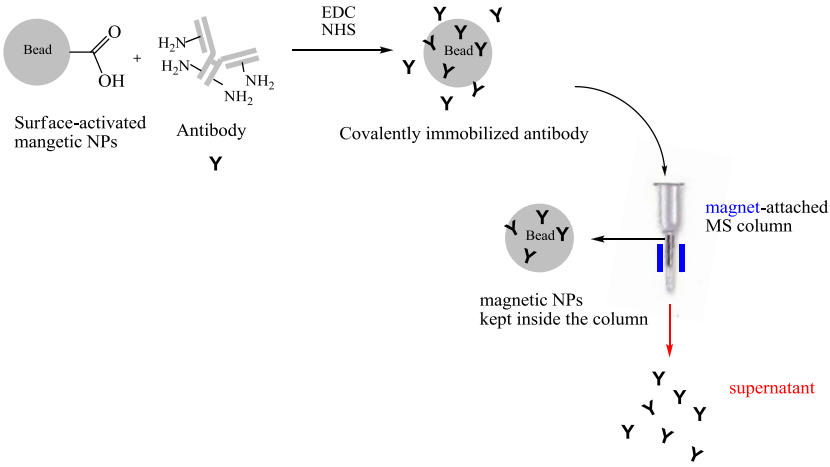

Fig. 2.3**:** Schematic overview of protein coupling and separation procedure. First, carboxyl-functionalized IONPs were covalently bound to protein via an amide bond in the presence of EDC and NHS. Then, the obtained solution was poured to a magnet-attached MS column. Nonreacted protein freely flowed through the MS column while protein-coupled IONPs were kept inside the column. Finally, these magnetic NPs were collected by the removal of the magnetic field followed by the addition of an appropriate solvent.

protein-coupled magnetic particles were magnetically separated by using a magnetic separation (MS) column, washed with PBS buffer solution three times and then stored in 5 ml of PBS solution at pH=7 (see Fig. 2.3).

2.2.4 Quantification of protein binding to MNPs by Bradford's method

Preparation of protein sample: All protein samples needed to be dispersed in 50 mM pH 5.5 MES buffer solution before pouring into cuvettes. Next, the volumes were diluted up to 600 µL by MES buffer solution, followed by the addition of 900 µL of CBB reagent. The mixture was mixed and then incubated for 30-60 minutes at room temperature. The absorption of all samples was recorded in the range from 500-700 nm with a reference cuvette containing 600 µL of MES and 900 µL of CBB. The increase at the wavelength of maximum absorption (normally 599 nm) was recorded.

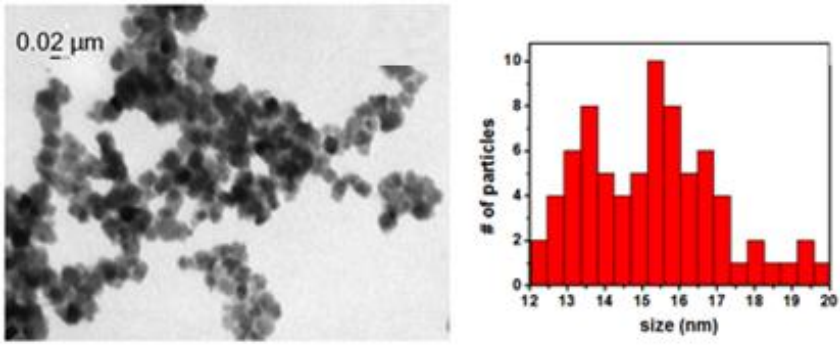

Fig. 2.4: TEM image of *n*-octylamine coated IONPs (left, scale bar 20nm) and a histogram of the size distribution (15.7 ± 2.4 nm) of *n*-octylamine coated IONPs (right).

Calibration curve: Standard protein samples containing free protein were also prepared in the same way as described above. We measured calibration curves and the results are shown in Fig. 2.S3 and 2.S4, SI.

Calculation of bound protein: After each coupling reaction between functional MNPs and BSA protein, protein bound MNPs were magnetically separated and dispersed in 5 mL of MES buffer solution. On the other hand, all supernatant solutions were also collected and diluted to 5 mL by MES buffer solution. The amount of reacted protein was determined directly by using a pellet sample or indirectly by using the supernatant as described above.

Due to the high sensitivity of Bradford's method, each experiment was repeated 2-4 times with different volumes of the sample (for instance: 150µL, 300µL, 450µL, 600µL), after which the average amount of BSA was calculated.

2.3 Results and discussion

2.3.1 Characterization of synthesized n-octylamine-coated IONPs

IONPs were synthesized based on forced hydrolysis [63]. XRD showed that the synthesized particles were composed of magnetite (Fe_3O_4) [63]. According to Brullot [69], DLS measurements of magnetite nanoparticles in toluene showed that the mean size of MNPs was 30 nm, resulting in a size of 27.2 nm of the magnetite core. A

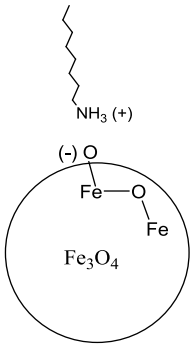

Fig. 2.5**:** The possible structure of *n*-octylamine-coated magnetite nanoparticle. The interaction between –OH groups on the surface and $–NH_2$ groups leads to the formation of the structure $O^{(-)}\ H_3N^+R$.

magnetic measurement, performed by vibrating sample magnetometer (VSM), showed a saturation magnetization (M_s) of 35 emu/g at 5T and room temperature (M_s value of bulk Fe_3O_4 is 92-100 emu/g [69]). Fitting the magnetization curve to a Langevin function resulted in a magnetic core size of 8.9 nm [69]. Fig. 2.4 shows a TEM image of *n*-octylamine-coated IONPs with a size distribution of 15.7 ± 2.4 nm. The difference in size determined by the different techniques is due to several reasons. DLS yields a hydrodynamic diameter which will always be larger than the diameter determined by TEM. Furthermore aggregation of particles could be another reason for the larger diameter in DLS. The size determined from the Langevin function is smaller than the TEM size which is explained by the fact that the particle is assumed to be spherical and only consists of magnetite. However, a magnetite particle consists of a magneto-crystalline core and a disordered shell of spins (magnetically dead layer) [155] and the latter does not attribute to the magnetization of the particle. So, the diameter calculated from magnetization data is only the size of the crystalline magnetite core.

Fig. 2.5 shows the structure of synthesized IONPs in which the surface of the particles is covered by a layer of *n*-octylamine due to the interaction between free -OH groups on the surface of IONPs and $–NH_2$ groups. Owing to the coating, IONPs can be dispersed in solvents such as methanol, toluene. These rather weak bonds also enable the coating ligands to be exchanged in the silanization reaction later.

The attachment of octylamine on the IONP surface was confirmed by investigating the infrared spectra of the coating (free octylamine) and the product (octylamine-coated magnetite particles). A FT-IR spectrometer equipped with a diamond ATR sample cell was used for all IR measurements in this study. These spectra are combined in Fig. 2.6, showing that the characteristic vibrations of octylamine all appear in the spectrum of

Table 2.1: Different vibration modes of the coating reagent (n-octylamine) and coated magnetite particles.

	IR vibration modes (cm^{-1})
n-Octylamine (free)	2955 (CH_3 as), 2921 (CH_2as), 2852 (CH_2 s), 1601 (NH bend in primary amine), 1465 (CH_2 bend), 1378 (CH_3 bend), 1072 (C-N) 795 (NH out of plane bending), 722 (long-chain band)
n-Octylamine-coated Fe_3O_4 (solid sample)	3300-3000 (NH…), 2920 (CH_2 as), 2849 (CH_2 s), 1651 (NH bend in primary amine), 1538 , 1454 (CH_2 bend), 1380 (CH_3 bend), 543 (Fe-O)

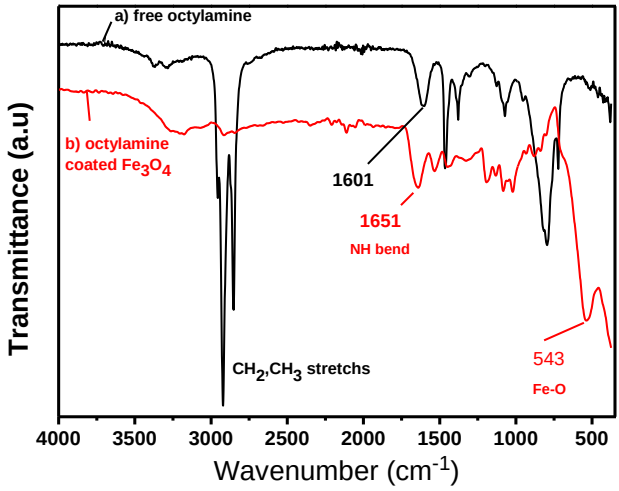

Fig. 2.6: Formation of Fe_3O_4 NPs in the presence of octylamine as a capping reagent. Spectra show the characteristic vibrations of free octylamine (a) and n-octylamine in the surface of the Fe_3O_4 surface (b).

the product, for example the NH bend in primary amines. The absorption of the NH bend in the primary amines was shifted from 1601 cm^{-1} (spectrum a) to 1651 cm^{-1} (spectrum b) due to the interaction with –OH groups on the surface. All main peaks of the functional groups were assigned and listed in Table 2.1.

2.3.2 Characterization of carboxyl functionalized IONPs

As mentioned in Section 2.2.2, the names of functional MNP samples are based on the percentage of the coating COOH-PEG used and the method of synthesis (a: ultrasonic method, b: stirring method). To investigate the effect of carboxylic groups on the stability and other properties of ferrofluids, C10a, C20a, C30a, C40a, C50a, C100a

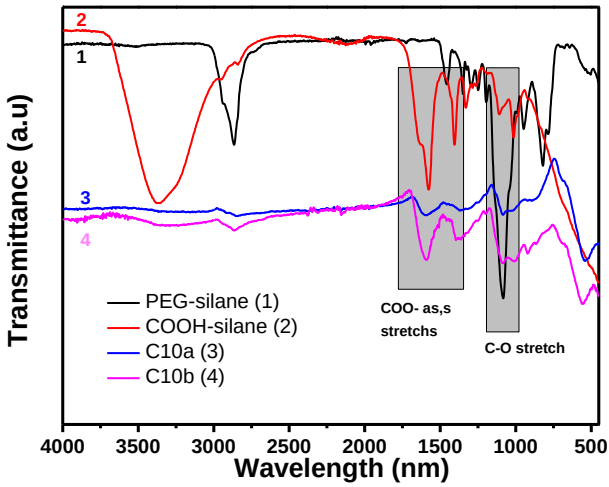

Fig. 2.7: FT-IR spectra of coatings PEG-silane, COOH-silane and functional MNPs C10a, C10b (spectrum 1,2,3,4 respectively).

Table 2.2: Vibrations of coating reagents (PEG-silane, COOH-silane) and functional MNPs C10a, C10b

	IR vibrations (cm^{-1})
PEG-silane (90%)	2865 (CH_2, CH_3),1456 (CH_2 bend), 1349 (CH_3 bend), 1083 (C-O), 820 (Si-O)
COOH-silane (45%)	3600-3000 (H_2O), 2956, 2840 (CH_2, CH_3), 1577(COO^- as), 1405 (COO^- s), 1109 (C-O)
C10a sample	2905, 2841 (CH_2, CH_3 stretches), 1590 (COO^- as), 1352 (COO^- s), 1085 (C-O), 540 (Fe-O-Fe, Fe-O-Si)
C10b sample	2864 (CH_2, CH_3), 1589 (COO^-, as), 1396 (COO^-, s), 1087 (C-O), 1010 (Si-O), 552 (Fe-O-Fe, Fe-O-Si)

samples were synthesized and characterized. In order to compare the efficiency of the two methods of synthesis, C10b and C100b samples were synthesized and their properties were compared to the properties of C10a and C100a samples. The properties of the functional MNPs were characterized by different techniques (IR spectroscopy, Dynamic Light Scattering, Zeta potential, Vibrating Sample Magnetometer).

FT-IR spectroscopy: Firstly, surface modification of magnetite NPs was confirmed by FT-IR spectroscopy. Fig. 2.7 shows the infrared spectra of coating reagents and functional MNPs: C10a and C10b samples (solid pellets). Peaks were assigned and listed in the Table 2.2, and the main characteristic peaks of the coatings also appear in

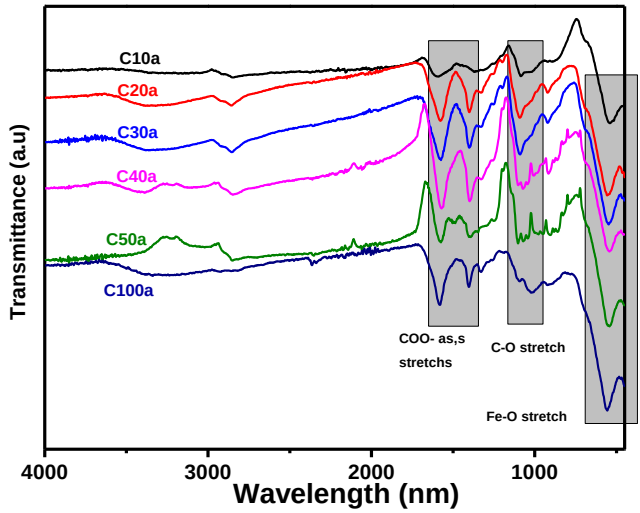

Fig. 2.8: Comparison of FT-IR spectra of functional MNPs synthesized from PEG-silane and COOH-silane coating reagents with different percentages of COOH-silane: 10%, 20%, 30%, 40%, 50%, 100% (respectively corresponding to C10a, C20a, C30a, C40a, C50a, C100a samples).

the spectra of functional MNPs, such as carboxylate (COO-) groups (anti-symmetric and symmetric stretches), ether (C-O) groups. The vibrations of Fe-O groups are found in the spectra of C10a and C10b samples.

Fig. 2.8 shows the combination of the spectra of various functional MNPs samples with the volume percentage of COOH-Silane in the range from 10-100%. Characteristic vibrations of alkyl chains, carboxylate groups, ether groups and Fe-O groups were all found.

Transmission electron microscopy: A TEM image of C10a particles is shown in Fig. 2.9. The image indicates that the particles synthesized by sonication were not homogeneous. In general, the size of these particles is around 15 nm.

Dynamic Light Scattering and Zeta Potential: The stability of ferrofluids is an important parameter for applications, hence their properties were characterized by dynamic light scattering (DLS) and ZP. Table 2.3a, shows the hydrodynamic diameter and zeta potential of functional MNP samples synthesized. The hydrodynamic diameter of ferrous fluids is higher than the size measured by TEM image due to the layer of solvent (water) surrounding the MNPs. As shown in Table 2.3a, no relation between hydrodynamic diameter and the percentage of COOH-silane is found. This is

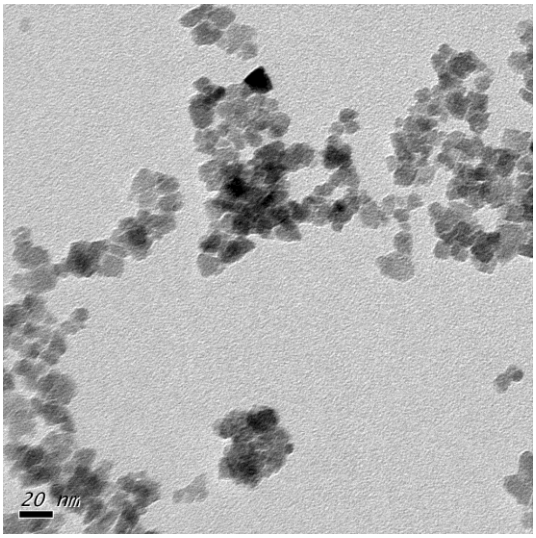

Fig. 2.9: TEM image of C10a samples.

still an unsolved question and further study needs to be done to clarify this phenomenon. However, with a hydrodynamic diameter varying from 27-52 nm, these systems are suitable for the coupling of proteins or other bio-entities.

Zeta potentials of ferrofluids are negative (from -22 mV to -48 mV), indicating a high degree of stability. Especially the C100 samples are very stable (ZP_{C100a}= -48mV, ZP(C100b= -35mV), explained by many negatively charged groups on the surface of MNPs. Notice that the functional group on the particles' surface is carboxylate (COO-) which is strongly solvated by water molecules in aqueous solutions. A decrease in the values of ZP was found when storing the MNPs in the solution, possibly due to the reaction between carboxylate groups (-COONa) and carbon dioxide (CO_2) in the air leading to the formation of -COOH groups. However, these samples are still stable after two weeks (Table 2.3b). Both synthetic methods yield particles with considerably different ZP. For example, the ZP of C100a solution is more negative than the value of C100b solution, suggesting that C100a sample in the solution is more stable than C100b and a thicker coating layer is formed on C100a particles. This is also confirmed by DLS (Table 2.3b).

For biomedical applications, the particles need to be stable under various pH conditions. So, the stability of the ferrous fluids was investigated in a pH range from 4 to 10. The pH of the solution was adjusted by 0.01M NaOH solution and 0.01M HCl solution. Before adjusting the pH, 1mM NaH_2PO_4 solution was added to the ferrofluids. By this way, the ferrofluid was buffered with 1 mM NaH_2PO_4. Note that

Table 2.3: Properties of ferrofluids based on different kinds of carboxylic functional MNPs, depending on i) the percentage of COOH-silane component and ii) the method of synthesis.

a)

Samples 0.5 mg/mL	Hydrodynamic diameter (nm)	ZP (mV)
C10a	52	-34
C20a	32	-23
C30a	34	-22
C40a	25	-24
C50a	27	-38
C100a	49	-48

b)

Samples (c=0.5 mg/mL H_2O)		100% COOH-silane	
		C100a	C100b
Hydrodynamic diameter (nm)		49	17
ZP (mV)	Newly synthesized	-48	-35
	After 14 days	-20	-21
pH		9	10

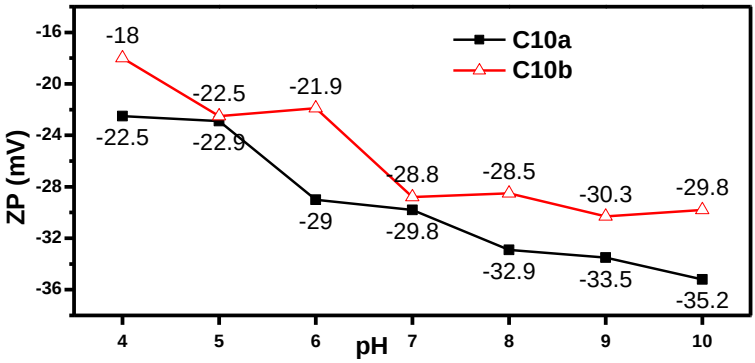

Fig. 2.10: Zeta potential values of C10a and C10b suspensions as a function of pH.

the addition of NaH_2PO_4 could cause a slight decrease in ZP. C10 samples were chosen for this study because they are the most appropriate samples to couple with proteins as explained in Section 2.2.3). Other samples have much more carboxylic groups, leading to the high possibility to form cross-links between protein and NPs.

Data of zeta potentials of C10a and C10b samples in the pH range from 4-10 are shown in Fig. 2.10. At a concentration of 0.0625 mg/mL, the values of the hydrodynamic diameter of all samples are approximately 40 nm, suggesting that they

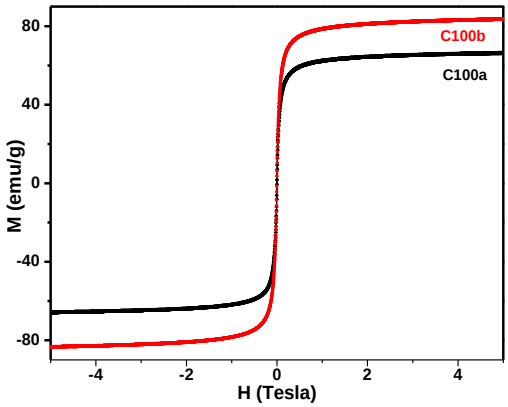

Fig. 2.11: Magnetization curves of C100a and C100b samples

are not affected much by the pH. Both C10a and C10b samples are stable in solution with zeta potentials ranging from -22.5 to -35.2 mV (C10a) and from -18.0 to -29.8 mV (C10b). Similar to the zeta potentials of C100a and C100b shown above, C10a suspensions were slightly more stable than C10b ones. The data also show a decrease of zeta potentials as the pH increases. This is expected because more carboxylic groups will convert to charged carboxylate groups since the solution is more basic.

Vibrating Sample Magnetometer: Fig. 2.11 shows magnetization curves of the C100a and C100b samples at 298K, indicating superparamagnetic behavior of theses functionalized IONPs. The high values of saturation magnetization (M_s(C100a) = 65.41 emu/g, M_s (C100b) = 83.81 emu/g) suggests the presence of magnetite Fe_3O_4 in the core. Especially, the M_s value of C100b particles is close to the value of bulk magnetite (92-100 emu/g) [156].

2.3.3. Quantification of BSA binding onto functionalized IONPs

During the coupling of protein to functional IONP samples, there was a high tendency to form cross-links between magnetic NPs and BSA molecules. This readily happened especially with the magnetic particles having many carboxyl groups on the surface. In this case, several functional IONPs are linked together through BSA molecules, forming a heavy conjugate which was precipitated out of the solution. For this reason, IONPs functionalized with only 10% COOH-silane and 90% PEG-silane were chosen for further study of the coupling process later. The sample C10b was used instead of the sample C10a because stirring process (method b) rendered the solution mixed

Table 2.4: The reaction conditions of some coupling experiments (EDC solution: 20mg/mL; NHS solution: 20mg/mL ; BSA solution (in MES) 2.5 mg/mL).

	Amount of C10b sample	Volume of EDC solution	Volume of NHS solution	Amount of BSA	Time reaction	Method of coupling
Ex1	3 mg	50 µL	50 µL	100 µg	2h	Shaking
Ex2	3 mg	50 µL	50 µL	100 µg	2h	Stirring

better. This leads to a formation of more uniformly coating layer on the surface of IONPs.

Before the determination of the amount of bound protein, a test sample consisting of a mixture of BSA and functional MNPs was used to check the accuracy of the calibration curve in the presence of magnetic NPs. The experiment and the results are shown in SI, confirming that the presence of magnetic NPs do not affect the results of Bradford assay.

BSA molecules were coupled to the C10b sample in the presence of activating substances EDC and NHS. After the reaction, the particles were separated, washed and stored in PBS buffer solution at pH=7. The hydrodynamic diameter was 36 nm and the zeta potential -25 mV.

Through the reaction, it is important to avoid cross-linking between MNPs and protein molecules. Because there are many carboxyl groups on the MNPs surface and many amine groups in BSA, several MNPs and several protein molecules have a tendency to react together, forming very heavy particles. In this case, these particles will precipitate and cannot be dispersed again. It is clear that there are many parameters that can affect the coupling, such as the concentration of functional MNPs, the amount of reactants MNPs and BSA, the amount of EDC and NHS, reaction time. For these reasons, many experiments were carried out to find the optimal conditions of the coupling process as described in Section 2.2.3. The optimized conditions are given in Table 2.4.

After the reaction, all magnetic particles were separated, and then the volume of the BSA-MNPs solution and the volume of the supernatant were increased to 5mL. Different aliquots of each protein sample (in the solution of protein – coupled MNPs and the supernatant) were used for Bradford assay because the method is very sensitive. The amounts of BSA in 5 mL solution were calculated by using the calibration curve and are listed in the Table 2.5.

Table 2.5: Amount of BSA coupling to 3 mg MNPs was determined by Bradford assay. The assays were performed in both the pellet and the supernatant after coupling reaction.

Experiment	Existing form of BSA	Volume of protein sample (mL)	Total amount of coupled BSA in the pellet (µg)	Total amount of free BSA in the supernatant (µg)	Total amount of BSA (µg) coupling to 3 mg MNPs (% BSA reacted)
Ex1	Coupled to MNPs	0.30	63		58.6 ± 4.1
		0.45	60		
		0.60	52.5		
	Free in supernatant	0.15	56.7	51.7 ± 8.3	48.3±8.3
		0.30	63.3		
		0.45	44.4		
		0.60	42.5		
Ex2	Coupled to MNPs	0.15	73.3		63.1 ± 6
		0.30	65		
		0.45	60		
		0.60	54.2		
	Free in supernatant	0.15	50	45.6 ± 3.9	54.6±3.9
		0.30	45		
		0.45	48.9		
		0.60	38.3		

In Ex1 and Ex2, the calculation of the amount of BSA bonded to the MNPs showed a good agreement between the two methods of determination (direct and indirect ones). The amounts of reacted BSA ranged from 48.3-58.6 µg in Ex1 and from 54.6-63.1µg in Ex2. On average, there is 18.2-21.0 µg of BSA on the surface of 1 mg MNPs in Ex2.

Note that the experimental conditions of Ex1 and Ex2 were the same but the method of coupling differs. So, the higher amount of reacted BSA in Ex2 indicates that the stirring method is preferred for the coupling due to its higher efficiency.

Although only the coupling and determination of BSA were investigated, this work can be extended to other types of proteins such as antibody/antigens.

2.4 Conclusions and outlook

2.4.1 Conclusions

The goals of this chapter were the synthesis of functional magnetic nanoparticles (MNPs) and using these particles to couple to proteins (Bovine serum albumin). One of the main issues was to quantify the amount of protein bounded on the magnetic particle surface.

First, magnetite nanoparticles (with a coating layer of n-octylamine) were synthesized by the forced hydrolysis method. Next, the particles were functionalized to yield MNPs with carboxyl functionalities on their surface. The MNPs dispersed well in water yielding very stable ferrofluids. The structure of the coating layer of the MNP surface was studied by FT-IR spectroscopy, the sizes were confirmed by TEM, magnetization curves were recorded by VSM and the properties of ferrofluids were investigated by DLS and ZP. At the end, we were able to successfully couple BSA to the MNPs giving conjugates that were stable in PBS buffer solution. Using the Bradford assay, a BSA calibration curve was build and used to detect BSA with a detection range of 0.5-15µg BSA. For quantification of coupled BSA on the MNP surface, Bradford assays were performed in both the suspension of protein - MNPs conjugates and the supernatant. Generally, about 20 µg of BSA could be bound to 1 mg of MNPs.

2.4.2 Outlook

A series of functional MNPs were synthesized based on two coating reagents: PEG-silane and COOH-silane and the method of synthesis (sonicating and stirring method). Several characterizations such as DLS and ZP measurements were done in order to explore the dependence of the properties of particles on their coating components. However, no clear relation was observed. Further studies are needed to clarify.

In general, the amount of BSA coupled to MNPs was quantified, however there are still questions to answer. Other techniques used to determine protein need to be applied and compared with the Bradford's method. One possible approach is using fluorescent dyes to label protein and the dye-tagged protein - MNP conjugation will be determined by fluorescence measurements.

2. 5. Supporting information

A. Experimental section

Materials: All chemicals were purchased from standard supplies and used as received without further purification. Milli-Q water (18 MΩ cm^{-1}) was used to prepare all aqueous solutions. Protein bound MNPs were washed by 50 mM pH7 PBS buffer solution and also stored in this kind of buffer solution. 50 mM pH 5.5 MES buffer solution was used as solvent in all experiments to determine the amount of protein in all protein samples.

Magnetic columns (MS columns) were purchased from Miltenyi Biotec.

Equipment and characterization: Transmission electron microscopy measurements were performed on a 80 kV Zeiss EM-900 using 300 mesh Formvar-coated copper grids. Distribution data were calculated by ImageJ software. UV–Vis Spectrometry was performed on a Perkin Elmer Lambda 900 spectrometer. Magnetic properties of the nanoparticles were characterized by a superconducting quantum interference device magnetometer (SQUID, Quantum Design MPMS XL-5). Vibrating sample magnetometry (VSM) experiments were conducted on a VSM Maglab setup from Oxford Instruments. Fourier transform infrared (FT-IR) spectra were obtained using a Bruker Alpha FT-IR spectrometer equipped with a Platinum ATR module. Dynamic light scattering and zeta potentials were measured on a Brookhaven 90plus particle analyzer. The internal detector was positioned at 90°.

Synthesis of superparamagnetic IONPs: The synthesis method of magnetite nanoparticles is based on the forced hydrolysis technique described by Brullot *et al.* [63]. Ferric chloride ($FeCl_3$) is used as a salt precursor, ethylene glycol as a solvent and a reductant. n-Octylamine functions as both a capping agent and a preliminary coating layer. Typically, a ferric solution was prepared by dissolving 2.4 g of anhydrous $FeCl_3$ in 10 mL of ethylene glycol and 3.5 mL of Milli-Q water at 50 °C. On the other hand, 25 mL of octylamine was dissolved in 37.5 mL of ethylene glycol, then the solution was heated to 150 °C. To this solution, the ferric solution was added, and then the mixture was further heated, refluxed at 180 °C for 24h. After the reaction, the particles were precipitated by using a magnet, quickly washed with acetone and dried in vacuum to obtain a powder of iron oxide with a typical quantity of 1 g.

It is important to note that the synthesized IONPs are coated by a layer of n-octylamine. Therefore, if particles are washed too many times with acetone, the layer coating will dissociate in acetone. IONPs will loose the coating layer and therefore cannot be redispersed in toluene later.

B. Bradford's method

Bradford's method is one of the most common assays for protein quantification because of its rapid and sensitive characteristics.

Principle of Bradford's method: The Bradford reagent contains the dye Coomassie Brilliant Blue G-250 (CBB) that can simultaneously exist in three different forms: anion, neutral species and cation with different absorption maximum (595, 650 and 470 nm, respectively) [154]. The structure of neutral form is shown in Fig. 2S.1.

Existing forms:	Anion (blue) ⇌	Neutral species (green) ⇌	Cation (red)
Absorption maximum:	595nm	650 nm	470nm

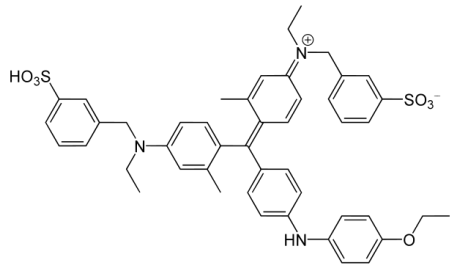

Fig. 2.S1: The structure of the neutral form of CBB. The anion will be obtained when the acid dissociation occurs at -SO_3H group.

The concentration ratio of existing forms of the dye CBB is pH-dependent in which CBB is almost entirely doubly protonated (cationic form) at pH 0.30, and deprotonated (anionic form) at pH 1.25 [154], [157]. So, in the acidic environment of protein reagent (pH=0.5), only cationic and neutral forms exist and the presence of anionic form is not found.

Because only anionic species of CBB G-250 are able to bind to protein due to their electrostatic and hydrophobic interaction [154], [157], the addition of protein to CBB solution leads to the conversion of neutral and cationic species to anionic species. As a result, the absorption maximum of the dye is shifted from 465nm (cation) and 650 nm (neutral species) to 595 nm. The number of proteins can be determined from the

increase in absorbance at 595 nm. The protein dye complex has a high absorption coefficient, explaining the high sensitivity of the method.

Preparation of protein reagent (CBB solution): 100 mg of CBB G-250 was dissolved in 50 mL of 95% ethanol. To this solution, 100 mL of 85% (w/v) phosphoric acid (H_3PO_4) was added. Then, the volume is filled up to 1 L with Milli-Q water to form a solution of 0.01% (w/v) CBB, 4.7% (w/v) ethanol, and 8.5% (w/v) phosphoric acid [153].

Calibration curve: Standard protein solutions were prepared following the procedure in Section 2.2.4 (preparation of protein sample). Twelve standard protein solutions containing from 0.5 to 15µg of BSA were prepared from 25µg/mL BSA solution in MES as follows:

Table 2.S1: Preparation of standard protein samples from 25µg/mL BSA solution.

Standard samples	Volume of 25µg/mL BSA solution (µL)	Volume of 50 mM pH 5 MES buffer solution added (µL)	Amount of protein (µg)
STD1	20	580	0.5
STD2	40	560	1.0
STD3	60	540	1.5
STD4	120	480	3.0
STD5	180	420	4.5
STD6	240	360	6.0
STD7	300	300	7.5
STD8	360	240	9.0
STD9	420	180	10.5
STD10	480	120	12.0
STD11	540	60	13.5
STD12	600	0	15.0

To each standard protein sample, 900µL of the protein reagent (CBB solution) was added and its absorption was measured with a reference cuvette containing 600 µL of MES and 900 µL of CBB. The absorbance values at maximum wavelength (normally 595nm) were plotted versus the amount of protein (µg), forming the BSA calibration curve.

Fig 2.S2a shows the UV-Vis spectra of CBB in the absence of protein and in the presence of protein with a reference cuvette of water. The spectrum of CBB has a maximum wavelength at 650 nm, referring to the absorption maximum of neutral

species. No absorption maximum at 595 nm was recorded, meaning there is no the presence of anionic species (or negligible amount) in the protein reagent.

When adding proteins, the absorbance of the solution increased and the absorption maximum was gradually shifted to the wavelength of absorption maximum of the anionic species. This is explained by converting a part of the neutral species to anionic ones when adding protein due to the fact that anionic species can make strong interactions with protein molecules.

Fig 2.S2b shows a similar result in which the reference cuvette consists of MES buffer solution and CBB reagent. Absorption maxima are found at 588 nm in all spectra corresponding to the formation of anionic species.

The values of the absorption maximum of standard samples (at 588 nm) are listed in Table 2.S2 and are plotted versus the amount of BSA protein (µg) (Fig 2.S3.), creating the BSA calibration curve.

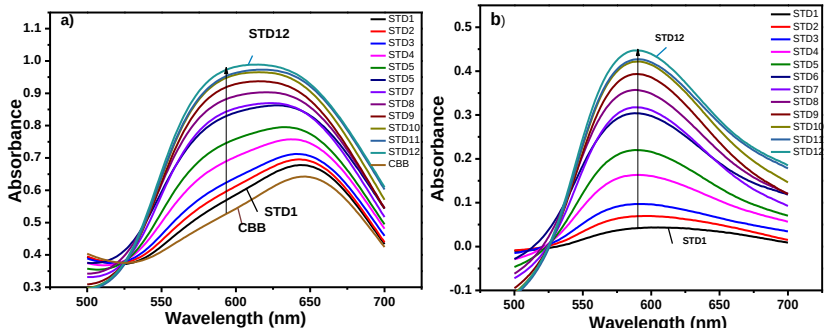

Fig 2.S2: The result of the Bradford assay of standard samples with reference cuvette of water (a) or the mixture of MES(600µL) and CBB(900µL) (b).

Table 2.S2: The absorbance of standard samples in Bradford assays at absorption maximum

Standard samples	Amount of protein (µg)	Absorbance at maximum wavelength (588nm)
STD1	0.5	0.03872
STD2	1.0	0.0734
STD3	1.5	0.10604
STD4	3.0	0.16208
STD5	4.5	0.24163
STD6	6.0	0.32494
STD7	7.5	0.33816
STD8	9.0	0.38618
STD9	10.5	0.42296
STD10	12.0	0.44394
STD11	13.5	0.4286
STD12	15.0	0.45895

There is a small non linear trend at the end of the curve (Fig 2.S3a), however the high correlation factor (R^2=0.993) proves the high accuracy of the calibration.

With the data from six first standard samples, the calibration curve is linear (Fig 2.S3b). This calibration was used to calculate the amount of protein in Bradford assays.

$$y = 0.046 * x + 0.022 \quad (R^2=0.9942) \quad (2.1)$$

where : y : the absorbance at absorption maximum, x: the amount of BSA (µg)

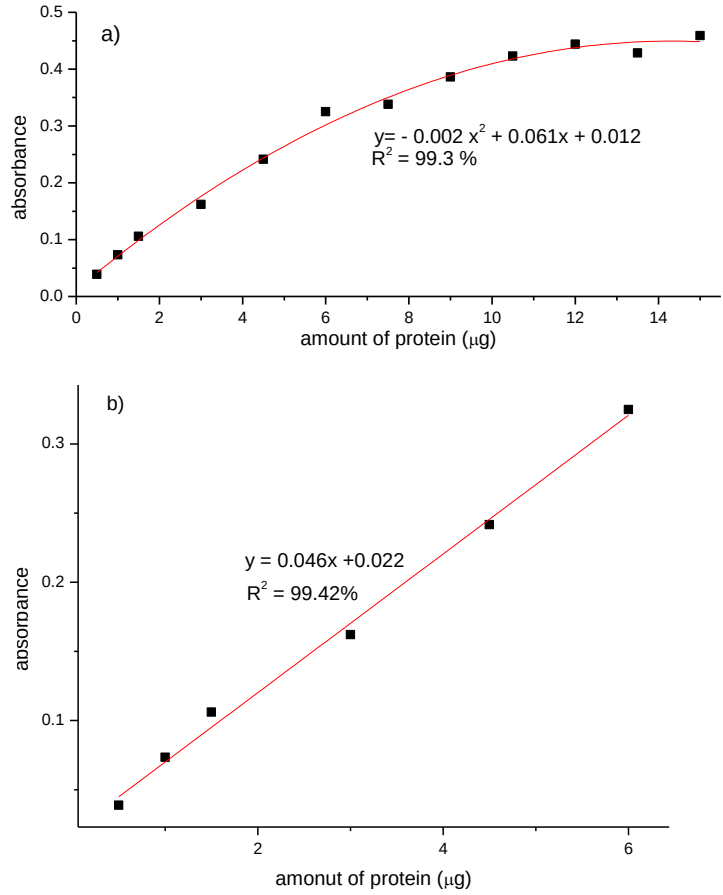

Fig 2.S3: The calibration curve of BSA in Bradford assays (buffer MES 50mM, pH 5.5) in the range a) from 0.5-15µg BSA, b) from 0.5-6µg BSA

Note that these experiments were carried out in MES buffer. Every solution was prepared in MES, containing protein and functional MNPs solutions. The Bradford assays can be performed in other conditions, such as PBS (pH 7.0). In this case, new calibration curves should be measured again.

Test sample for calibration curve: A test sample consists of a mixture of 3 mg of functional MNPs (C10b) and 100 µg of BSA protein. These components were dissolved in MES and the solution was diluted up to 5 mL. Different quantities (0.15mL, 0.3mL, 0.45mL and 0.6mL) of the test sample (respectively corresponding to 3µg, 6µg, 9µg and 12µg BSA) were chosen to do Bradford experiment. Then, UV-Vis spectra were compared to the spectra of standard samples containing the same amount of protein (STD4, STD6, STD8, STD10). These spectra are shown in the Fig. 2.S4. The similarity of these spectra suggests: i) the MNPs have no contribution in these UV-Vis spectra) and ii) the high accuracy of BSA calibration curve.

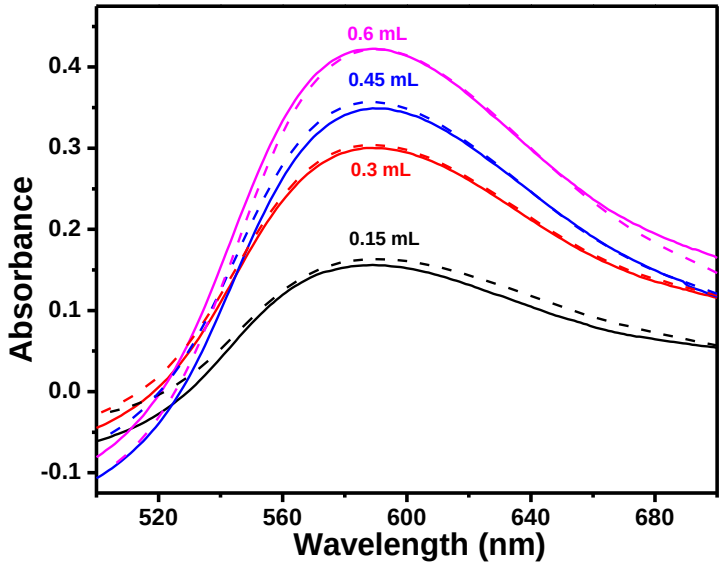

Fig. 2.S4: Comparison of results of Bradford experiment for test samples and standard samples containing the same amount of BSA (solid lines refer to spectra of test samples, dash lines refer to spectra of standard samples)

Chapter 3

Synthesis of iron oxide/gold core/shell nanoparticles

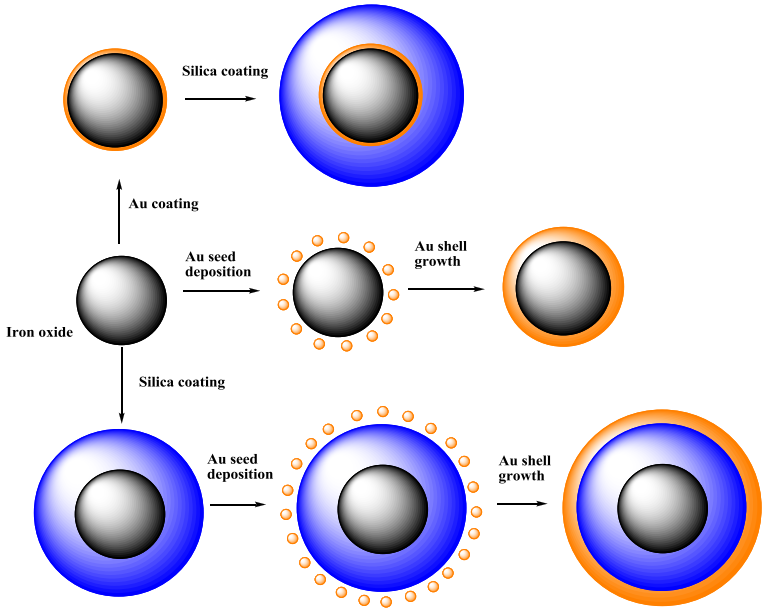

Dr. M. Bloemen prepared oleic acid coated IONPs and helped with the synthesis of gold coated IONPs in the organic phase. Prof. Dr. J. Billen performed TEM measurements.

Abstract

In this chapter, we present the synthesis of water-dispersed gold nanoshells by two approaches: synthesis in aqueous phase and organic phase. Gold nanoshells show surface plasmon resonance peak varying from 528 nm to ~700 nm. Besides, mesoporous silica component was also introduced to design versatile multilayer nanoshells. By combining many interesting properties into one single particle, the obtained nanostructures show their potential in advanced applications.

3.1 Introduction

Magneto-plasmonic nanostructures combine magnetic and plasmonic properties in one material. Although either magnetic [5], [50], [64], [85], [95], [99], [141], [158]–[163] or plasmonic [134], [164]–[169] nanoparticles (NPs) have been intensively studied in biomedical applications for a long time, magneto-plasmonic nanostructures have been given attention only recently. The integration of magnetic and plasmonic components results in many interesting properties such as a strong interaction with light and external magnetic fields. Fig. 3.1 shows the interaction of magneto-plasmonic core-shell nanoparticles with photons, AC magnetic fields and DC magnetic fields. The characteristic feature of the plasmonic component is its interaction with light. Incident photons can be: i) absorbed to generate localized surface plasmon resonances (LSPR) and generate heat [170] or ii) scattered to generate scattering contrast [171]. External magnetic fields can be used to control the movement of particles and provide extra contrast in magnetic resonance imaging (MRI) [170]. AC magnetic fields can also be absorbed to generate heat through several loss processes [20].

Interestingly, the hybrid materials do not only possess the properties of each component, but some properties are also enhanced. For example, oscillating magnetic fields with frequencies of kHz to MHz induce hyperthermia in Fe_3O_4 nanoparticles [13], [146] whereas the hyperthermia can be achieved at lower frequencies (44 Hz to 430 Hz) for Au–Fe_3O_4 core/shell nanocomposites [20]. Au NPs smaller than 2.5 nm do not show LSPR bands but 0.5 nm Au shells can exhibit LSP resonances [23]. Furthermore, Au NPs show a plasmon peak around 520 nm [121] whereas magneto-plasmonic nanostructures show plasmon peaks in a wide spectral range (530-1200 nm) [136], [172].

To design multifunctional (magnetic and plasmonic) nanostructures, it is possible to perform one of the following approaches: [61]

- Assembling several mono-functional entities in a larger assembly.
- Integrating the required functional components into a single entity.

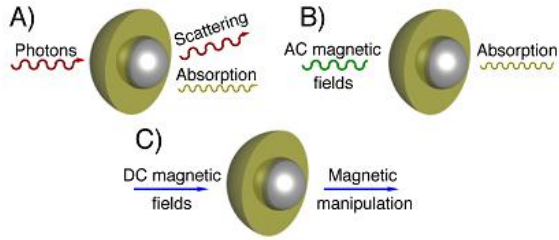

Fig. 3.1: Magneto-plasmonic core-shell nanoparticles and their interactions with light (A), AC magnetic fields (B) and DC magnetic field (C). Reprinted with permission from Ref. [183].

Some examples of the first approach are: Au NPs and iron oxide nanoparticles (IONPs) that are embedded in a polymer or silica coating [173]–[175], or the assembly of Au NPs and IONPs by a linker composed of bifunctional small molecules to make nanoparticle multilayers [176]. In the second approach, two components in the core-shell particles are very close, leading to a maximal interaction between magnetic and plasmonic components. Moreover, many applications in biomedicine, such as controlled drug delivery, diagnostic and therapy require the movement of these nanostructures as single entities. Therefore, we opted for the synthesis of iron oxide-gold core-shell nanoparticles (IOGNPs). Furthermore, for biomedical applications, it is critical that the synthesized IOGNPs are biocompatible and water-dispersible. Finally, the shell thickness needs to be controlled to obtain a tunable plasmonic peak. Formation of water-dispersed IOGNPs can be achieved by two general approaches: i) direct synthesis of Au nanoshells in aqueous phase, or ii) synthesis of Au nanoshells in an organic phase followed by phase transfer to water.

3.1.1 Synthesis of Au nanoshells in water

For the first approach, Au nanoshells are formed by the reduction of Au precursor ($HAuCl_4$) onto the surface of IONPs in the aqueous medium. Before Au shell deposition, IONPs need to undergo a surface functionalization. The purpose of adding a coating layer on the surface of the IONPs is:

- The functional groups are able to bind Au^{3+} ions before the reaction and gold after the reaction. As a consequence, the reaction preferably takes place on the surface of IONPs to form Au nanoshells instead of somewhere in the solution to form isolated Au NPs.

- To avoid the migration of Au atoms into the iron oxide core [33]. This migration would lead to a distortion of the core and therefore significant decrease of the magnetic properties.

The coating layer can be composed of i) polymers [146], [177]–[179], ii) small molecules [33], [75], [85], [89], [101], [180], or iii) a (mesoporous) silica shell [102], [173], [181]. Fig. 1.13 showed an overview of surface functionalization of IONPs.

i) The use of polymers as coating agents are favorable for some applications because of their biocompatibility. However, the disadvantages in control of the shell thickness and the leak of the core (due to the weak interaction between IONPs and polymers) limit their potential in advanced applications. Therefore, there were only few cases in which polymers were reported as coating agents for gold coating, such as polyaniline [177] and poly-L-histidine [178].

ii) Contrary to polymers, organic molecules such as alkoxysilane, carboxylate, phosphonates are widely used in functionalization because they bind covalently to IONPs. Moreover, these organic molecules can form a thin coating layer which has no influence on the magnetization of IONPs. The availability of many organic molecules as coating agents is also an advantage because they can provide different functional groups (such as amino, thiol, carboxylic, hydroxyl) for different purposes. For gold coating, these organic molecules often have two functional groups: one is able to bind to IONPs (carboxylate/phosphate/catechol/alkoxysilane) and another is able to coordinate to gold. Although both amino and thiol groups have high affinity for gold, only amino-terminated reagents are often used to form coating layers. This is due to the low polarity of thiol groups leading to a low solubility of functionalized particles in aqueous medium. Some common amino-terminated reagents are 3-aminopropylphosphonic acid [33], dopamine [92], [93] and alkoxysilane [100], [101], [182].

iii) Prior to the gold coating process, silica or mesoporous silica (mp-SiO_2) shells with different thickness can also be used as coating agents for IONPs. The most popular method used to grow a silica shell is the Stöber method based on the hydrolysis and condensation of a silica precursor such as TEOS/EtOH in the presence of a base (NH_3, NaOH,…) [103]. During the growth of the silica shell, a large excess of surfactants (e.g., cetyltrimethylammonium bromide (CTAB)) [7], [104], [105]) can be added to form mp-SiO_2 shells which can be exploited as fluorescent labeling or drug delivery carriers [7], [181].

The presence of SiO_2 shells increase the particle size before gold coating, leading to an increase of IO-SiO_2 core/Au shell ratio. The increase of core/shell ratio causes a red-shift of the LSPR band of the Au shells. The position of the band can vary from the visible to the near-infrared (NIR) region [136], [183]. For example, IOGNPs exhibit a

Scheme 3.1: Schematic of gold coating approach using gold seeds.

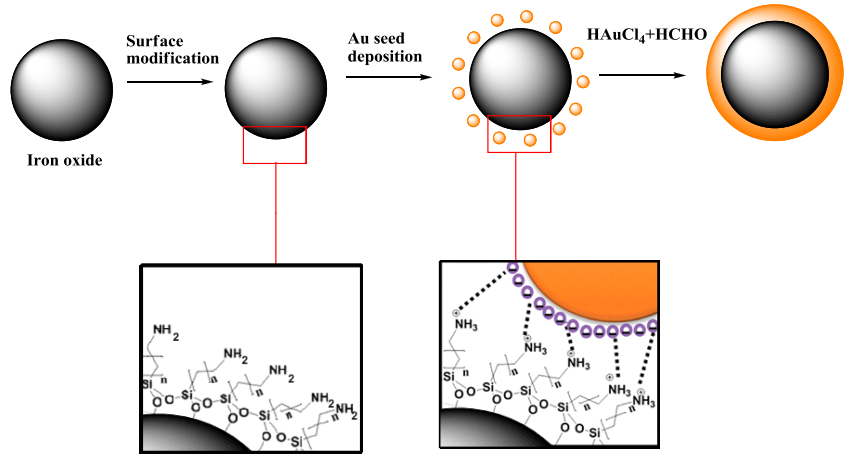

clear SP band at 535 and 550 nm for different core sizes and Au shell thickness [184], [185] whereas iron oxide – silica – gold NPs might exhibit a plasmonic peak at 1200 nm [136] (see Section 1.4.3). The red-shift of the plasmonic peak to the NIR region plays an important role in optical biomedical applications such as *in vivo* optical imaging and photothermal therapy [134], [186], [187] because water and most biological materials including hemoglobin, are transparent (in active) in NIR region [188].

In order to prepare Au nanoshells, $HAuCl_4$ is reduced with relatively strong reductants such as citrate [189], [190] or hydroxylamine (NH_2OH) [171], [191]. Furthermore, the reaction can be facilitated by sonication as well [33], [192] . Au atoms prefer to deposit on the surface of NH_2-functionalized IONPs because amino groups can bind to Au^{3+} before the reaction and newly formed Au shells after the reaction. However, during the reaction, there is always the possibility that isolated Au NPs can be formed in the solution instead of Au nanoshells and as a consequence the product is always a mixture of Au NPs and Au nanoshells.

To avoid these disadvantages, we opted for the approach described in scheme 3.1. Briefly, small negatively charged Au seeds (1-3 nm), prepared by the Duff method [193], are attached on the surface of NH_2-functionalized IONPs before undergoing the gold coating process. Because alkylamines mainly exist in positively charged form ($R\text{-}NH_3^+$) at pH<10, the dominant interaction between Au seeds and NH_2-functionalized IONPs is electrostatic rather than coordinative in nature [194]. Also according to Westcott [194], small Au seeds can strongly attach to the surface of the IONPs and the

Scheme 3.2: The schematic of gold depositing onto IONPs in the organic phase. Reprinted with permission from Ref. [23].

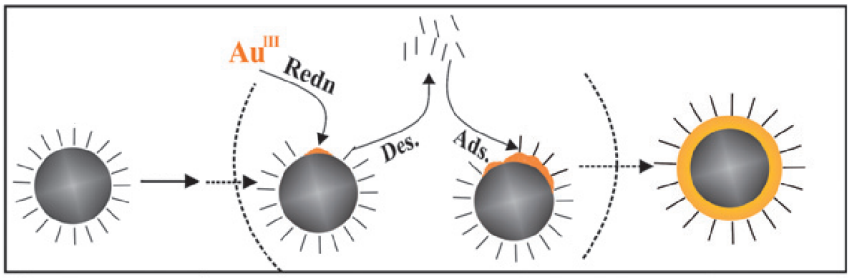

coverage ratio can go up to ~ 30%. These small Au seeds do not only act as seeds for the growth of nanoshells, but also act as the catalyst for the reduction. Hence, a weak reductant such as HCHO [101], glucose [93], CO [100] is sufficient for the reaction. The use of a weak reductant can be beneficial as the formation of Au nanoparticles in the solution is avoided. Moreover, the shell thickness can be easily controlled by varying the amount of reactants.

3.1.2 Overview of synthesis of Au nanoshells in an organic phase

For the second approach, synthesis of Au nanoshells in an organic phase, a well-known method is the direct growth of Au shells on the surface of IONPs at elevated temperature [23]. First, oleic acid-coated IONPs are synthesized that act as seeds for gold deposition. Then, gold is deposited onto the surface of the IONPs by the reduction of gold (III) acetate at 180-190 ^{o}C in the presence of oleylamine and oleic acid as capping agents. This method is used to synthesize highly monodisperse nanoparticles [23], [184], [185]. The reaction is illustrated in Scheme 3.2.

The deposition of gold onto IONPs takes place together with the partial desorption of surfactants (oleic acid, oleylamine) from the IONPs, followed by re-adsorption of surfactants onto the gold surface. The temperature plays an important role here because all processes are thermally activated. More reduced gold (III) ions lead to the formation of a complete Au nanoshell and the latter is surrounded by a coating layer of oleylamine due to the high affinity of Au for amino groups. This coating layer helps IOGNPs to disperse well in organic solvents (heptane). This approach can be applied to synthesize iron oxide-gold NPs with a core size from 5-15 nm and a shell thickness from 0.5–2.0 nm [23]. The thickness of Au nanoshells is tunable by changing the concentration of Au precursor and the reaction time [23]. However, for biomedical applications, hydrophobic Au nanoshells need to be transferred from the organic phase to an aqueous phase.

Scheme 3.3: Summary of syntheses of magnetic core-shell nanoparticles starting from IONPs.

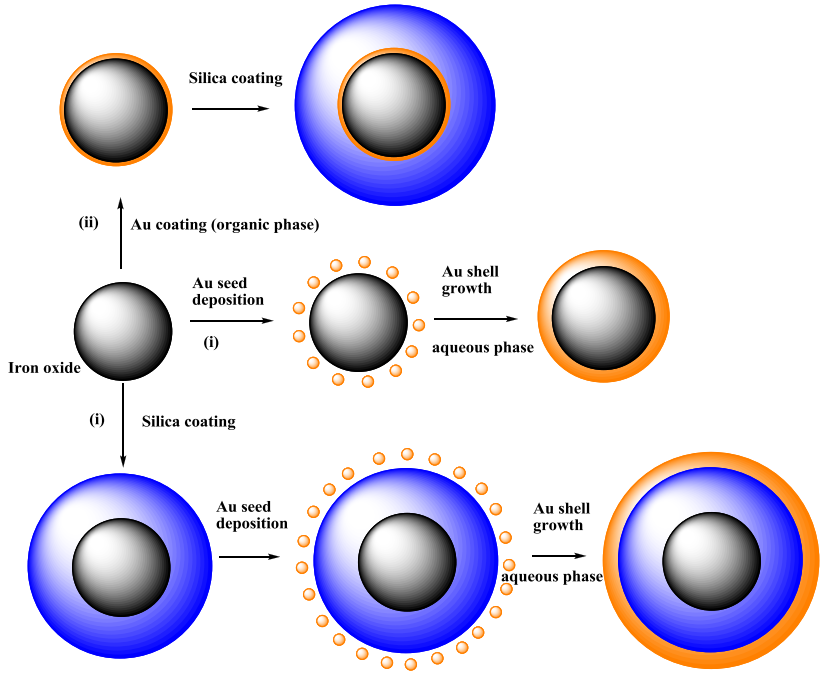

Here, the synthesis of IOGNPs following two approaches: synthesis in the aqueous phase (i) and organic phase (ii). Furthermore, iron oxide – gold – silica multilayer nanoshells (IO-Au-SiO_2 NPs) were prepared. Although the synthesis of gold nanoshells with tunable plasmon properties has been intensively studied since first synthesized by Oldenburg in 1998 [195], to our knowledge, very little work in the integration of gold nanoshells, mesoporous silica shells and magnetite core in one single particle has been done. These multilayer nanoshells with many interesting properties can be a potential candidate in the search of a new class of multifunctional nanodevice for advanced biomedical applications such as theranostic nanomedicines.

Scheme 3.3 shows the summary of all syntheses presented in this chapter. All prepared NPs were characterized by various techniques including TEM, SEM, UV-Vis-NIR spectroscopy, SQUID/VSM and Zeta Potential.

3.2 Experiments

3.2.1 Chemicals

All chemicals were purchased from standard suppliers and were used as received without further purification. Preparation of all solutions including buffer solutions, Au seed solution, $HAuCl_4$ plating solution are described in SI.

3.2.2 Synthesis of IONPs

Oleic acid coated IONPs were synthesized on a large scale as reported earlier [52], [75]. The obtained particles were dispersed in heptane and stored in a flask. Details can be found in the supporting information (SI).

3.2.3 Functionalization of IONPs

Dopamine functionalization of IONPs:

100 mg of oleic acid coated IONPs (50 mg/mL heptane) were dispersed in 50 mL of tetrahydrofuran (THF) in an Erlenmeyer flask. The solution was protected in argon atmosphere and then sonicated. To this solution, some amounts of aqueous 30 mg/mL dopamine hydrochloride solution (1.5 mL, 2 mL, 1.5 mL) were alternatively added in 2 hours. The solution was continuously sonicated for one hour. After one hour, the particles were magnetically separated and then dispersed again in water. This cycle was repeated three times and finally dopamine-HCl coated IONPs were dispersed in water (10 mg/mL) for storage.

The obtained solution has a very low pH value (pH~2) because of the present of HCl, which is not suitable for Au seed deposition later. The particles were collected and washed by centrifugation (11.000 rpm, 20 minutes, three times). Finally, the particles were dispersed in PBS buffer solution (10 mM, pH 6) at a concentration of 2 mg/mL in order to protonate $–NH_2$ groups.

mp-SiO_2 functionalization of IONPs

mp-SiO_2 coated IONPs were synthesized by the Stöber method following a published protocol with minor modifications [52], [181]. In a typical procedure, IONPs (12 mg) were dried from heptane solution and dissolved in 0.5 mL of chloroform. Simultaneously, 5 mL of 0.11 M aqueous CTAB solution was prepared at 35 ^{o}C and added to the chloroform solution. The mixture was stirred vigorously for 2 hours to form a turbid brown solution. Then, the mixture was heated up to 61.5 ^{o}C and kept stirring for 20 min to evaporate completely the chloroform, resulting in a transparent dark brown solution. After that, the solution was transferred to a 100 mL round flask

containing 45 mL of water and 0.3 mL of 2 M NaOH solution. The flask was connected to a condenser and heated up to 70 ^{o}C. To the solution, 0.5 mL of tetraethylorthosilicate (TEOS) and 3 mL of ethyl acetate were consequently added. The reaction completed after 3 hours. After removing ethyl acetate from the solution by rotary evaporation, the particles were separated by centrifugation and dispersed again in ethanol. This step was repeated several times to remove excess reactants. To extract CTAB from the silica shells, 40 µL of HCl 37 % was added to the dispersion and stirred at 60 ^{o}C for 3 hours or shaking overnight. The pH of the solution was tested by pH paper and should be around pH 1-2 to avoid dissolving the magnetic core [181]. Magnetic nanoparticles (MNPs) were separated and washed 3 times and then dispersed again in 20 mL at the concentration of 1 mg/mL.

Next, mp-SiO_2 shells were functionalized with (3-aminopropyl)trimethoxysilane (APTMS). In detail, mp-SiO_2 coated IONPs (12 mg) were collected from ethanol and dispersed in 20 mL of toluene. To this solution, 0.1 mL of APTMS was added and the obtained solution was shaken overnight. APTMS-functionalized IONPs were separated from toluene by centrifugation (11.000 rpm, 10 minutes, three times). The obtained particles were dispersed in ethanol (2 mg/mL).

To protonate –NH_2 groups, the particles were collected by centrifugation and dispersed in PBS buffer solution (10 mM, pH 6) at a concentration of 2 mg/mL.

3.2.4 Synthesis of Au nanoshells in aqueous phase

This section describes the general method of gold coating on the surface of dopamine or mp-SiO_2 functionalized IONPs. The method contains two steps: Au seed deposition on the surface of functionalized IONPs and Au shell growth. Preparation of Au seeds (ca. 2 nm) is described in SI.

Au seed deposition:

Prior to the Au seed deposition, amino-terminated functionalized IONPs were protonated, as described above, to strengthen their interaction with the Au seeds. Then, 1 mL of functionalized IONPs (2 mg/mL) was mixed with 6 mL of Au seed solution and the mixture was shaken for 18 hours. Au seed-decorated IONPs were separated by centrifugation (11.000 rpm, 20 minutes) and dispersed again in water. This cycle was repeated several times to remove excess Au seeds.

Au shell growth:

Au-coated IONPs were produced by the reduction of $AuCl_4^-$ ions (44 µM) in a plating solution by 10 µL of formaldehyde onto Au seed decorated IONPs [100]. The reaction took place in 15 minutes and the product was separated by centrifugation after the reaction (11.000 rpm, 20 minutes, 3 times). Au coated IONPs were dispersed again in water for the characterization (0.2 mg/mL).

3.2.5 Synthesis of Au nanoshells in an organic phase

Synthesis of Au nanoshells in an organic phase:

IOGNPs were synthesized in an organic phase following a previously reported protocol with some modifications [185]. In detail, 100 mg of oleic acid coated IONPs were dispersed in 5 mL of heptane. This solution was mixed with gold acetate (1mmol, 374mg), 1,2-hexadecanediol (3 mmol, 775mg), oleic acid (2 mmol, 505 µL), oleyl amine (2 mmol, 434 µL) and dioctyl ether (solvent, 20 mL). This mixture was heated to 180 ^{o}C and aged at that temperature for 30 minutes. After cooling down to room temperature, 150 mL of ethanol was added and the particles were separated magnetically. The supernatant is greenish at this point. A small amount of heptane (5 mL) was added, which results in a red phase. After adding 100 mL ethanol, the phase turns blue, indicating aggregation of gold-containing particles. The particles were magnetically attracted and the supernatant was decanted. This process was repeated five times. 100 µL of extra oleylamine was added to ensure the dispersion of Au-coated IONPs because these ligands might be washed away during purification. The nanoparticles were stored in heptane at a concentration of 10 mg/mL.

Phase transfer: CTAB was used as a capping agent to transfer IOGNPs from organic phase to aqueous phase. In detail, 12 mg IOGNPs were collected by evaporating heptane, then the particles were dispersed in 0.5 mL of chloroform. To this solution, 5 mL of aqueous 0.055 M CTAB was added and the mixture was vigorously stirred at 35 ^{o}C for 2 hours. Finally, the mixture was heated up to 61.5 ^{o}C and kept stirring for 20 min to evaporate completely the chloroform, resulting in a transparent dark pink solution.

3.2.6 Synthesis of IO-Au-SiO_2 NPs

Aqueous IOGNP solution was obtained by using CTAB as a ligand exchange agent as described in Section 3.2.5. 5 mL of aqueous IOGNP solution was added to a 100 mL round flask containing 45 mL of water and 0.3 mL of 2 M NaOH solution. The flask was connected to a condenser and heated up to 70 ^{o}C. To the solution, 0.5 mL of TEOS and 3 mL of ethyl acetate were subsequently added. The reaction was completed after 3 hours. After removing ethyl acetate from the solution by rotary evaporation, the particles were separated by centrifugation and dispersed again in ethanol. This step was repeated several times to remove excess reactants.

To extract CTAB from the silica shells, 20 µL of HCl 37 % was added to the dispersion and stirred at 60 ^{o}C for 3 hours or shaking for 16 hours. The pH should be around pH 1-2 to avoid dissolving the magnetic core [181]. After collection by centrifugation (7.000 rpm, 15 minutes), the particles were washed three times by ethanol and then dispersed again in 20 mL of ethanol.

IO-Au-SiO_2 NPs were functionalized with rhodamine B following a published protocol with minor modifications [52]. Firstly, rhodamine B isothiocyanate (RITC) was coupled to APTES before binding to *m*-SiO_2 shells. The mixture of RITC and APTES (molar ratio 1:10) in ethanol was shaken for 2 days under dark conditions. Next, IO-Au-SiO_2 NPs (12 mg) were dispersed in 20 mL of toluene. To this solution, 0.4 mL of RITC-APTES solution was added and the obtained solution was shaken overnight. Rhodamine B functionalized IO-Au-SiO_2 NPs were separated by centrifugation (11.000 rpm, 20 minutes). For the purification, the particles were dispersed in ethanol and then were collected by centrifugation (11.000 rpm, 20 minutes). This step was repeated several times until the supernatant was colorless and its absorbance in UV-Vis spectrum was insignificant.

3.2.7 Characterization

Nanoparticles were characterized using transmission electron microscopy (TEM, 80 kV Zeiss EM-900, 300 mesh Formvar on copper grids as substrate), scanning electron microscopy (SEM, XL30 FESEM FEG microscope), vibrating sample magnetometry (VSM, 300 K, Oxford instruments VSM Maglab), superconducting quantum interference device magnetometer (SQUID, Quantum Design MPMS XL-5), Zeta potential measurements (Zetasizer Nano from Malvern Instruments) and UV–visible absorbance measurements (Perkin- Elmer 900).

All TEM images were analyzed by Image J software.

3.3 Results and Discussion

3.3.1 Synthesis of IOGNPs in aqueous phase

Synthesis of Au seeds

Fig. 3.2 shows a TEM image of small Au NPs and the histogram of size distribution (inset). A size analysis indicates the size of Au seeds is 2.4 ± 0.5 nm. The UV-Vis spectrum of the Au seed solution is shown in Fig. 3.3 (solid line). The spectrum does not exhibit a plasmon peak as expected because the size of particles is too small. This result is consistent with results published previously [193]. According to Ref. [23], [196], Au NPs with a small size do not show a LSPR band whereas bigger Au NPs (e.g., 5 nm) show a pronounced plasmon peak. For example, commercial products containing 5 nm Au NPs from Sigma Aldrich and Cytodiagnostics show LSPR peaks at 510-520 nm [197], [198].

Synthesis of IOGNPs from dopamine functionalized IONPs

Superparamagnetic IONPs (mainly Fe_3O_4 with small amounts of Fe_2O_3) were synthesized as reported earlier [52], [75]. Fig. 3.3(a) shows a TEM image of oleic acid coated IONPs. The particles size is 8.6 ± 0.6 nm.

IONPs were transferred from the organic phase (heptane) to the aqueous phase upon dopamine functionalization. After the reaction, functionalized IONPs disperse well in water (10 mg/mL) and the solution is acidic due to the present of HCl. A quick pH test of the solution by a pH paper indicated the pH value was 2. Fig. 3.3(b) shows the TEM image of dopamine functionalized IONPs which is similar to that of oleic acid coated IONPs since the organic thin layer of dopamine does not appear in the TEM image.

Dopamine is attached strongly to the IONPs due to bidentate or bridge bidentate chelating interactions between iron ions on the surface and –OH groups of dopamine [199] (see Fig. 3.4). ZP measurement indicates a positive potential of +25.8 mV. This high ZP value also confirms the high stability of a colloidal dispersion of dopamine-functionalized IONPs in water [15].

Au seeds were deposited onto dopamine-functionalized IONPs under acidic conditions. The attachment is due to the electrostatics interaction between small Au NPs (negatively charged) and NH_3^+ groups of the coating layer [102], [174], as illustrated in Scheme 3.1. The attachment of Au seeds is confirmed by the ZP measurement of the particles after purification. Because synthesized Au seeds are negatively charged [182], [194], the ZP value of Au seed-decorated dopamine functionalized IONPs should change from positive (dopamine-IONPs +25.8 mV) to negative. Indeed, the negative ZP value of Au seed decorated NPs (-24.94 mV) is shown in Fig. 3.S2 (SI), proving the success of the attachment.

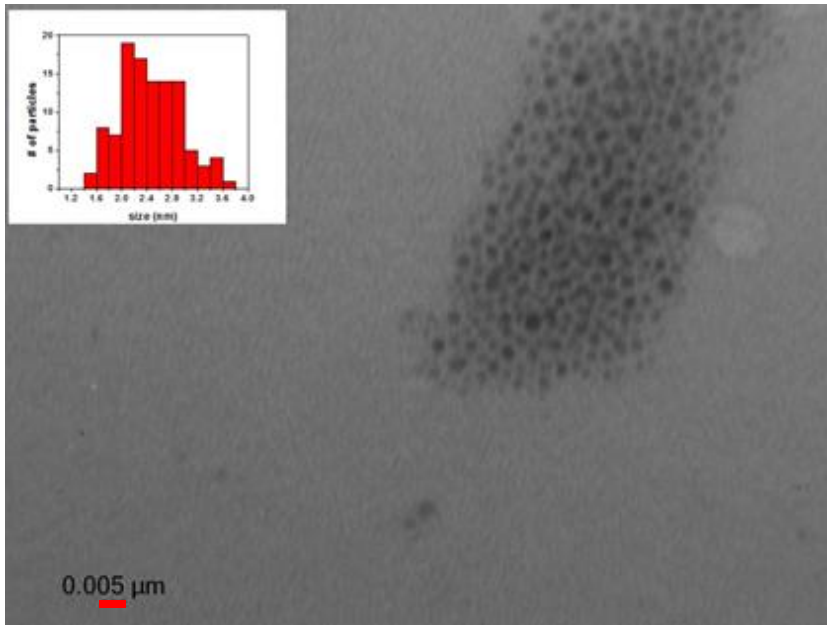

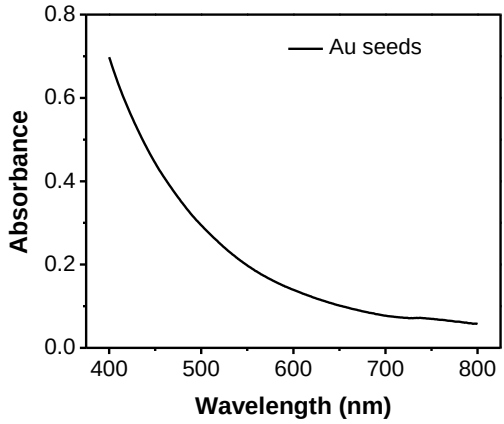

Fig. 3.2: (top) TEM image of Au seeds. The histograms of size distribution (inset) shows the Au seed size of 2.4 ± 0.5 nm. (Bottom) UV-Vis spectrum of Au seed solution. No LSPR peak is observed.

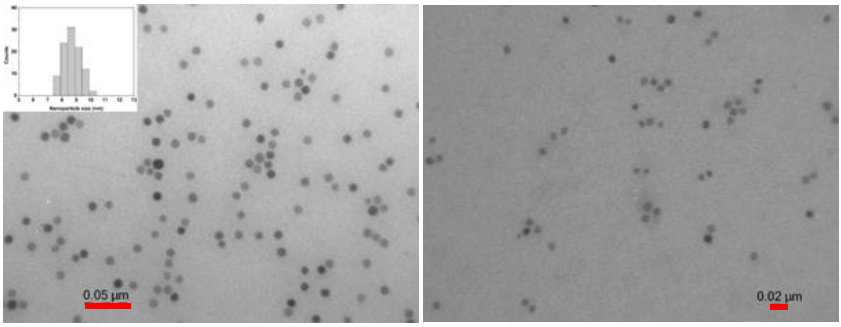

Fig. 3.3: TEM image of oleic acid coated IONPs (left, scale bar 50 nm) and dopamine functionalized IONPs (right, scale bar 20 nm). The inset shows the particle size of oleic acid-coated IONPs is 8.6 ± 0.6 nm.

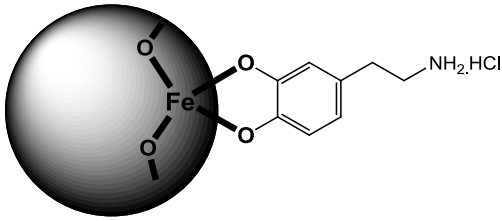

Fig. 3.4: The structure of dopamine coated IONPs

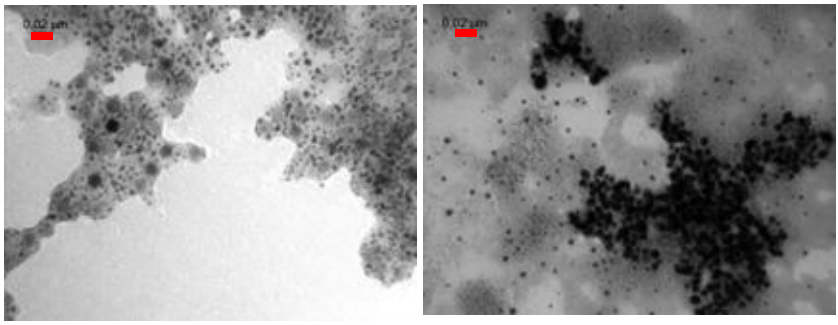

Fig. 3.5: TEM images of Au seeds-decorated iron oxide-dopamine NPs (pH=6) (left) and iron oxide/dopamine-Au core-shell NPs (right). Scale bars are 20 nm.

TEM images of Au seed-deposited on dopamine-coated IONPs are shown in Fig. 3.5(a). There are small Au NPs (1-3 nm) attached to IONPs, however there are also a lot of free Au seeds present. Furthermore, it seems as if the particles were embedded in a film of organic material. The Au seed-embedded film remained in the pellet after the centrifugation process, and then cannot be separated out of Au seed-deposited IONPs. Although this phenomenon was reproducible, it has not been understood fully. We hypothesize that the polymer film might be produced from the oxidative self-polymerization of dopamine [200]–[202].

For this reason, it is difficult to obtain well-defined IOGNPs after the Au shell growth process. Fig. 3.5(b) shows TEM images of core-shell NPs achieved when the $HAuCl_4$ precursor was reduced. There are some aggregations of Au nanoshells due to cross-linking between Au shells, but we can clearly see smaller islands and even isolated particles. Also, the sample after shell growth shows isolated Au NPs of ca 3-4 nm size which are assumed to result from the growth of Au on free Au seeds. Although these Au NPs can be removed by magnetic separation, the formation of aggregation is difficult to avoid due to the present of impurities of free Au seeds sticking in the polymer film.

Synthesis of IOGNPs from *mp*-SiO_2 functionalized IONPs

mp-SiO_2-coated IONPs were synthesized by the Stöber method in which TEOS was hydrolyzed by the reaction with NaOH and the silica shell was grown on top of the CTAB/oleic acid bilayer [52]. CTAB plays important roles in the synthesis of MNPs: i) it acts as phase transfer agent from the organic to the aqueous phase and ii) as template for the formation of pores during growth of the silica shell [181].

Fig. 3.6(a,b) shows TEM images of oleic acid coated IONPs (8.6 ± 0.6 nm) and *mp*-SiO_2 coated IONPs (ca. 50 nm). Pores inside the silica shell can be seen clearly in Fig. 3.6(c). After functionalization, the particles remain superparamagnetic however the saturation magnetization is significantly lower than that of oleic acid coated IONPs due to increased weight of the core/shell particles (Fig. 3.S3, SI). After functionalization of IONPs with a mp-SiO_2 shell and then with APTMS, Au seeds were decorated on the surface of particles and Au shell growth was carried out by the reduction of Au plating solution as illustrated in Scheme 3.4.

TEM image of Au seed decorated *mp*-SiO_2-functionalized IONPs is shown in Fig. 3.6(c). Each iron oxide - *mp*-SiO_2 core-shell particle is surrounded by a large number of Au seeds due to the large surface of the silica shell. The surface coverage of Au seeds is roughly estimated about 30%, which is consistent with results reported previously [194], [203]. A minus ZP value of iron oxide-silica-Au_{seed} (-22 mV, see Fig. 3.S4, SI), also confirms the formation of Au seed attachment.

By the addition of the Au plating solution and the reductant formaldehyde, $HAuCl_4$ was reduced on the Au seeds. As a result, the growth of Au seeds gradually leads to

Scheme 3.4: An illustration of the synthesis of iron oxide-mesoporous silica-gold multilayer nanoshells.

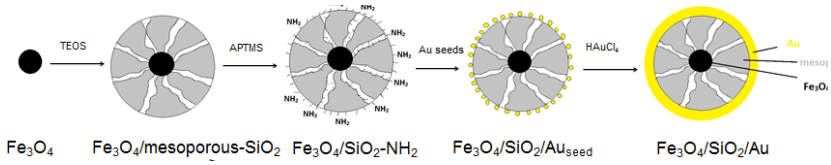

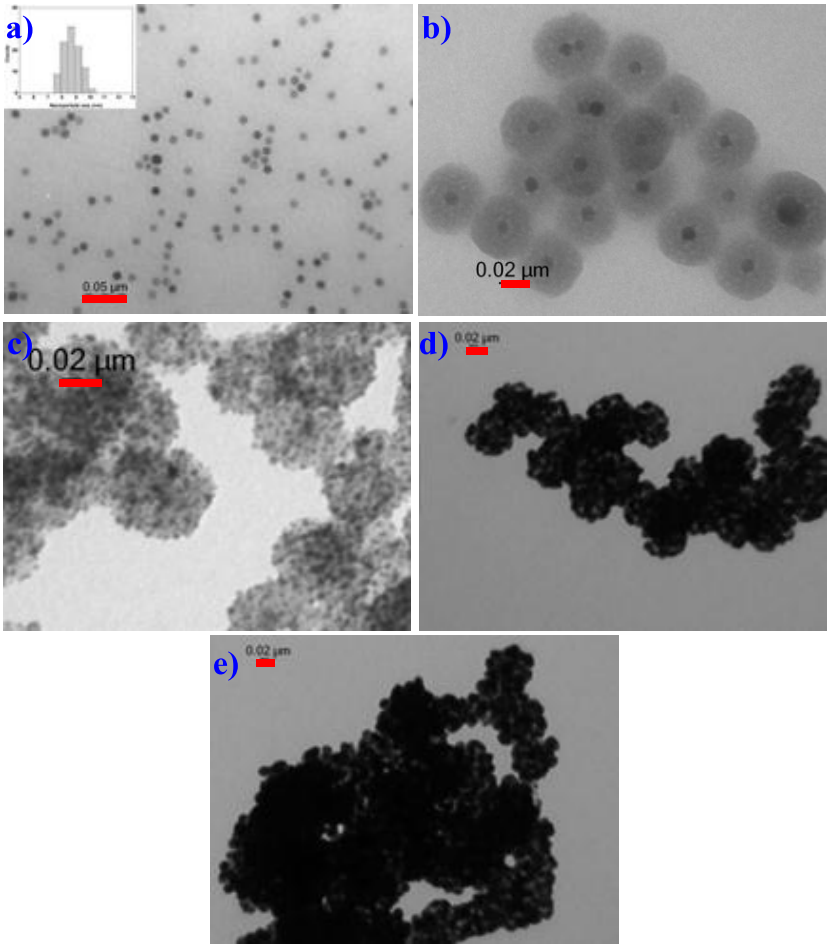

Fig. 3.6: TEM images of (a) oleic acid coated IONPs, (b) *mp*-SiO_2 functionalized IONPs, (c) Au seed-decorated *mp*-SiO_2 functionalized IONPs, (d,e) iron oxide-mesoporous silica-gold multilayer nanoshells. Scale bar in (a) is 50 nm. All scale bars in (b),(c), (d),(e) are 20 nm.

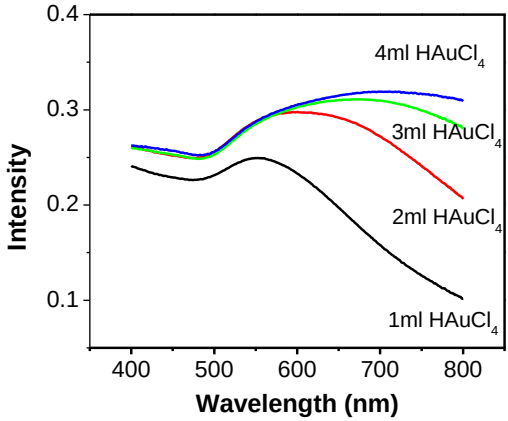

Fig. 3.7: UV-Vis spectra of Au nanoshells when adding 1-4 mL of Au plating solution to Au seed-decorated iron oxide-silica NPs.

the formation of incomplete Au shells and then complete Au shells. Formation of the incomplete Au shells are observed in the TEM image (Fig. 3.6d) and also in the SEM image (see Fig. 3.S5, SI). Furthermore, Fig. 3.6(e) shows TEM images of Au nanoshells when more Au plating solution added. We now clearly observe the formation of cross-linking between particles along with the growth of Au shells. This leads to the formation of aggregates and changes the optical properties of the Au nanoshells.

Fig. 3.7 shows UV-Vis spectra of iron oxide-silica-Au_{seed} NPs when gradually adding Au plating solution. Their intensity increases because more Au atoms were deposited on the surface of the particles, more free electrons on the surface of Au shells participate in the LSPR. Moreover, the SP band became broader and the band was red-shifted (up to ~ 700 nm). The continuous increase of λ_{max} when adding Au plating solution suggests that complete nanoshells have not been achieved yet because the SP band will be blue shifted when complete Au shells grow thicker [204], [205].

In general, IO-Au core-shell NPs were synthesized in aqueous phase with tunable plasmonic properties. The gold nanoshells were observed by TEM images while their LSPR bands can be red-shifted in NIR region. The core-shell NPs were synthesized from amino-terminated functionalized IONPs, in which Au shell growth plays a key role in the achievement of the well-defined IO-Au core-shell NPs. Although the results are promising, improvement of control of Au shell growth process is needed because cross-linking between Au shells was formed as side products, leading to the formation of aggregations.

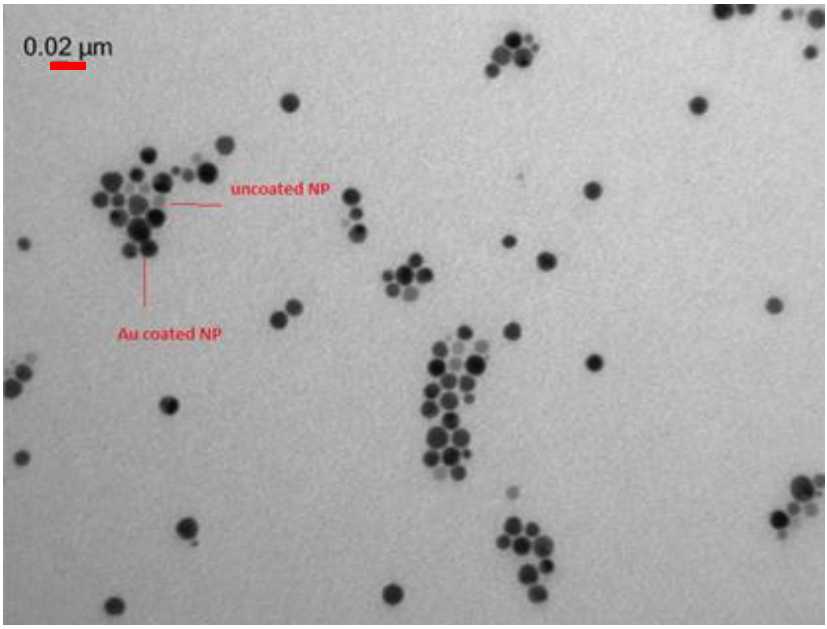

Fig. 3.8: TEM images of Au coated IONPs. An example of coated and uncoated NPs is pointed out. The coated and uncoated NPs can be distinguished by the contrast of the particles. Scale bar is 20 nm.

3.3.2 Synthesis of IOGNPs in organic phase

Synthesis of IOGNPs:

Oleic acid-coated IONPs were also used for the synthesis of IOGNPs in organic phase. The TEM image of IONPs was shown in Fig. 3.6a with a size of 8.6 ± 0.6 nm. Fig. 3.8 shows the TEM image of an iron oxide-gold core-shell NPs which appear much darker than the IONPs due to the formation of Au shells. An image analysis shows an overall size of around 10.9 ± 0.9 nm, yielding a thickness of the gold shell of 1.2 nm. There are a few brighter and smaller nanoparticles in Fig. 3.8, which can be assigned to uncoated nanoparticles. Actually, the core-shell structure cannot be seen in the TEM image because gold has a higher electron density than IONPs and allow fewer electrons to go through [206], [207]. However, the changes in the size and the appearance of particles in Fig. 3.8 indicates core-shell formation. Moreover, the study of their optical properties also strengthens this hypothesis.

Fig. 3.9 shows the extinction spectrum of Au-coated IONPs (solid line) in comparison with the spectrum of IONPs before the reaction (dashed line). The spectrum indicates a

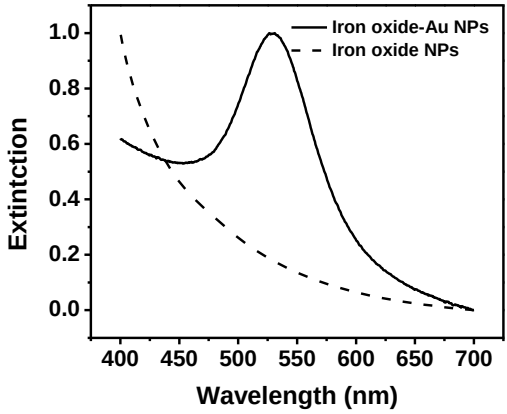

Fig. 3.9: Extinction spectra of IONPs and IO-Au core-shell NPs.

strong absorption peak centered at 528 nm due to the LSPR response of Au shells. The extinction of the gold-coated IONPs increases strongly at short wavelengths due to the scattering of nanoparticles.

The magnetic properties of the Au-coated IONPs were characterized by SQUID measurements. The measurements were performed in magnetic fields from -3 to 3 Tesla at 300 K. Fig. 3.10 shows the magnetization curve of core-shell NPs in comparison with the magnetization curve of IONPs performed by VSM measurement. The saturation magnetization decreases from 56 emu/g to 9.2 emu/g upon the gold coating. This decrease (84%) is very large if we only consider the decrease of magnetization due to the increase of magnetic particle weight (29% - calculated). Hence, the decrease is not only ascribable to the particle weight increase. There must be a contribution from the interaction between the magnetic core and the gold shell.

There are some reports indicating that direct coating of gold onto IONPs severely decreases the saturation magnetization of the magnetic core by 78% or more [23], [33]. The mechanism is still being studied however there might be a contribution from the migration of gold atoms into the iron oxide core, as suggested by Smolensky [33]. This migration would lead to a distortion of the core and therefore decrease of the magnetic properties. A similar effect was also discovered when gold was coated on the surface of cobalt NPs [208].

Phase transfer

Au-coated IONPs were transferred from an organic phase (heptane) to an aqueous phase by the interaction of CTAB with the coating layer of oleic acid and oleylamine.

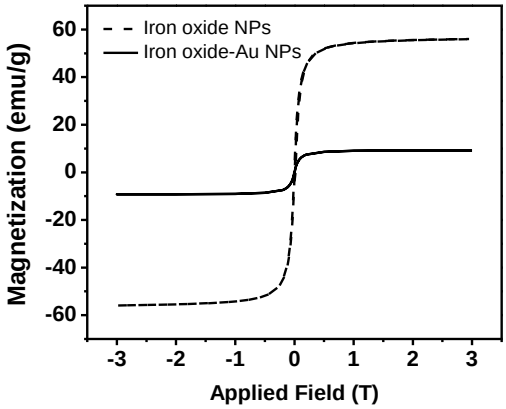

Fig. 3.10: Comparison of saturation magnetization of iron oxide NPs (VSM measurement, dashed line) and saturation magnetization of gold coated iron oxide NPs (SQUID measurement, solid line).

Fig. 3.11: Dispersion of Au coated IONPs in heptane (left) and in water (right) before and after phase transfer.

Because oleic acid binds more strongly to IONPs than CTAB does, no ligand exchange occurs. There is formation of oleic acid/oleylamine – CTAB bilayers in which hydrocarbon tails of CTAB penetrate the hydrocarbon chains of oleic acid/oleylamine and the ammonium heads become exposed to the aqueous medium. Fig. 3.11 shows the dispersion of Au-coated IONPs in heptane (left) and in water

(right) before and after phase transfer. The organic phase turned colorless after phase transfer indicating all Au-coated IONPs were successfully transferred to aqueous phase.

After many efforts, well-defined water-dispersed iron oxide-gold core-shell NPs were achieved. The particles are spherical, containing a magnetic core with a small standard deviation and a thin shell of gold. These core-shell particles can be further modified/functionalized and applied in many applications.

3.3.3 Synthesis of IO-Au-SiO_2 NPs

Iron oxide-gold-mesoporous silica multilayer nanoshells were synthesized from Au-coated IONPs. The procedure consists of two steps: phase transfer of IOGNPs from organic phase to water and mesoporous silica growth by Stöber method. Fig. 3.12 shows TEM images of IO-Au-SiNPs. An analysis indicates the particle size is 67.4 ± 7.2 nm. Taking into account that the size of IONPs is 8.6 nm and the size of IOGNPs is 10.9 nm, the inner shell thickness of gold shell is 1.2 nm and the outer shell thickness of silica is 28.1 nm.

The addition of mesoporous silica shells onto the IOGNP surface leads to mesoporous shells which might be exploited in drug release and delivery, fluorescent labeling, so on. These extra potential applications rely on porous silica shells and their ability in functionalization with various ligands. For these reasons, IO-Au-SiO_2 NPs were functionalized with rhodamine B as a test. Fig. 3.13 shows the UV-Vis spectra of IO-Au-SiO_2 NPs (dashed line) and rhodamine B functionalized IO-Au-SiNPs (solid line). The spectrum of IO-Au-SiO_2 NPs exhibits a LSPR peak centered at 528 nm, indicating that the coating layer of silica does not change the optical properties of the gold shell. After functionalization, bound rhodamine B shows a strong absorption at 550nm and the LSPR band of Au shells still remains in the spectrum as a shoulder.

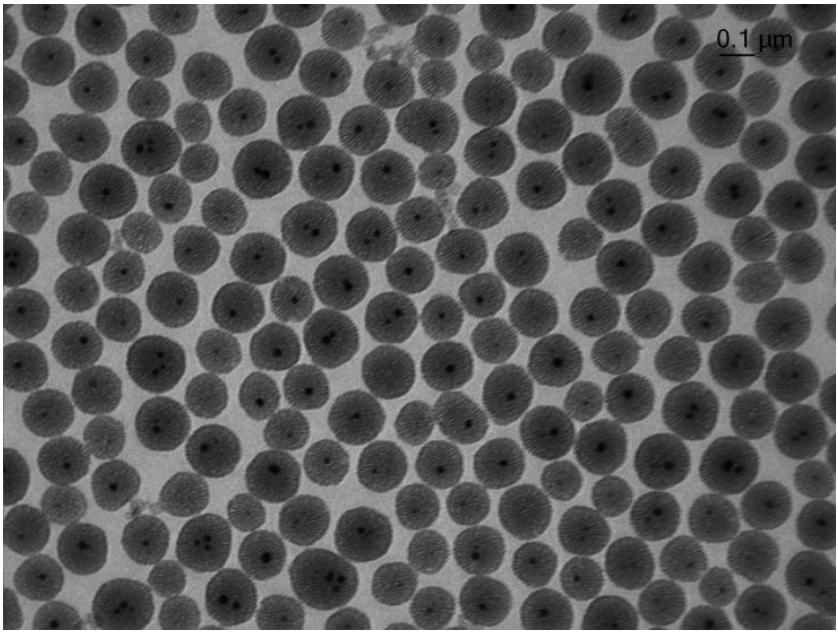

Fig. 3.12: TEM images of IO-Au-SiO_2 NPs.

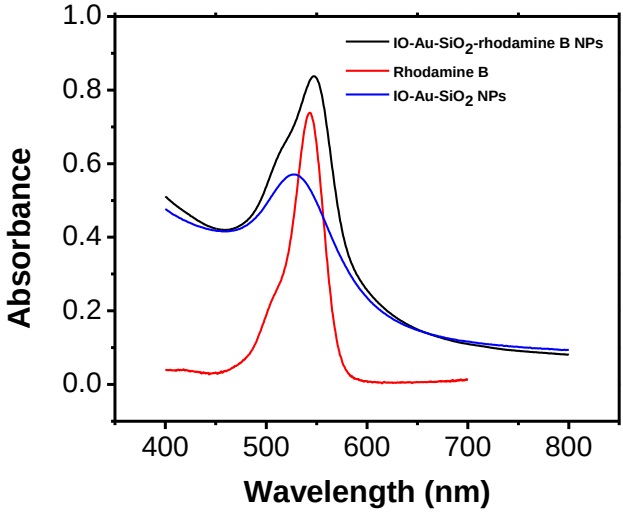

Fig. 3.13: UV-Vis spectra of IO-Au-SiO_2 NPs , free rhodamine B and rhodamine B functionalized IO-Au-SiO_2 NPs.

3.4 Conclusions

In summary, we have described two approaches to synthesize iron oxide-gold core-shell NPs: synthesis in aqueous phase and organic phase. A large batch of highly monodispersed oleic acid-coated IONPs (8.6 nm size) was synthesized and these particles were used as seeds for all gold coating experiments in this study.

Synthesis in the aqueous phase started with Au seed deposition onto the surface of amino-terminated functionalized IONPs. Then $HAuCl_4$ was selectively reduced onto Au seeds by a weak reductant, leading to the formation of Au shells. Moreover, their plasmonic properties are tunable and can be shifted in NIR region. However, further studies on Au shells growth control need to be performed in order to achieve monodispersed core-shell structures.

Synthesis in the organic phase resulted in well-defined gold coated IONPs with the shell thickness of 1.2 nm. Then, the particles could be transferred from organic phase into aqueous phase for biomedical applications. Their plasmonic properties remain unchanged but the magnetization of the core-shell structures was intensively decreased, mainly due to the immigration of Au atoms into iron oxide core. Furthermore, multilayer nanoshells were also synthesized in order to combine all novel properties of the magnetic core, the plasmonic shell and the mesoporous silica shell.

With many interesting properties, magneto-plasmonic core-shell nanoparticles are promising candidates for advanced biomedical applications such as noninvasive imaging, magnetically guided drug delivery, controlled drug release, targeted hyperthermia induced by an external magnetic field or a laser source. Plasmonic properties are also interesting for nonlinear imaging and labeling applications.

3.5 Supporting information

A. Experimental section

All chemicals were purchased from standard suppliers and used as received without further purification. Milli-Q H_2O (18 MΩ cm^{-1}) was used to prepare all aqueous solutions.

In detail: tetrakis(hydroxymethyl)phosphonium chloride (THPC, 80 % solution in H_2O) formaldehyde (HCHO, 37 % in water), Cetyltrimethylammonium bromide (CTAB), tetraethylorthosilicate (TEOS), Dopamine hydrochloride (Dop.HCl), sodium oleate and iron(III) chloride hexahydrate (97 %) were purchased from Sigma Aldrich. Tetrahydrofuran (THF), tetrachloroauric acid ($HAuCl_4.3H_2O$), hydrogen chloride (HCl, 37 %), sodium hydroxide (NaOH, pellet), sodium dihydrogen phosphate (NaH_2PO_4), potassium carbonate (K_2CO_3) were purchased from Sigma Aldrich.

3-Aminopropyltrimethoxysilane (APTMS, 97 %) were obtained from ABCR. 1-Octadecene (90 %, technical grade) was purchased at Acros. Ethanol (EtOH, absolute) and oleic acid were obtained from VWR. Heptane and toluene were obtained from Fisher Scientific, and acetone was purchased at Chem Lab.

Preparation of Au seeds

Au seeds (ca. 2nm) were synthesized following a previously published protocol with minor modifications [193]. Firstly, the solution of $HAuCl_4$ was prepared beforehand by dissolving 20 mg of $HAuCl_4.3H_2O$ in 2mL Milli-Q water. This fresh solution need to be prepared at least 15 minutes before the reaction [193]. Then, a mixture of 45.5 mL of Milli-Q H_2O and 1.5 mL of 2M NaOH was prepared and vigorously stirred in a 100 mL beaker. To this solution, 1 mL of H_2O and 12 µL of 80% THPC was added. After 2 minutes, 2 mL of the $HAuCl_4$ solution was added, leading to the change of solution color from yellow to brown after few seconds due to the formation of brown hydrosol of gold. The solution was kept stirring in 10 minutes and then stored in a dark condition at 4 ^{o}C. A large quantity of gold sols (up to 300 mL) with similar size can be prepared by using the same procedure.

Preparation of PBS buffer solution

10 mM PBS buffer solutions were prepared from NaH_2PO_4. pH values of these solutions were determined by a pH meter and was adjusted by dilute HCl or NaOH solutions.

Preparation of $HAuCl_4$ plating solution

A 0.44 mM $HAuCl_4$ plating solution was prepared from Au precursor ($HAuCl_4$) by dissolving 30 mg of $HAuCl_4$ (34.8 mg $HAuCl_4.3H_2O$) and 50 mg of K_2CO_3 in 200.3 mL of Milli-Q H_2O. The plating solution was stored at 4 ^oC for at least 1 day before use as recommended by Bruce [100].

Preparation Au NPs by citrate method

Gold colloidal synthesis was performed following a method based on an aqueous citrate reduction [209]. In a typical protocol, 500 mL of 1 mM $HAuCl_4$ was prepared in a 1 L Erlenmeyer flask. The solution was vigorous stirred and heated to boil. When the solution boiled, 50 mL of 38.8 mM sodium citrate was added. The yellow solution shortly turned clear, dark blue and then a deep red burgundy color. After that, the solution was kept stirring and boiling for 10–15 min. Heat source was removed and the solution was then kept stirring for 15 min. Finally, the solution was diluted to 500 mL with H_2O, resulting a deep red colored dispersion.

Synthesis of oleic acid coated IONPs

Superparamagnetic IONPs were synthesized by the method published previously [75], [210]. First iron oleate precursor were prepared from iron (III) chloride and sodium oleate, followed by the transformation into IONPs.

36.5 g (120 mmol) of sodium oleate and 10.8 g (40 mmol) of $FeCl_3.6H_2O$ were dissolved in a mixture of 80 mL ethanol, 60 mL Milli-Q water, and 140 mL heptane. This mixture was heated to reflux at 70 ^oC for 4 h under argon protection. Afterward, the upper layer containing iron oleate in heptane, was separated using a separatory funnel and washed three times with 40 mL Milli-Q water. Then, heptane was evaporated using a rotavapor, resulting in a dark brown waxy solid.

For the synthesis of IONPs, 36 g (40 mmol) of iron oleate precursor, 5.7 g (20 mmol) of oleic acid and 200 g of 1-octadecene were added to a 500 mL three-neck flask. This mixture was first heated to 100 ^oC for 5 min to evaporate all remaining heptane. After fitting a reflux cooler, the mixture was heated further to 320 ^oC and kept at that temperature for 30 min. Around 250 ^oC, the decarboxylation of the oleate starts, producing a large amount of CO_2 gas. After the reaction, the mixture was cooled down to room temperature. The precipitation of IONPs was performed by the addition of the large amount of ethanol (500 mL). After that, the particles were magnetically separated and washed with ethanol. Finally, IONPs were dried in a vacuum and then dispersed in heptane (with one drop of oleic acid) at the concentration of 100 mg/mL.

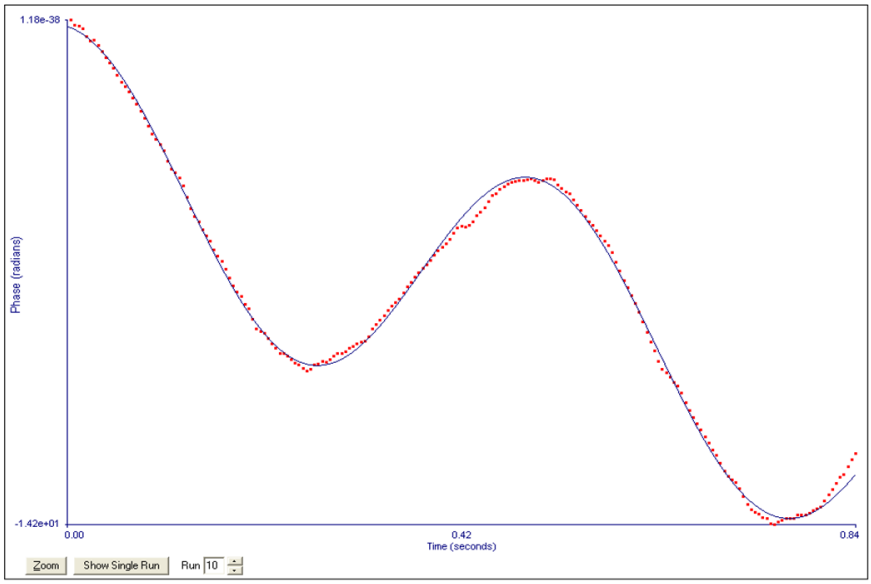

Run	Mobility	Zeta Potential (mV)	Rel. Residual
1	-2.15	-27.50	0.0299
2	-1.91	-24.47	0.0283
3	-1.86	-23.84	0.1020
4	-1.82	-23.30	0.0389
5	-1.77	-22.68	0.0443
6	-1.78	-22.74	0.0373
7	-1.65	-21.17	0.0505
8	-1.94	-24.87	0.0336
9	-2.00	-25.64	0.0248
10	-1.96	-25.05	0.0380
Mean	-1.96	-25.14	0.0322
Std. Error	0.04	0.57	0.0023
Combined	-1.95	-24.94	0.0111

Fig. 3.S2: ZP measurement of Au seed-decorated dopamine functionalized IONPs.

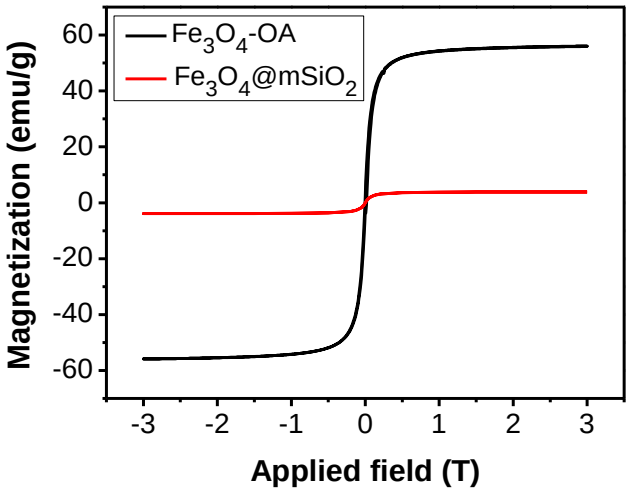

Fig. 3.S3. Magnetization curves of IONPs and mesoporous silica coated IONPs. After the synthesis, the particles retain superparamagnetic behavior. Reprinted from our published article, Ref. [52].

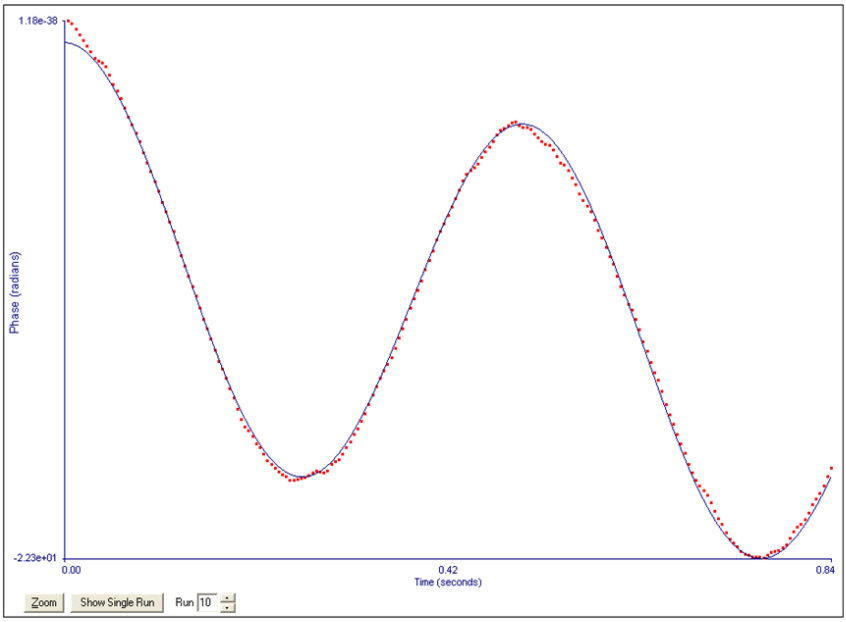

Run	Mobility	Zeta Potential (mV)	Rel. Residual
1	-1.80	-23.01	0.0301
2	-1.79	-22.97	0.0445
3	-1.66	-21.28	0.0306
4	-1.87	-23.93	0.0252
5	-1.77	-22.66	0.0799
6	-1.62	-20.78	0.0661
7	-1.77	-22.59	0.0452
8	-1.88	-24.01	0.0860
9	-1.66	-21.25	0.0284
10	-1.69	-21.64	0.0438
Mean	-1.73	-22.20	0.0375
Std. Error	0.04	0.52	0.0063
Combined	-1.73	-22.17	0.0159

Fig. 3.S4: Zeta potential measurement of iron oxide-silica-Au_{seed} NPs.

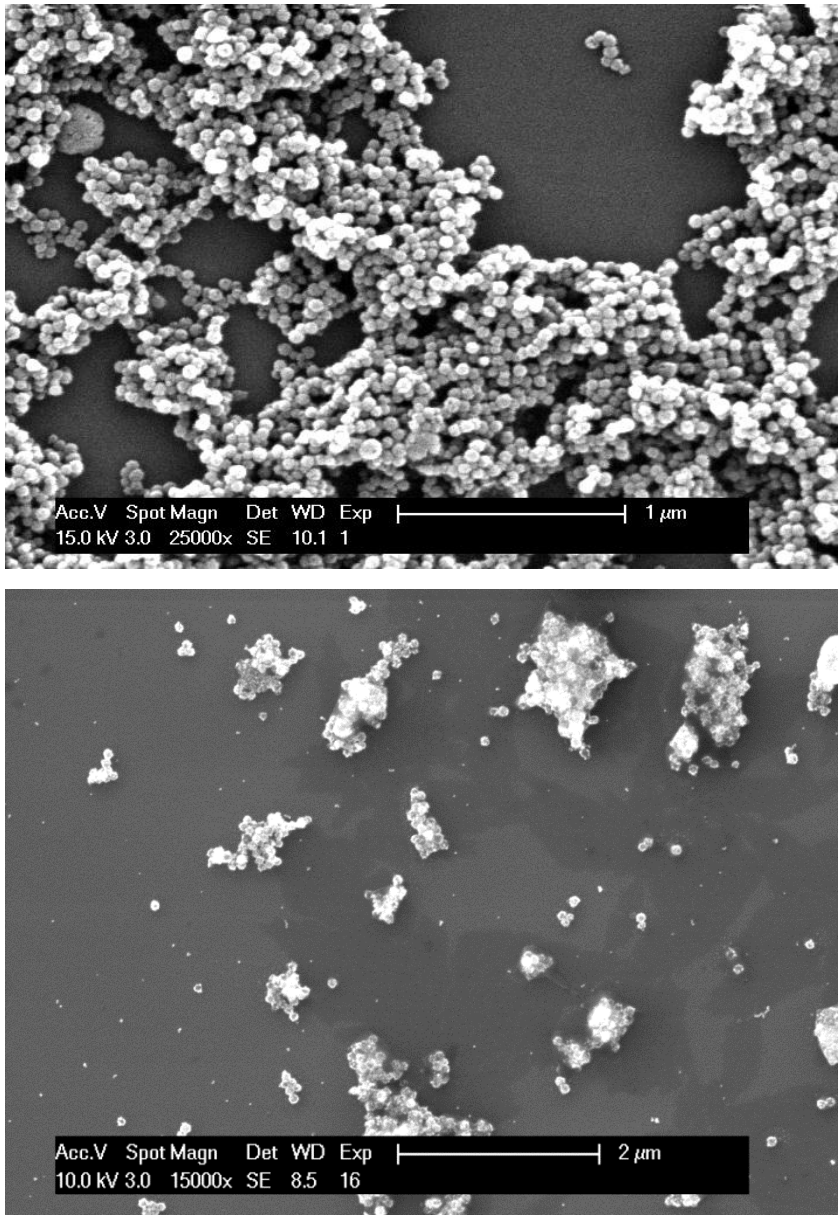

Fig. 3.S5: SEM images of Au seed decorated iron oxide-silica core-shell NPs (top) and incomplete Au shells (bottom).

Chapter 4

Magnetothermal release of payload from iron oxide/silica drug delivery agents

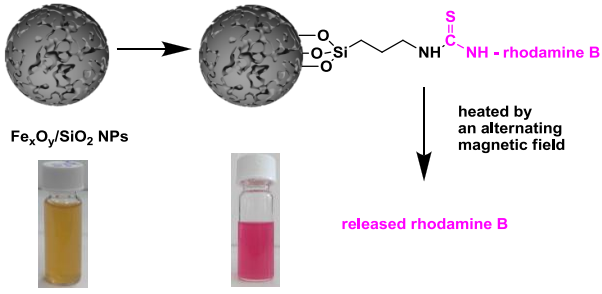

This chapter is based on the following publication with minor modifications: "Magnetothermal Release of Payload from Iron Oxide/Silica Drug Delivery Agents"
T. T. Luong, S.Knoppe, M. Bloemen, W. Brullot, R. Strobbe, J.-P.Locquet and T. Verbiest.
Journal of Magnetism and Magnetic Materials, 416 (2016) 194-199

Dr. M. Bloemen prepared iron oxide nanoparticles. R. Strobbe designed the AC magnetic heating setup. J. Jochum performed SQUID measurements. Prof. Dr. J. Billen performed TEM measurements.

Abstract

The release of covalently bound Rhodamine B from iron oxide/mesoporous silica core/shell nanoparticles under magnetically induced heating was studied. The system acts as a model to study drug delivery and payload release under magnetothermal heating.

4.1 Introduction

Magnetic nanoparticles are of great interest for researchers from a broad range of disciplines, especially in bio-medicine, because of their interesting properties such as superparamagnetism, non-toxicity, bio-compatibility, and ability to functionalise the ligand shell [63], [151], [211], [212]. Some important bio-applications are magnetic bio-separation and detection of biological entities [67], [211] (such as cells, proteins, nucleic acids, enzymes, bacteria, and viruses), clinic diagnosis and therapy (including Magnetic Resonance Imaging, MRI, and magnetic hyperthermia) [67], [170], [213]–[215].

Among these applications, inducing hyperthermia with magnetic nanoparticles is a promising one [216]. Under the influence of external oscillating magnetic fields, magnetic nanoparticles can be heated through several loss process such as Néel relaxation or Brownian relaxation. This leads to temperature increase of the surrounding medium and subsequent death of cancer cells. Cell death can occur when the temperature of the region increases above 42 ^{o}C while necrosis occurs at 50 ^{o}C and above [13]. In order to obtain hyperthermia efficiency, magnetic nanoparticles need to be targeted and gathered with high enough concentration on the surface of the cancer tumor, and efficient targeting is still challenging [217].

Recently, controlled dye/drug release has been the focus of many studies [43], [164], [218]–[220]. Multifunctional drug delivery systems, especially mesoporous nanoshell structures, have received a lot of attention because many interesting properties can be combined into one particle [164], [221]. In addition, mesoporous silica nanoshells or nanoparticles are known to be nontoxic [41], [222]. Silica nanoparticles with uniform shape and size, and well-defined mesoporous structure were synthesized [223] and they can carry dyes or drugs [57], [224], [225]. It is essential for these systems to exhibit a “zero release” of payload (under normal conditions) and efficient release under external stimuli [220]. To meet the “zero release” requirement, the pores on the surface of silica shells are covered by macro cycles [164], polymers [218] or small nanoparticles [43], [219] after loading the cargo molecules. Opening of these nanocaps can be triggered by chemical and physical stimuli such as pH,

Scheme 4.1: Schematic for the preparation of Rho-MNPs.

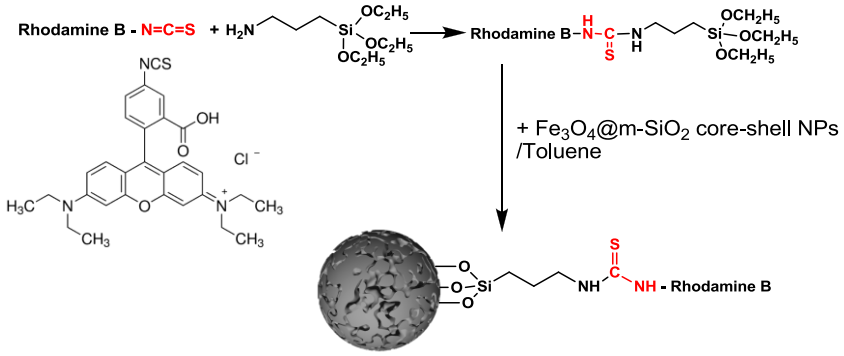

disulfide reducing compounds, enzymes, temperature, light, magnetic field [220]. The physical stimuli-induced release cannot only be controlled spatially and temporally but also has the advantage of avoiding a physical contact or chemical reaction with the carrier devices. Although the payload molecules are trapped inside mesoporous silica shells and their release is prevented considerably by forming nanocaps, it is still a challenge to fully control premature payload leakage and stability under physiological conditions.

In this context, we report the loading of a payload (rhodamine B fluorescent dye [181], [226], [227]) by forming a robust covalent bond with iron oxide-mesoporous core-shell nanoparticles (Scheme 4.1). We studied release of the dye via magnetically induced heating. We studied the influence of magnetic field strength on the extent of dye release. The release was followed photometrically, and the rhodamine B acts as a model for controlled magnetically induced dye release from magnetic core/shell nanoparticles.

4.2 Experimental section

The synthesis of rhodamine B functionalized iron oxide/mesoporous silica core/shell nanoparticles (Rho-MNPs) was carried out following published protocols with modifications [75], [181]. Details can be found in the SI.

A home-made AC magnetic heating setup with a copper coil (n = 42 loops, l = 0.42 m) was used (Fig. 4.S1, SI). The coil was connected to an AC power source, and the amplitude of the magnetic field is determined by equation (1) in SI. Release of dye was studied at different magnetic field strengths: 2.4 kA/m,

3.6 kA/m, 4.8 kA/m and 6 kA/m (magnetic flux density: 30 G, 45 G, 60 G and 75 G, respectively) at a frequency of 48 kHz. A centrifugation tube containing 7.5 mL of Rho-MNPs solution (0.133 mg/mL) was placed in the center of the copper coil (Fig. 4.S1, SI). For each magnetic field, the temperature of the bulk solution was recorded until equilibration.

To determine the amount of released dye, aliquots of 0.5 mL were taken over a range of up to ten days and diluted three times with ethanol. The solution was centrifuged (11,000 rpm, 20 min) and the supernatant was collected and its UV-Vis spectrum was recorded. To prove that the dye release is induced by magnetic heating and not due to temperature increase in the bulk solution, control experiments were carried out. In detail, Rho-MNPs were aged at different temperature using an oil bath instead of an AC magnetic field as a heat source. Otherwise, the samples were processed as described above.

4.3 Results and Discussion

Superparamagnetic iron oxide nanoparticles (IONPs) (mainly Fe_3O_4 with small amounts of Fe_2O_3) were synthesized at large scale as reported earlier [75]. Fig. 4.S2 in SI shows a TEM image of oleic acid coated IONPs and the histogram of particle size distribution (the inset). The particles size is 8.6 ± 0.6 nm. CTAB plays important roles in the synthesis of magnetic nanoparticles (MNPs): i) it acts as phase transfer agent from the organic to the aqueous phase and ii) as template for the formation of pores during growth of the silica shell [181]. To form the shells, TEOS was hydrolyzed by the reaction with NaOH and the silica shell was grown from ammonium groups of CTAB-IONPs.

Fig. 4.S3 (SI) shows TEM images of MNPs when changing the concentration from 0.275 M to 0.0275 M. In most cases, one iron oxide core was coated by a silica shell. Visually, the pore size decreases when the amount of CTAB is decreased (Fig. 4.S3a,b,c,d). An analysis of particle size indicates that the size of the core-shell nanoparticle is around 50 nm, yielding a thickness of the silica shell of ca. 20.7 nm. A CTAB concentration of 0.11 M was used for the particles in further experiments.

Characterization of MNPs by a superconducting quantum interference device (SQUID) shows that no coercivity or magnetic remanence is found, indicating that the particles remain superparamagnetic (Fig. 4.S4). The magnetization of the core/shell particles saturates at ca. 1 Tesla. The saturation magnetization (3.86 emu/g) of the core/shell particles is significantly lower than that of oleic acid coated IONPs (55 emu/g) [75]. This decrease is assumed to be due to increased weight of the core/shell particles. The particles were then

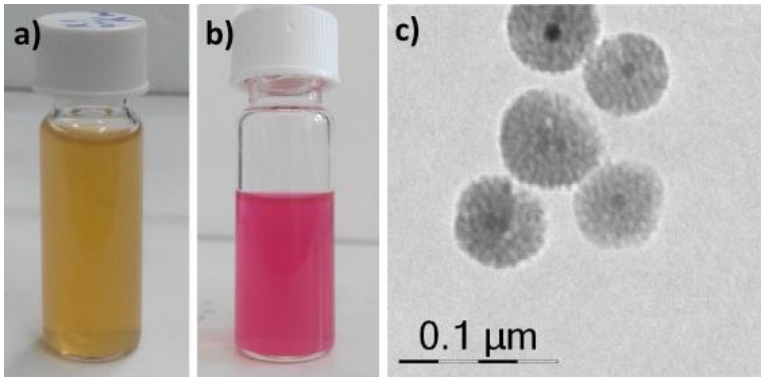

Fig. 4.1: Photographs of MNPs solution before (a) and after (b) loading with rhodamine B, the solvent is ethanol. c) TEM image of MNPs (a).

functionalized with rhodamine B isothiocyanate (RITC). For this, we first reacted RITC with APTES in ethanol as shown in Scheme 1, followed by addition of RITC-APTES to a dispersion of the MNPs in toluene. Toluene contains enough water to initiate the condensation reaction between the siloxane and the silica shell [228]. A photograph of the RITC functionalized MNPs is shown in Fig. 4.1.

When applying an external AC magnetic field to Rho-MNPs, the magnetic particles convert magnetic energy to thermal energy and the MSNs are heated strongly. Fig. 4.S5a shows the temperature increase of the bulk solution as the result of increase of the local temperature surrounding the magnetic particles. The starting temperature is 22 ^{o}C and it reaches saturation after one hour in most cases. When the amplitude of the applied magnetic field was varied from 2.4 kA/m to 6 kA/m, the temperature increase of the solutions (ΔT) increased from 3 to 17.5 ^{o}C. The temperature evolution in the bulk solution follows an exponential function [229] (Table 4.S1, SI). A linear correlation was found when comparing the temperature increase ΔT as a function of the magnetic field H (Fig. 4.S5b, SI). Although the concentration of MNPs was quite low (0.133 mg/mL), a significant increase of the solution temperature is observed, suggesting that the local temperature surrounding the MNPs is very high and this thermal energy might be high enough to break down the covalent bonding in mesoporous silica shells to release the payload. The average bond dissociation enthalpies of C-N, C-Si, C-C are 305, 318, 347 (kJ/mol) respectively [230], suggesting that the C-N bond in the thiourea group might be broken to release rhodamine B.

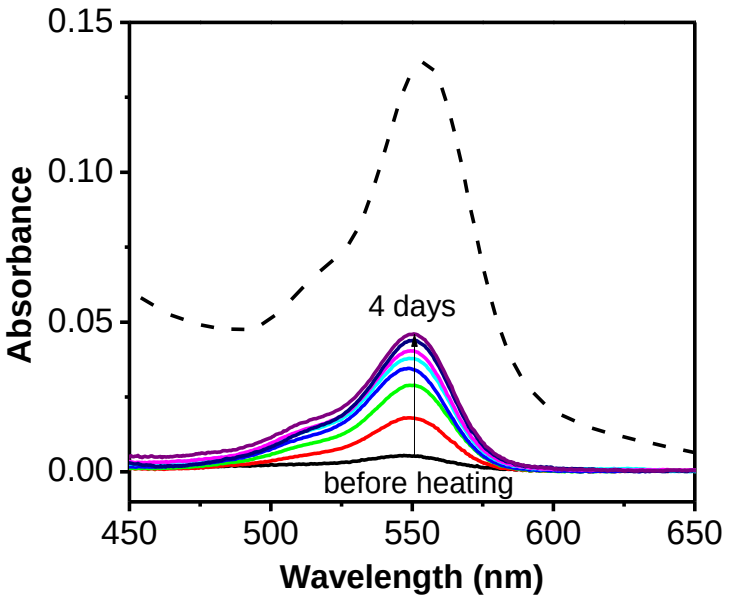

Fig. 4.2: Extinction spectra of Rho-MNPs solution (dash line) and released rhodamine in the supernatant (solid line) after magnetic heating over four days (magnetic field: 6 kA/m).

When the particles are heated by AC magnetic fields, rhodamine B is released from the MNPs, hence the absorbance of rhodamine B in the supernatant increases. Fig. 4.2 shows the UV-Vis spectra of the supernatants before and after heating (H = 6 kA/m) over a time span of four days.

The concentration of the released dye is straight forwardly calculated from the absorbance of the supernatants (Figs. 4.S6 and 4.S7). The determination of the concentration of the dye in the nanoparticles is more complex due to scattering contributions from iron oxide and silica. We used Gaussian peak fitting of the extinction spectra of Rho-MNPs in ethanol to extract the contribution of dye absorption (Fig. 4.S8).

Fig. 4.3 shows the percentage of released dye (with respect to the total amount of dye in the nanoparticles). The dye is released faster when exposed to stronger magnetic fields. At 6 kA/m, the dye release appears to saturate at about 40 % after four days, but slightly drops after continued magnetic heating. This decrease is reproducible and might be due to degradation of the dye by high local temperatures surrounding the MNPs (see Fig. 4.S11). At lower magnetic

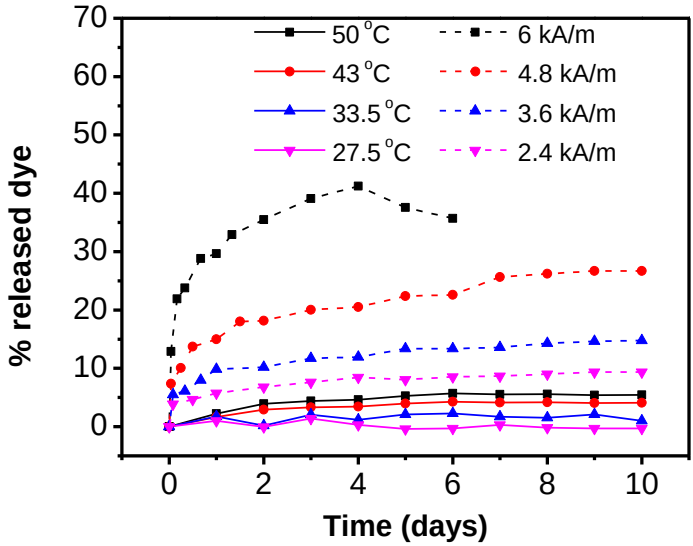

Fig. 4.3: Percentage of released dye in different magnetic heating experiments and control experiments (without magnetic field). More dye was released when increasing the strength of the magnetic field from 2.4 - 6 kA/m (dotted lines). In the control experiments (solid lines), even at elevated temperatures, the amount of released dye is significantly lower than with magnetically induced heating at low fields. Note that the lines are merely a guide to the eye and not a fit to the data.

field strengths, less dye is released. The fact that we do not observe complete release is likely due to two reasons: 1) at stronger fields the dye might degrade before complete release; 2) the silica shell is not completely degraded as seen in transmission electron microscopy (Fig. 4.4). Future research could therefore focus on improving release by changing the strength of the covalent bond (300 – 350 kJ/mol for thiourea), the thickness and porosity of the silica shell and the magnetic field strength. While this may be detrimental to the stability of the payload (see above), we suggest pulsed magnetic field induced heating instead of continuous heating. In addition, the dye release may depend on the pH, as it is known that the dissolution of mesoporous silica is faster in basic media [231]. Hence, under physiological conditions (pH ~ 7.5), dye release could be significantly different.

Note that a strong magnetic field was used in this experiment, causing a high solution temperature (39.5 ^{o}C). Therefore, control experiments using external

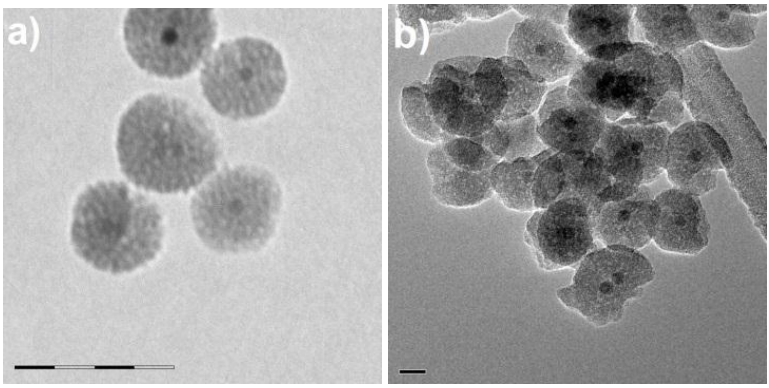

Fig. 4.4: TEM images of NPs before heating (a) and after heating at the magnetic field of 6 kA/m for 5 days (b). The scale bars are 100 nm (a) and 20 nm (b).

heating via an oil bath (solution temperatures of 27.5 – 50 °C) were carried out to show that the release is due to heating of the magnetic cores of the nanoparticles and not due to temperature increase of the bulk solution. Even at elevated temperatures, the absorbance of the supernatant is significantly lower than with magnetically induced heating at low fields (Fig. 4.3).

Using CTAB as templating agent during growth of the silica shell, mesoporous shells are obtained. These are known to degrade under heat [232]–[234]. Fig. 4.4 shows TEM images of MNPs before and after heating at 6 kA/m for six days. Clearly, the morphology of the MNPs was modified, caused by the heating of the magnetic core. The damage of the silica shells results in an increase of pore size.

The release of rhodamine B into the solution under magnetically induced heating is due to the local heating of the superparamagnetic iron oxide cores of the core/shell particles. The concentration of dye in the supernatant after equilibration scales linearly with the magnetic field strength applied during heating (Fig. 4.5, top) It is an obvious question to search for the reaction law and a correlation between magnetic field strength and the rate of dye release. In a simplified way, the dye release process can be described by the reaction:

$$Rho\text{-}MNPs \rightarrow Rhodamine$$

This unimolecular reaction might be expected to obey a first order rate law:

$$ln(C) = -kt + ln(C_0)$$

Where C is the concentration of the reactant (bound dye, mol/L), C_0 is the concentration of the reactant at the beginning and k is the rate constant.

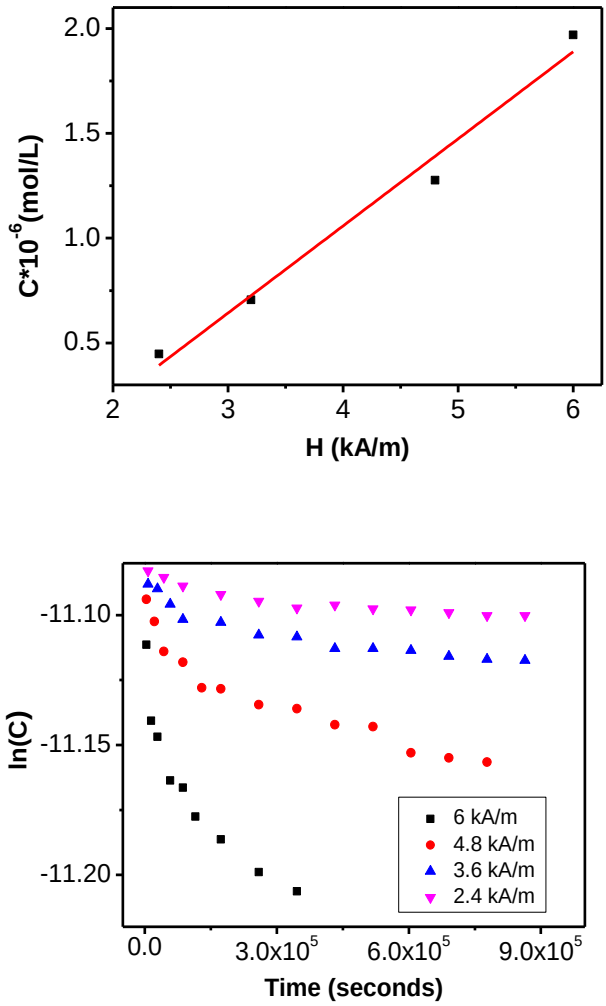

Fig. 4.5: (Top) Dependence of the saturation concentration of released dye in the supernatant with the magnetic field strength during the magnetically induced heating (R^2 = 0.9748). A good linear correlation is observed. (Bottom) Kinetic analysis of unimolecular release reaction. Plot of *ln(C)* vs. reaction time. No linear correlation was found, indicating that the dye release reactions do not follow a first-order rate law.

However, analysis indicated that there is no linear correlation between *ln(C)* and *t* (reaction time, seconds) (Fig. 4.5, bottom), and the dye release does not follow a classical first order rate law. The absence of a linear correlation indicates that the reaction is more complex than a classic first order reaction. This is easily imaginable since different processes take place during the dye release upon magnetically induced heating: a) breaking of the covalent bond between rhodamine B and silica, b) breaking of the mesoporous silica shell, and c) diffusion of the payload out of the pores of the mesoporous silica shell to the solution. Considering that each of these processes is temperature-dependent and follows individual rate laws, it is evident that the overall process (which is studied here) does not obey a classic first-order rate law. In addition to that, the system was not stirred, which may also impact the reaction kinetics.

We prefer not to speculate about the individual contributions of these effects, as we are currently unable to address these independently. Further, more detailed studies are therefore necessary.

4.4 Conclusions

In summary, mesoporous silica shells were successfully coated on the surface of IONPs and subsequently rhodamine B was grafted to the silica. The dye was released under magnetically induced heating. In contrast, little release is observed under heating with an oil bath (no release at room temperature). This highlights the suitability of covalently bound payload for use in drug delivery. The system acts as a model for stimulated release of a payload from a superparamagnetic nanoparticle drug carrier. We studied the influence of the magnetic field strength on the release. A clear increase in the release was observed under stronger magnetic fields. This is ascribed to increased heating of the superparamagnetic cores of the drug carrier. In addition, the silica shell degrades over the course of magnetic heating. A broad variety of functionalization of the silica shell is accessible, allowing for a range of payloads to be bound to the nanoparticles. These particles can also be useful for the release of two (or more) kinds of molecules. In that case, two (or more) different functional groups with different bond strength could be used. Thus, each payload could be released at different magnetic field strengths. The use and release of fluorescent dyes may also be exploited in simultaneous imaging (e.g., in fluorescent or nonlinear optical imaging) and photodynamic therapy [235]. Furthermore, the superparamagnetic properties of the carrier can also be exploited in MRI and hyperthermia. Overall, the presented platform offers a wide range of functionalities.

Acknowledgements

We are grateful to Johanna Jochum for SQUID measurements and Prof. Johan Billen for TEM measurements. The research leading to these results has received funding from the European Union Seventh Framework Programme [FP7/2007-2013] under the CosmoPHOS-nano project, grant agreement n° 310337. This work was financially supported by the Fund for Scientific Research Flanders (FWO), grant number G.0C02.13, and 322 Project of Ministry of Education and Training of Vietnam (TTL). SK is grateful to the German Academic Exchange Service (DAAD) for a postdoctoral fellowship. MB is grateful for financial support from the Funds for Innovation by Science and Technology in Flanders (IWT), grant number SB-111175. TV received financial support from the IWT (SBO-NANOCOMIT).

4.5 Supporting information

A.Experimental Section

Materials. All chemicals were used as received without further purification. Sodium oleate and iron (III) chloride hexahydrate (97 %) were obtained from Sigma Aldrich. Oleic acid, ethanol (analytical reagent grade) and ethyl acetate were purchased from VWR. HCl (37 %), heptane and toluene were ordered from Fisher Scientific. Acetone was purchased from Chem Lab. 3-Aminopropyltriethoxysilane (APTES) (97 %) were obtained from ABCR chemicals. 1-Octadecene (90 %, technical grade), chloroform, tetraethylorthosilicate (TEOS), cetyltrimethylammonium (CTAB) were purchased from Acros Organics. Sodium hydroxide, rhodamine B isothiocyanate (mixed isomers) (RITC) were supplied by Sigma Aldrich. Milli-Q water (18 MΩ cm^{-1}) was used to prepare all aqueous solutions.

Equipment and Characterization. Transmission electron microscopy measurements were performed on a 80 kV Zeiss EM-900 using 300 mesh Formvar coated copper grids. Distribution data were calculated by ImageJ. UV–Vis Spectrometry was performed on a Perkin Elmer Lambda 900 spectrometer. Magnetic properties of the nanoparticles were characterized by a superconducting quantum interference device magnetometer (SQUID, Quantum Design MPMS XL-5).

Synthesis of iron oxide@mesoporous silica core-shell nanoparticles. Uniform superparamagnetic IONPs were synthesized using the previously reported method by Bloemen et al. [75]. Iron oxide@mesoporous silica (Fe_3O_4@*m*-SiO_2) core/shell nanoparticles were prepared by the method published by Kim et al. [181] with modifications.

In a typical procedure, IONPs (12 mg) were dried from heptane solution and dissolved in 0.5 mL of chloroform. Simultaneously, 5 mL of 0.11 M aqueous CTAB solution was prepared at 35 ^{o}C and added to the chloroform solution. The mixture was stirred vigorously for 2 hours to form a turbid brown solution. Then, the mixture was heated up to 61.5 ^{o}C and kept stirring for 20 min to evaporate completely the chloroform, resulting in a transparent dark brown solution.

After that, the solution was transferred to a 100 mL round flask containing 45 mL of water and 0.3 mL of 2 M NaOH solution. The flask was connected to a condenser and heated up to 70 ^{o}C. To the solution, 0.5 mL of TEOS and 3 mL of ethyl acetate were consequently added. The reaction completed after 3 hours. After removing ethyl acetate from the solution by rotary evaporation, the particles were separated by centrifugation and dispersed again in ethanol. This step was repeated several times to remove excess reactants.

To extract CTAB from the silica shells, 40 µL of HCl 37 % was added to the dispersion and stirred at 60 ^{o}C for 3 hours or shaking overnight. The pH of the solution was tested by pH paper and should be around pH 1-2 to avoid dissolving the magnetic core [181]. MNPs were separated and washed 3 times and then dispersed again in 20 mL of ethanol.

In this experiment, the concentration of CTAB in 5 mL aqueous solution was varied from 0.275 M to 0.0275 M to investigate the effect of the amount of surfactant on the pore size of the silica shell.

Binding RITC to mesoporous silica shell. RITC was coupled to APTES before binding to *m*-SiO_2 shells as described in Scheme 1. RITC was reacted with APTES (molar ratio 1:10) under dark conditions for 2 days according to the literature [181] and the stock solution was kept at 4 ^{o}C. MNPs (12 mg, prepared with a CTAB concentration of 0.11 M) were collected from ethanol solution and re-dispersed in 20 mL of toluene. To this solution, 0.4 mL of RITC-APTES stock solution was added and the obtained solution was shaken overnight. Rhodamine B-MNPs (Rho-MNPs) were separated by centrifugation (11.000 rpm, 20 minutes). This step was repeated several times until the supernatant was colorless and its absorbance in UV-Vis spectrum was insignificant. Rho-MNPs were dispersed in 90 mL of ethanol and stored in a freezer. The Rho-MNP solution has the typical pink color of rhodamine B (Fig. 4.1b, Manuscript)

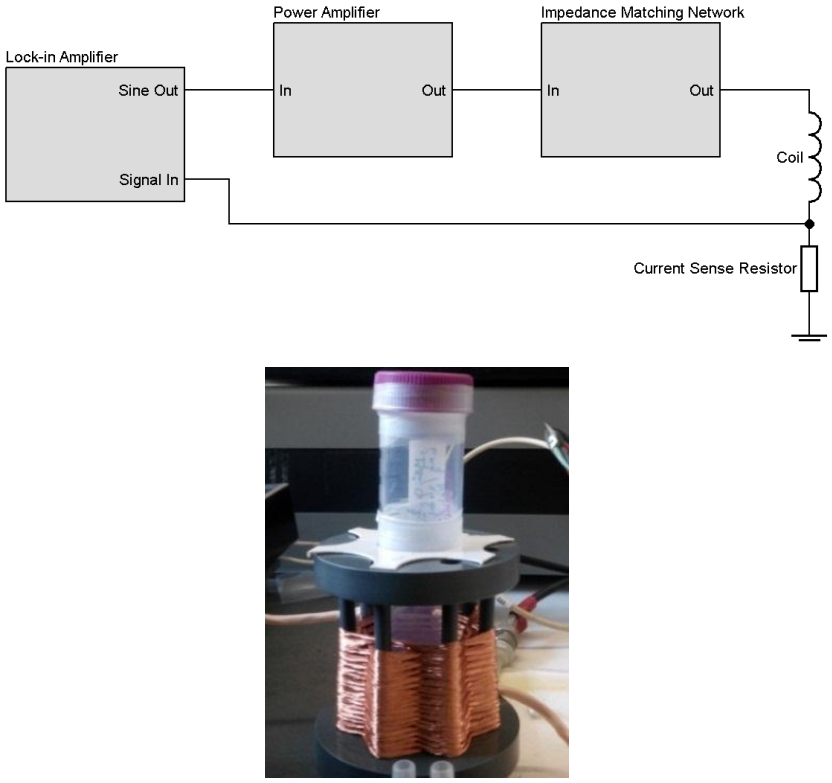

Fig. 4.S1: (top) Schematic for setup of the magnetic heating experiment, (bottom) The solution of Rho-MNPs was stored in a centrifugation tube and placed in the center of the copper coil.

When a current occurs in the circuit the strength of magnetic field is determined by:

$$H = \frac{n.I}{l} \qquad \text{(Eq. 4.S1)}$$

Where: *H* is the strength of the magnetic field (A/m), *n* is the number of turns of the coil, *I* is the current (A), *l* is the length of the coil (m).

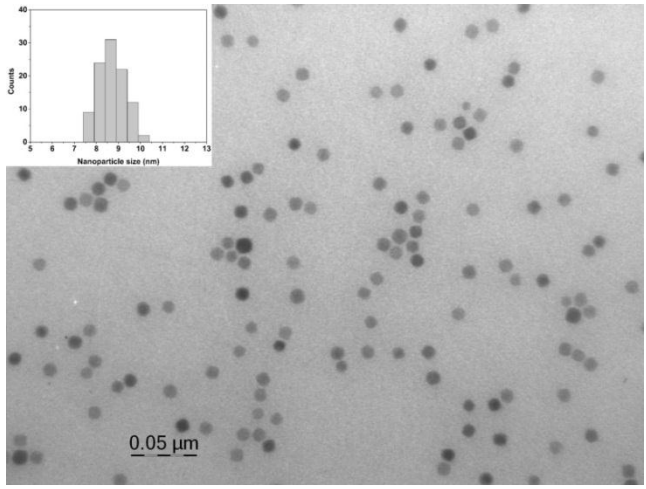

Fig. 4.S2: TEM image of oleic acid coated IONPs. The inset shows the particle size distribution: 8.6 ± 0.6 nm. Scale bar is 50 nm.

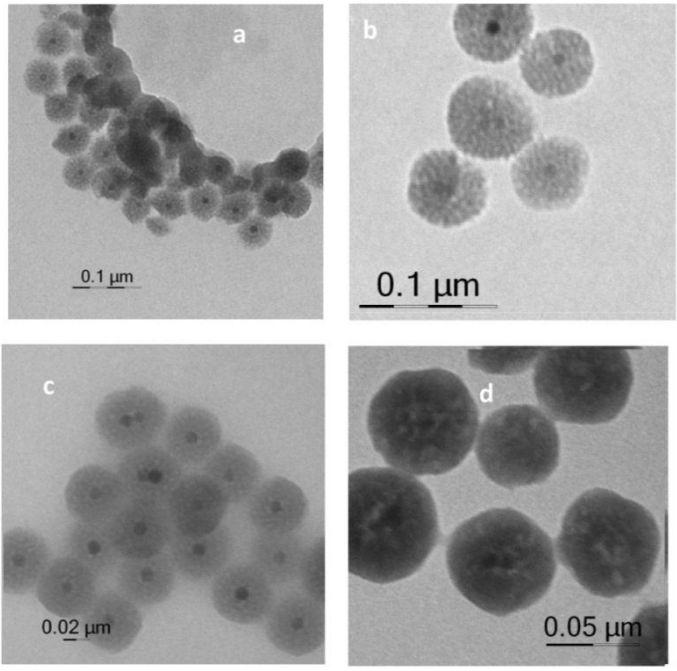

Fig. 4.S3: TEM images of *m*-SiO_2 coated IONPs obtained from different synthetic batches with various CTAB concentrations: 0.275 M (a), 0.11 M (b), 0.055M (c), 0.0275 M (d).

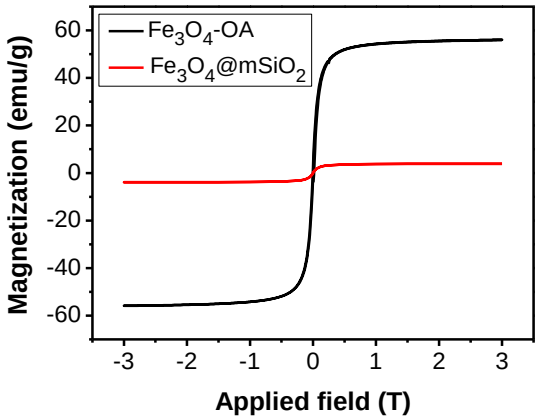

Fig. 4.S4: Magnetization curves of IONPs and mesoporous silica coated IONPs. After the synthesis, the particles retain superparamagnetic behavior.

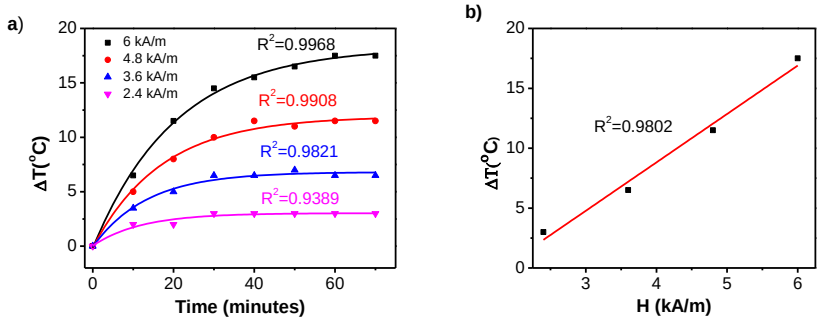

Fig. 4.S5: (Left) Temperature increase of RITC-MNPs solutions when applying a magnetic field with different strengths H=2.4, 3.6, 4.8, and 6 kA/m. The temperature of the bulk solutions was measured. Analysis of data shows a good fit between the data with an exponential function. Right: Plot of ΔT (^{o}C) versus magnetic field H (kA/m). A linear correlation is found, according to the fact that the applied magnetic fields fall within the linear regime of the Langevin-type magnetization curve.

Table 4.S1. Exponential fitting of temperature increase of the bulk solution in magnetic heating experiment by using model: $y = a-b*c^x$, where: y is the temperature increase (^oC), x is the time (minute) and a, b, c are the parameters of the model.

H/kAm^{-1}	Adj. R-Square	Value		Standard Error	ΔT(^{o}C) (y)
6	0.9989	a	18.263	0.336	17.5
		b	18.425	0.415	
		c	0.952	0.003	
4.8	0.99597	a	11.925	0.307	11.5
		b	12.035	0.444	
		c	0.943	0.005	
3.6	0.99752	a	6.808	0.198	6.5
		b	6.852	0.349	
		c	0.928	0.009	
2.4	0.99802	a	3.036	0.151	3
		b	2.989	0.286	
		c	0.920	0.018	

B. Calculation of the concentration of released dye

The concentration of the released dye in the supernatant (see manuscript) was determined photometrically. For this, we measured a calibration curve of free RITC (Fig. 4.S6). Using this calibration curve and the absorbance of released dye at a certain moment, we can calculate the concentration of released dye. Note that the solution was diluted by factor three before centrifugation. The calculated concentration of released dye is shown in Fig. 4.S7.

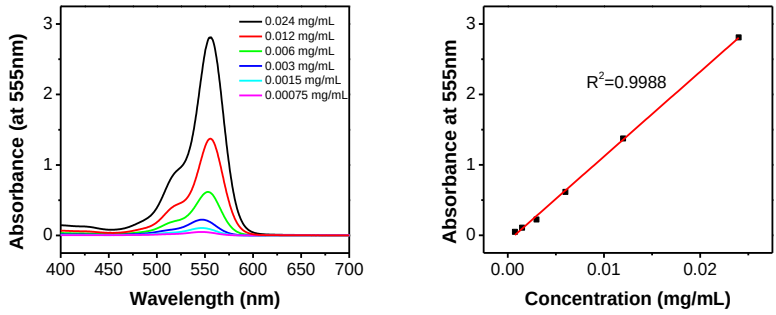

Fig. 4.S6: (Left) UV-Vis measurements of free RITC sample with different concentrations in Ethanol. (Right) Calibration curve of free RITC in ethanol. A linear fit shows the equation y=115.32*x. This equation was used to calculate the concentration of the dye in all the samples.

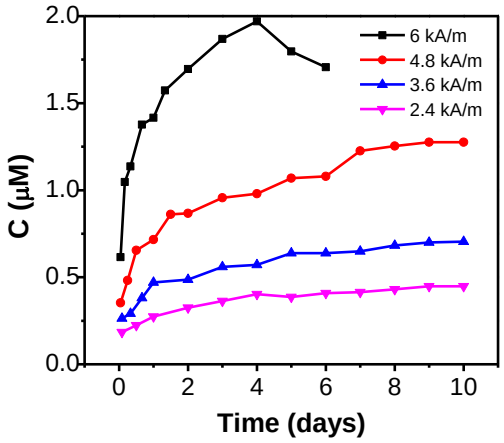

Fig. 4.S7: Calculated concentration of released dye in different magnetic heating experiments.

C. Calculation of the percentage of released dye.

It is interesting to determine the percentage of released dye from the nanoparticles during magnetic heating. Therefore it is essential to calculate the concentration of the dye in the solution before the magnetic heating experiment. As shown in the UV-Vis spectra of the solution before heating (Fig. 4.2, manuscript), the absorption is not only determined by the dye but also by extinction and scattering of the nanoparticles. To calculate the concentration of the dye in the NP solution, the contribution of the NPs has to be removed. This removal can be done by two methods: i) peak fitting and ii) dissolving silica shell by reaction with NaOH.

i) Peak Fitting

The scattering contribution can be estimated by analyzing the UV-Vis spectrum. The spectrum of the solution shows a peak at 555 nm, a shoulder at 524 nm, and a scattering signal with high intensity at the short wavelength region. Hence, there are three peaks used for the fitting: peak 1 (at 555 nm) and peak 2 (at 524 nm) are from the contribution of Rhodamine B, peak 3 (in the UV with very board FWHM) is from the contribution of the scattering of the nanoparticles. The cumulative fit peak is likely coincident with the spectrum of the solution, indicating that a good fit is found (Fig. 4.S8). To calculate the concentration of RITC in the NPs based on the fit peaks above, a new calibration curve based on fitted peaks from the dye is needed.

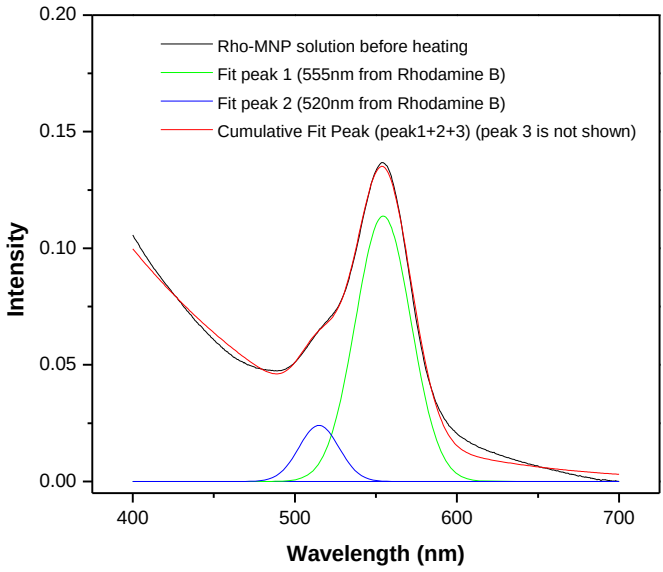

Fig. 4.S8: A peak analysis of the UV-Vis spectrum of the solution before heating (at 6 kA/m magnetic field). The spectrum of the solution shows a peak at 555 nm, a shoulder at 524 nm, and a scattering signal with high intensity at the short wavelength region. Hence, there are 3 peaks used for the fitting: peak 1 (at 555 nm) and peak 2 (at 524 nm) are from the contribution of the dye rhodamine B, peak 3 (far away in the UV light with very broad FWHM) is from the contribution of the scattering of the nanoparticles. Peak 3 is not shown.

ii) Dissolving the silica shell by reaction with NaOH

50 µL of 2M NaOH was added to the solution of Rho-MNPs and the solution was placed on a shaker for 16 h (room temperature) to dissolve the silica shell. After the reaction, the magnetic cores were removed by centrifugation whereas the dye remained in the supernatant. The absorbance of the dye was measured and is shown in Fig. 4.S9.

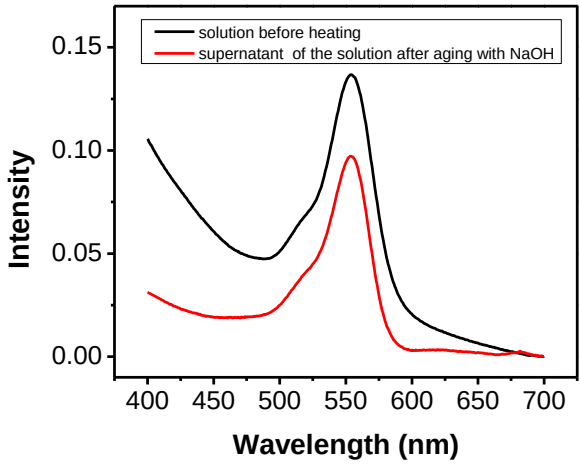

Fig. 4.S9: UV-Vis spectra of rhodamine B covalently bound with NPs (black) and rhodamine B releasing from NPs by adding NaOH to dissolve silica shell (red).

There is a good agreement between the calculated concentrations of the dye in Rho-MNP solution using the two methods. By using the method i, the calculated concentration of the dye is 0.0027 mg/mL, and is 0.00253 mg/mL when using method ii. The percentage of released dye after magnetic heating was calculated from this initial concentration (0.0027 mg/mL) and is presented in Fig. 4.S10.

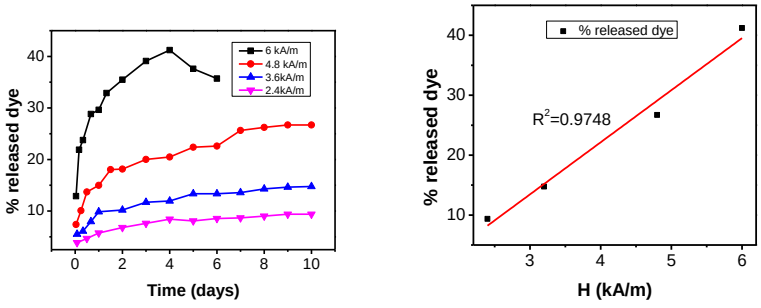

Fig. 4.S10: (Left) % released dye in the magnetic heating experiments. (Right) Linear correlation between % released dye after equilibration and the magnetic field strength.

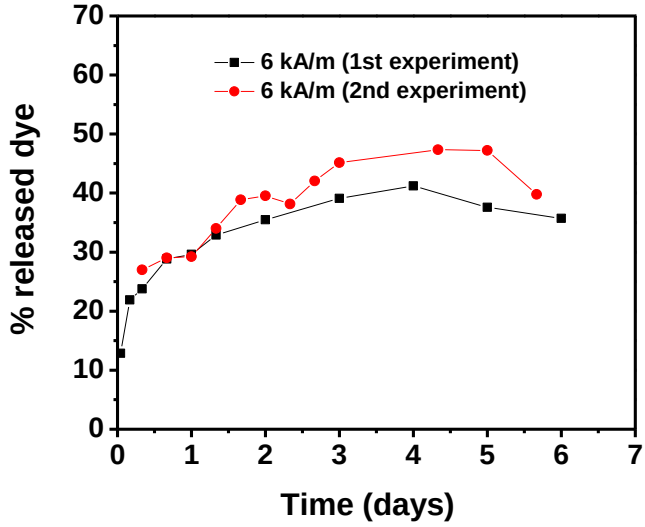

Fig. 4.S11: Magnetic heating experiment at 6 kA/m was repeated to verify the phenomenon that percentage of released dye reached maximum after ca. 4 days and then decreased.

Chapter 5

Magneto-fluorescent nanoparticles for nonlinear optical imaging

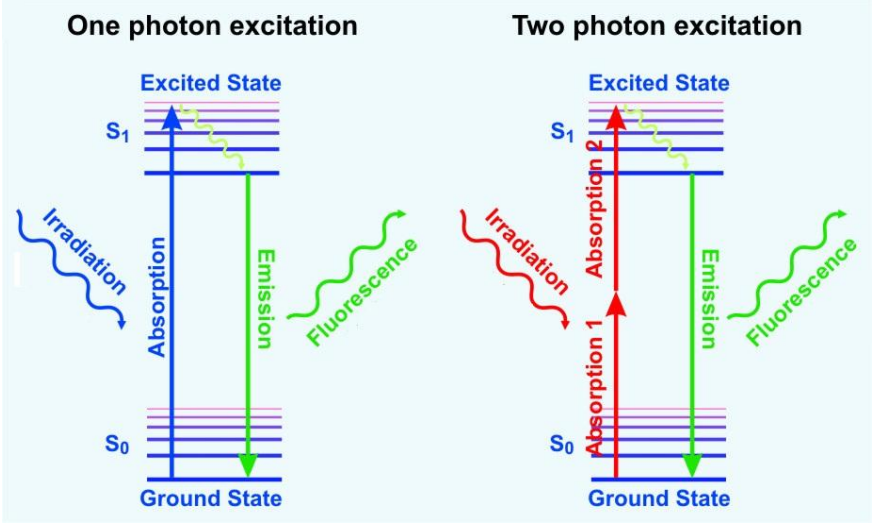

Author prepared nanoparticles and samples for nonlinear measurements. Dr. S. Van Cleuvenbergen performed 2-PF, HRS and TPF spectroscopy measurements. C. Verstraete performed SHG and 2-PF microscopy measurements. Analysis was done by author with the help from Dr. S. Van Celuvenbergen.

Abstract

We investigated rhodamine B functionalized magnetic iron oxide-mesoporous silica core-shell nanoparticles (Rho-MNPs) for fluorescence applications. Rho-MNPs combine strong fluorescent properties of the dye with superparamagnetic properties of the iron oxide core. Nonlinear optical (NLO) spectroscopy measurements moreover show promising NLO properties. Strong multiphoton fluorescence signals can be attributed to the rhodamine B dye. While the second-order NLO response is rather weak, the third-order NLO signal is strong. Indeed the second-order hyperpolarizability γ_{ZZZZ} is an order of magnitude higher than the benchmark chromophore β-carotene. These results highlight the potential of hybrid MNPs for multimodal imaging applications.

Key words: magneto-fluorescent nanoparticles, non-linear optics, imaging, iron oxide-silica core-shell NPs

5.1 Introduction

In recent years multifunctional nanomaterials have been widely studied as promising candidates for biomedical applications, e.g., drug delivery, controlled drug release, molecular imaging, nanomedicine, clinic diagnosis and therapy [5], [52], [220], [236]–[240]. In such applications, a wide variety of organic and inorganic nanoparticle formulations can be used as a basis for a functional system, e.g., polymers, silica, gold, magnetic nanoparticles. In particular, iron oxide based multifunctional nanoparticles were admitted as a class of advanced materials due to their ability to interact with external magnetic fields [59], [146], [240]. Iron oxide nanoparticles (IONPs) are often coated with a silica shell to provide high colloidal stability, biocompatibility and versatile surface functionality [59], [241]. Syntheses of IONPs and mesoporous silica shells with uniform and tunable size are readily achieved nowadays [52], [75], [181]). Loading these iron oxide-mesoporous silica core-shell nanoparticles with high concentrations of fluorescent molecules renders magneto-fluorescent nanoparticles (MFNPs) that can be employed in advanced applications for diagnosis (multimodal imaging) and/or therapy[241]–[244].

The typical method to form MFNPs relies on the loading of fluorescent components (fluorescent dye/polymer, quantum dot) onto the surface of (functionalized) IONPs [226], [241], [242], [244], resulting in rather low concentrations of fluorescent component on the outer surface. The growth of mesoporous silica shells on IONPs can overcome this limitation since the available mesoporous surface is much larger and the dye can be loaded on the outer surface as well as inside the pores[52].

While targeted and non-targeted MRI contrast agents based on superparamagnetic property of IONPs were studied a lot before (some of them even became commercial) [59], [237], nonlinear imaging applications of magnetic NPs have not yet gained attention. Considering the massive number of studies on MNPs reported so far [5], [220], [236]–[240] and the advantages of nonlinear optical (NLO) imaging techniques this approach can be of importance. Compared with traditional imaging techniques NLO imaging provides deeper penetration depths and less photodamage since most biological materials are transparent in the wavelength region where multiphoton excitation takes place (near-infrared and infrared region) [245], [246]. Additionally NLO imaging provides better resolution and enhanced imaging contrast [245]. While second harmonic imaging strongly relies on symmetry (the second-order response vanishes for centrosymmetric media), multiphoton fluorescence and third harmonic imaging are always allowed. Combining different modalities can further improve sensitivity, contrast and specificity. Although NLO properties of plasmonic NPs have been extensively studied [247]–[252], only few non-systematic studies have been carried out regarding the NLO properties of MFNPs [253].

In this work, we investigate the potential of rhodamine B functionalized iron oxide-mesoporous core-shell nanoparticles (Rho-MNPs) for NLO applications. NLO spectroscopy measurements of two photon fluorescence (2-PF), hyper-Rayleigh scattering (HRS) and third-harmonic scattering (THS) were performed at illumination wavelengths in the near-infrared region (840 and 1300 nm). The material shows a strong 2-PF signal, while both the first and second hyperpolarizability are in the range of the best known organic chromophores, while maintaining its superparamagnetic properties as evidenced by SQUID measurements. This highlights the possibility of using Rho-MNPs as multimodal nonlinear imaging agents and labels for 2PF, second-harmonic generation (SHG) and THG microscopy. As a test, two photon microscopy measurements (SHG and 2PF) were performed and clear images of particles were observed.

5.2. Experiments

5.2.1 Synthesis of rhodamine B functionalized iron oxide/mesoporous silica core/shell nanoparticles

The synthesis of IONPs was performed following a previously published protocol [75]. Synthesized IONPs are stabilized by a coating layer of oleic acid. Core-shell nanoparticles, consisting of iron oxide (core) and mesoporous silica (shell), were synthesized and then functionalized with a fluorescent dye (rhodamine B) according to another published protocol [52]. Cetyltrimethylammonium bromide (CTAB) was used as a template to form silica pores.

Note that all oleic acid coated IONPs using in this dissertation are from the same batch. Mesoporous silica coated IONPs and Rho-MNPs used in this chapter is from the same batch with particles used in Chapter 4.

5.2.2 Nonlinear optical spectroscopy measurements

NLO spectroscopy measurements in solution were performed using a femtosecond laser source tunable from 680 to 1300 nm (Insight DS+, Spectra Physics). The intensity is controlled by a half wave plate/ polarizer (S-out) combination. The light is then focused in a cuvette by an aspheric lens (f=8 mm) mounted on a computer controlled high precision translation stage to compensate for differences in focal length due to different wavelengths and/or solvents being used. The light generated in the focal volume is then coupled into a spectrometer (Bruker 500 ISM) by a pair of achromatic doublets (f1=30 mm, f2=200 mm) while the laser light is filtered out by appropriate band pass filters. A spectrum is read out by an EM-CCD camera (Andor, Ixon 897) operated in CCD mode. The input power is kept at 400 mW for all experiments. For the THS experiments the slit of the spectrometer was fully opened. This enhances sensitivity but also leads to broadening of the peaks.

5.2.3 Nonlinear optical microscopy measurements

The two-photon microscopy samples were prepared by drop-casting the nanoparticles (0.3 mg/mL) in water on microscopy slides, after which the samples were allowed to dry for several hours. Two-photon microscopy experiments were conducted on a commercial Olympus BX61WI-FV1200-M system (Olympus, Münster, Germany). The fundamental wavelength was set to 800 nm or 1100 nm (120 fs pulse width, 82 MHz pulse repetition rate) on the Deep see Insight DS+ laser of Spectra Physics. The polarization of the fundamental beam was controlled using a Glan-laser polarizer. For detection at 400 nm, a 425 lpxr dichroic mirror of Chroma was installed in front of the detector to collect the two-photon fluorescence signal and an ET 400/10 bandpass filter (Chroma) for the SHG-signal. For detection at 550 nm, a 560 lpxr dichroic mirror and ET 550/10 bandpass filter of Chroma were used. Detection was carried out non-descanned in backward reflection using a photon counter detector of Hamamatsu R3896 (Hamamatsu Photonics Co., Hamamatsu, Japan). The images (640 × 640 pixels) were recorded with a 15× Thorlabs LMV objective (NA of 0.35) and a pixel dwell time of 200 ms.

5.2.4 Magnetization measurement

Magnetic properties of the nanoparticles were characterized by a superconducting quantum interference device magnetometer (SQUID, Quantum Design MPMS XL-5).

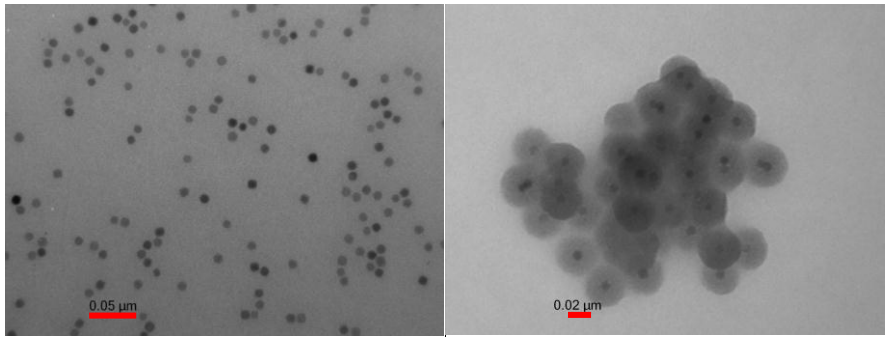

Fig. 5.1: (left) TEM image of oleic acid coated iron oxide nanoparticles (8.6 ± 0.6 nm) (scale bar 50 nm) and (right) iron oxide/mesoporous silica core/shell nanoparticles (58.0 ± 3.8 nm) (scale bar 20 nm).

5.3 Results and discussion

5.3.1 Characterization of nanoparticles

Characterization of materials by TEM, UV-Vis spectroscopy and SQUID measurements show results consistent with those reported in Chapter 4 [52]. Fig. 5.1 shows a TEM image of oleic acid coated IONPs (left) and a TEM image of iron oxide-mesoporous silica core-shell nanoparticles (right). Note that all oleic acid coated IONPs using in this dissertation are from the same batch. An analysis of particle size indicates that the size of IONPs is 8.6 ± 0.6 nm (Fig. 4.S2, SI, Chapter 4) and the core-shell nanoparticle size is 58.0 ± 3.8 nm, yielding a thickness of the silica shell of 24.7 nm. Most core-shell particles contain one iron oxide particle at the core. SQUID measurements indicate that the core-shell particles remain superparamagnetic since no coercivity or magnetic remanence is found (see Fig. 4.S4, SI, Chapter 4).

UV-Vis spectra of free rhodamine B and Rho-MNPs at the same concentration of the dye (c=18.37 µM, solvent ethanol) are shown in Fig. 5.2. The spectrum of Rho-MNPs shows a peak at 555 nm. There is a small red-shift in comparison with that of the free dye, that can be attributed to the interaction of the dye with the silica shell, resulting in a change in electronic structure of the dye.

5.3.2 Two-photon fluorescence (2-PF) spectroscopy

The laser source was operated at 1110 nm to match the two-photon excitation with the absorption of rhodamine B ($\lambda_{max,\ EtOH}$=555 nm, $\lambda_{emission}$=568 nm [254]). Rhodamine B

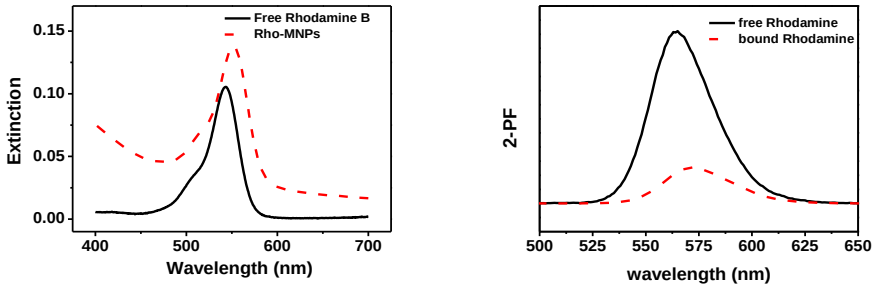

Fig. 5.2: Extinction spectra (left) and 2-PF (right) of free and bound rhodamine B for an equal concentration of rhodamine B (solvent ethanol).

functionalized MNPs display a strong two-photon fluorescence (2-PF) signal. Since the iron oxide core and silica are non fluorescent themselves [236], the 2-PF can be attributed exclusively to the payload, as can also be deduced from the spectral features. In Fig. 5.2 the 2-PF signal of free rhodamine B is compared with that of the functionalized MNPs, with the rhodamine B concentration equal for both samples. We observe a small red shift (from 566 to 571 nm) upon functionalization consistent with the UV-Vis spectra.

A 5-fold decrease in 2-PF intensity is evident, and is most likely explained by fluorescence quenching by the magnetic core and/or by the silica shell. Fluorescence quenching in the presence of IONPs was observed before [255], [256], however the mechanism is not entirely clear as both static (e.g., equilibrium complexation) and dynamic (e.g., collisional) mechanism occur. Fluorescence quenching was also observed in the presence of a silica shell due to the proximity of dye molecules to the shell [253], [257].

During 2-PF measurements, the fluorescence intensity was stable, allowing materials to be used in imaging or labeling applications. This high stability is an advantage compared with fluorescence dyes with short fluorescence lifetimes [253], [257].

5.3.3 Hyper-Rayleigh scattering spectroscopy

The use of MNPs as potential second-harmonic labels relies primarily on their first hyperpolarizability β. Hyper-Rayleigh scattering (HRS) is a powerful method for measuring β of molecules [258], [259] or nanoparticles [247], [248] in solution. We measured β_{HRS} of functionalized and unfunctionalized MNPs at 1260 nm and found

high values of (20±3) × 10^{-27} esu and (21 ± 3) × 10^{-27} esu respectively, by comparing the spectra of solutions of known concentration and comparing the second harmonic intensity with that of the bare solvent reference ($\beta_{HRS\ ethanol,1260\ nm}$ = 0.57 × 10^{-30} esu, corrected with two-level model [260]). Both values are within experimental error identical, indicating that the response stems from the particles themselves rather than the dye loaded in the shell. The value of unbound rhodamine B was also evaluated in the same manner and was found to be much lower as expected, adding up to (120 ± 20) × 10^{-30} esu on resonance at 840 nm (or $\beta_{HRS\ rhodamine\ B,1260\ nm}$ = (280 ± 42) × 10^{-30} esu as calculated by using two level model) . This low value of unbound rhodamine B explains why the second harmonic signal is unaffected by the presence of the loaded silica shell.

Since the hyperpolarizability is strongly size-dependent, it is often normalized to the number of electrons or atoms. For nanoparticles, the figure of merit is calculated as β^2/atom, hence the actual value of first hyperpolarization for metal nanoparticles is $\beta' = \frac{\beta}{\sqrt{number\ of\ atom}}$: β'_{Ag}=(5600 ± 1100) × 10^{-30} esu, β'_{Au}= (2800 ± 500) × 10^{-30} esu [247], [248]. For 8.6 nm Fe_3O_4 nanoparticles the total number of atoms is 5208 (2232 Fe atoms and 2976 O atoms), which makes β'= (0.78 ± 0.11) × 10^{-30} esu. Due to the absence of plasmonic effects in Fe_3O_4 nanoparticles, the values obtained here are substantially lower. However, if we compare with organic chromophores, this value is in the range of the best known organic NLO dyes [258], [261]–[263].

5.3.4 Third harmonic scattering (THS) spectroscopy

To evaluate the third-order NLO properties of MNPs third harmonic scattering was evaluated at an excitation wavelength of 1300 nm. A strong signal is generated both by the functionalized and the bare MNPs at an identical concentration of 1.68 × 10^{-16} particles/L (see Fig. 5.4). As a reference a solution of pure ethanol, with a known second hyperpolarizability γ_{ZZZZ} of 2.71 × 10^{-36} esu [264] was used to estimate the γ_{ZZZZ} of the MNPs analogous with the calculation of the first hyperpolarizability β. We found that γ_{ZZZZ} of the bare and functionalized MNPs were identical within error, i.e. (93 ± 10) × 10^{-33} esu and (98 ± 10) × 10^{-33} for the functionalized and the bare MNPs respectively. The strong THS signal can hence be attributed to the MNPs, since the presence of rhodamine B does not have a significant effect on the second hyperpolarizability. The small difference between both can be attributed to reabsorption of THS by rhodamine or multiple scattering by the silica shell. The second hyperpolarizability of the MNP is one order of magnitude larger than that of the benchmark chromophore β-carotene (10 × 10^{-33} esu, measured on-resonance) [265] and much larger than that of π-conjugated polyacetylene or silicon-ring oligomers with the same double bonds (12 double bonds, γ_{ZZZZ} ~ 60 × 10^{-36} esu [266]). This highlights their potential to be used as third harmonic imaging labels.

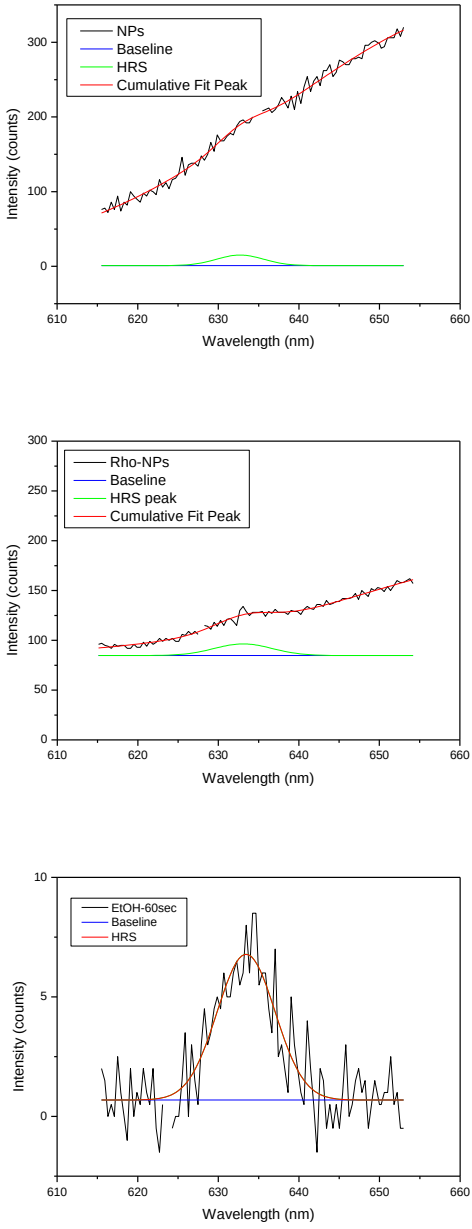

Fig. 5.3: Hyper-Rayleigh Scattering spectroscopy of MNPs (top), Rho-MNPs (middle) and the solvent ethanol (bottom). The fundamental wavelength is 1260 nm.

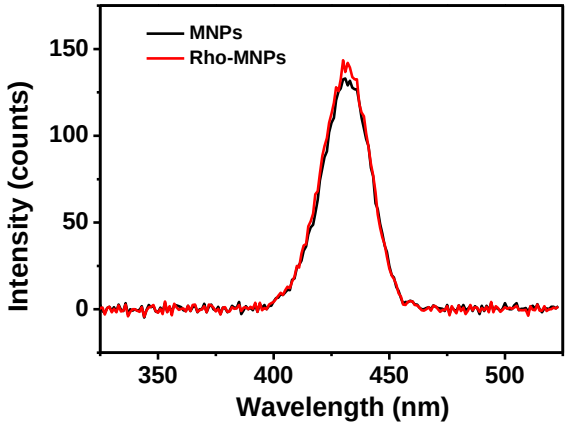

Fig. 5.4: THS of bare and functionalized MNPs for identical concentrations.

5.3.5 Nonlinear optical microscopy

SHG and 2-PF microscopy measurements of Rho-MNPs were performed at 800 and 1100 nm. Fig. 5.5 shows images of 2PF and SHG at the wavelength 1100 nm. The SHG signal strength is overall negligible or weak, only a few larger droplets are clearly visible in the SHG image (Fig. 5.5). The SHG signal strength fundamentally relies on both the molecular (microscopic) efficiency of the chromophore, and the macroscopic organization of the bulk medium. The latter requirement precludes SHG in centrosymmetric materials within the electric dipole approximation. The normalized hyperpolarizability ($\beta' = \frac{\beta}{\sqrt{number\ of\ atom}}$) of the Rho-MNPs, though lower than that of Au and Ag, is quite high, but spherical particles tend to form isotropic aggregates which quenches the SHG signal of the droplets. Small deviations from centrosymmetry and symmetry breaking at surfaces can lead to measurable signal in some larger particles. In contrast, 2-PF was easily detectable in the droplets found on the microscopy slide not having the strict symmetry requirements associated with SHG. Other measurements at 800 nm gave similar results.

The samples were also exposed to high power laser light for longer periods to see if there was any photobleaching. We selected a specific area in the 2-PF image and the light intensity was recorded over time as shown in Fig. 5.6. The measured signal was stable, confirming that no photobleaching occurred for the experimental conditions used here (laser power 200 mW – fundamental wavelength 1100 nm).

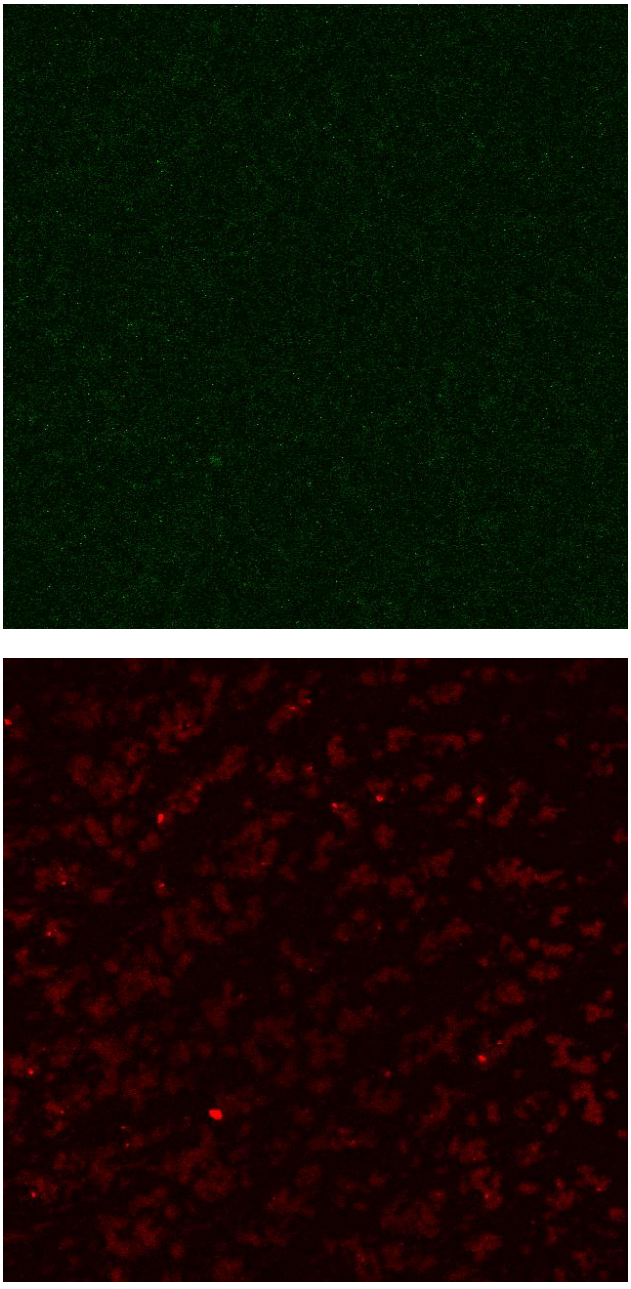

Fig. 5.5: SHG (top) and 2-PF (bottom) microscopy images of Rho-MNPs samples performed at 1100 nm. Particles are found in the 2PF image, however they are not found in the SHG image.

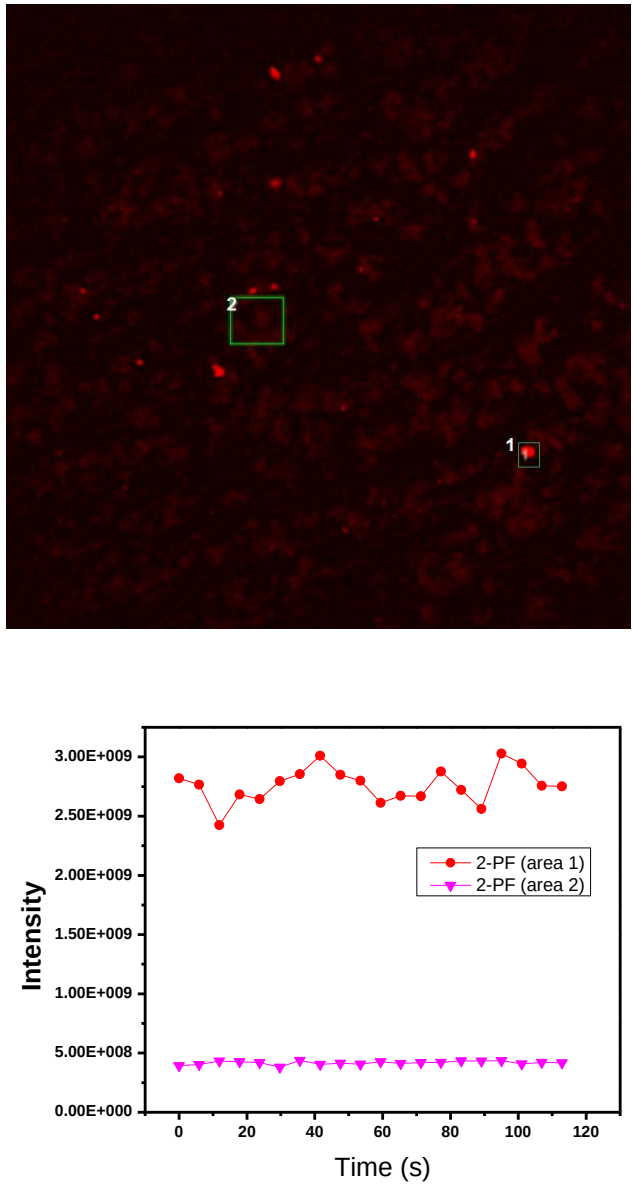

Fig. 5.6: (Top) Two areas of image were chosen for the study of photobleaching. (Bottom) Intensity of 2-PF signals coming from area 1/area 2 where particles are present/absent. Measurements were performed at a fundamental wavelength of 1100 nm.

5.3. Conclusions

In summary, rhodamine B functionalized iron oxide-mesoporous silica NPs were synthesized maintaining their superparamagnetic properties. A well-defined core-shell structure was evident from TEM images. We investigated the NLO properties (2-PF, HRS, THS) of these core-shell nanoparticles. Functionalization with rhodamine B results in strong 2-PF signal when excited at 1100 nm. We also measured the first and second hyperpolarizability and found high values comparable or higher than with the best organic chromophores. We conclude that MFNPs have potential to be used as labels in nonlinear imaging applications in the infrared region, which is particularly interesting for biological deep tissue imaging. Furthermore, the iron oxide core provides additional functionality, and can be exploited for MRI, magnetothermal heating, drug release, drug delivery and theranostic applications.

Chapter 6

Conclusions and outlook

6.1 Conclusions

In general, the functionalization of IONPs with a wide range of capping agents and their potential applications were presented in this doctoral research. Thanks to tireless efforts of our colleagues before, low-cost, highly reproducible and well-defined IONPs were already available [63], [75]. This work focused on the development of the surface functionalization. Various small molecules (e.g., PEG-silane, carboxyl-terminated-PEG-silane, APTMS, dopamine) and inorganic shells (gold, mp-SiO_2) were used as coating agents to form a versatile platform of functionalized NPs. These coating agents provide highly colloidal stability and functional groups for IONPs. We also separately explored the abilities of the NPs in bio-entities binding, non-linear imaging and drug delivery and release. These abilities are crucial for particles to be used in theranostic nanomedicines – in which the particles act simultaneously as a diagnostic and a therapeutic agent.

In Chapter **2** we presented the synthesis of a series of carboxyl functionalized magnetic NPs. The particles showed a good colloidal stability whereas the functional group carboxyl allowed coupling with bio-entities in the presence of EDC/NHS. The protein BSA was chosen as a case study, and the amount of bound protein was quantified by Bradford assays.

Although only BSA is used in this coupling study, it is likely that the procedure can be applied for other bio-entities as long as they have free amino groups on the surface. A typical example is the preparation of antibodies bound to NPs using the same method [67]. Note that this kind of conjugation plays an important role in tumor targeting agents in cancer diagnostic or treatment as mentioned in the Section 1.2. Moreover, thanks to the superparamagnetic properties of the core, the system also can be used in magnetic separation for bio-entities.

In Chapter **3** we described two approaches to synthesize IOGNPs: synthesis in aqueous phase and organic phase. The obtained particles can be dispersed in water, possess both magnetic and plasmonic properties but the magnetization of the core-shell structures was severely decreased. Furthermore, multilayer nanoshells were also synthesized in order to combine all properties of the magnetic core, the plasmonic shell and the mesoporous silica shell.

The presence of Au nanoshells provides more possibilities in bio-entity coupling because Au has high affinity for biological molecules. The study also showed promising optical properties of the nanoshells. The SPR bands are tunable and it is possible to shift them to the NIR region which can be exploited in deep tissue noninvasive imaging and photon-induced hyperthermia. Together with the hyperthermia activated by a laser source, magnetic MuNPs can generate heat when exposing them to an AC magnetic field. This property can be exploited in magnetically triggered drug release which is presented in Chapter **4**.

In Chapter **4**, we show a new case study of drug release. A payload (a fluorescent dye-rhodamine B) was covalently bound to *mp-*SiO_2 coated IONPs and then was released under magnetically induced heating. A well-defined core-shell structure was evident from TEM images. In the presence of an AC magnetic field, the iron oxide core was strongly heated. This led to a high temperature increase surrounding the core which is sufficient to break the bonds between the payload and the particles. We also studied the influence of the magnetic field strength on the release. A clear increase in the release was observed under stronger magnetic fields.

The release of a covalently bound payload is the new aspect of dye release. Moreover, a broad variety of functionalization of the silica shell is accessible, allowing for a range of payloads to be bound to the nanoparticles. The results suggest that these particles can also be useful for the release of two (or more) kinds of molecules. In that case, two (or more) different functional groups with different bond strength could be used. Thus, each payload could be released at different magnetic field strengths.

Chapter **5** shows the utilization of magneto-fluorescent nanostructures as nonlinear imaging agents. We investigated the NLO properties (2-PF, HRS, THS) of these core-shell nanoparticles. Functionalization of iron oxide- *mp*-SiO_2 NPs with Rhodamine B results in strong 2-photon fluorescence signal at 1100 nm. We also measured the first and second hyperpolarizability and found high values comparable or higher than with the best organic chromophores. We conclude that MFNPs have potential to be used as labels in nonlinear imaging applications in the near-infrared region, which is particularly interesting for biological deep tissue imaging.

In conclusion, the presented iron oxide based multifunctional NPs offer a wide range of functionalities, which will lead to many future research in biomedical applications.

6.2 Outlook

In this section, we discuss the recommendations for future research. Regarding to synthesis protocols, even though versatile iron oxide based MuNPs were synthesized successfully, several critical steps in the synthesis can be optimized to improve the efficiency of potential applications. For example, superparamagnetic IONPs synthesized from thermal decomposition method exhibited as great nanocores in the formulation of MuNPs, however their magnetization, can be improved by changing reaction parameters. This renders MuNPs more advantages, especially in applications in which the bioseparations are required. The control of gold shell growth in aqueous medium also needs to be improved in order to achieve well-defined IOGNPs with SPR band red-shifted to NIR region. This property will supplement their potential in the biological deep tissue imaging, besides nonlinear optical imaging as described in Chapter 5.

Iron oxide based MuNPs have great potential in biomedical applications and several applications of these nanostructures were explored through the dissertation. More future studies in specific applications were also suggested in the Section 6.1. Here, we discuss the potentiality of MuNPs as theranostic nanomedicines. Fluorescent dye-tagged spherical multilayered nanoshells were synthesized in Chapter 3. Moreover, MuNPs exhibited their ability in NLO imaging applications in the near-infrared region as described in Chapter 5. These techniques provide deeper penetration depths and therefore can be utilized in living cell tracking and photon-induced hyperthermia. In addition, the magnetically induced hyperthermia also can be achieved due to the presence of iron oxide cores, leading to the potential of controlled drug release and hyperthermia treatment (see Chapter 4). For these reasons, iron oxide based MuNPs are expected to be the first generation of nanomedicines for human therapy in the near future.

Bibliography

[1] M. J. Hayat, N. Howlader, M. E. Reichman, and B. K. Edwards, "Cancer Statistics, Trends, and Multiple Primary Cancer Analyses from the Surveillance, Epidemiology, and End Results (SEER) Program," *Oncologist*, vol. 12, pp. 20–37, 2007.

[2] G. M. Cooper, "Cancer," in *The Cell: A Molecular Approach*, Second edi., Sunderland: Sinauer Associates, 2000.

[3] "Cancer statistics at a glance," *Canadian cancer society*, 2016. [Online]. Available: http://www.cancer.ca/en/cancer-information/cancer-101/cancer-statistics-at-a-glance/?region=on. [Accessed: 15-Aug-2016].

[4] "Cancer death rate in Vietnam among world's highest," *Xinhuanet*, 2013. [Online]. Available: http://news.xinhuanet.com/english/health/2013-04/12/c_132304583.htm. [Accessed: 15-Aug-2016].

[5] C. S. S. R. Kumar and F. Mohammad, "Magnetic nanomaterials for hyperthermia-based therapy and controlled drug delivery," *Adv. Drug Deliv. Rev.*, vol. 63, no. 9, pp. 789–808, 2011.

[6] A. Jordan, "thermotherapy using Magnetic Nanoparticles: Principles and Clinical Application of Nanotherapy," in *EuroNanoForum*, 2005, pp. 76–80.

[7] Z. Li, J. C. Barnes, A. Bosoy, J. F. Stoddart, and J. I. Zink, "Mesoporous silica nanoparticles in biomedical applications," *Chem. Soc. Rev.*, vol. 41, no. 7, pp. 2590–2605, 2012.

[8] K. Strebhardt and A. Ullrich, "Paul Ehrlich's magic bullet concept: 100 years of progress," *Nat Rev Cancer*, vol. 8, no. 6, pp. 473–480, Jun. 2008.

[9] J. Conniot, J. M. Silva, J. G. Fernandes, L. C. Silva, R. Gaspar, S. Brocchini, H. F. Florindo, and T. S. Barata, "Cancer immunotherapy : nanodelivery approaches for immune cell targeting and tracking," *Front. Chem.*, vol. 2, no. November, pp. 1–27, 2014.

[10] D. Peer, J. M. Karp, S. Hong, O. C. Farokhzad, R. Margalit, and R. Langer, "Nanocarriers as an emerging platform for cancer therapy," *Nat Nano*, vol. 2, no. 12, pp. 751–760, 2007.

[11] U. Häfeli, M. Zborowski, J. Teller, and H. Putzar, "Applications of Magnetic Targeting in Diagnosis and Therapy — Possibilities and Limitations : A Mini-Review," *Hybridoma*, vol. 16, no. 1, pp. 109–117, 1997.

[12] C. A. J. Jr, P. Travers, M. Walport, and M. J. Shlomchik, *Immunobiology: The Immune System in Health and Disease*, 5th ed. New York: Garland Science, 2001.

[13] P. Cherukuri, E. S. Glazer, and S. A. Curley, "Targeted hyperthermia using metal nanoparticles," *Adv. Drug Deliv. Rev.*, vol. 62, no. 3, pp. 339–345, 2010.

[14] M. Arruebo, M. Valladares, and Á. González-Fernández, "Antibody-Conjugated Nanoparticles for Biomedical Applications," *J. Nanomater.*, vol. 2009, pp. 1–24, 2009.

[15] M. Bloemen, "Immunomagnetic separation of bacteria by iron oxide nanoparticles," University of Leuven, 2015.

[16] "What's so special about nanoscale?," *National Nanotechnology Initiative*. [Online]. Available: http://www.nano.gov/nanotech-101/special. [Accessed: 15-Aug-2016].

[17] A. Henglein, "Small-particle research: physicochemical properties of extremely small colloidal metal and semiconductor particles," *Chem. Rev.*, vol. 89, no. 8, pp. 1861–1873, 1989.

[18] L. Spanhel, H. Weller, and A. Henglein, "Photochemistry of semiconductor colloids. 22. Electron ejection from illuminated cadmium sulfide into attached titanium and zinc oxide particles," *J. Am. Chem. Soc.*, vol. 109, no. 22, pp. 6632–6635, 1987.

[19] H. C. Youn, S. Baral, and J. H. Fendler, "Dihexadecyl phosphate, vesicle-stabilized and in situ generated mixed cadmium sulfide and zinc sulfide semiconductor particles: preparation and utilization for photosensitized charge separation and hydrogen generation," *J. Phys. Chem.*, vol. 92, no. 22, pp. 6320–6327, 1988.

[20] F. Mohammad, G. Balaji, A. Weber, R. M. Uppu, and C. S. S. R. Kumar, "Influence of Gold Nanoshell on Hyperthermia of Super Paramagnetic

Iron Oxide Nanoparticles (SPIONs).," *J. Phys. Chem. C. Nanomater. Interfaces*, vol. 114, no. 45, pp. 19194–19201, 2010.

[21] E. Katz and I. Willner, "Integrated Nanoparticle–Biomolecule Hybrid Systems: Synthesis, Properties, and Applications," *Angew. Chemie Int. Ed.*, vol. 43, no. 45, pp. 6042–6108, 2004.

[22] Z. Liu, D. Elbert, C.-L. Chien, and P. C. Searson, "FIB/TEM Characterization of the Composition and Structure of Core/Shell Cu−Ni Nanowires," *Nano Lett.*, vol. 8, no. 8, pp. 2166–2170, 2008.

[23] L. Wang, H.-Y. Park, S. I.-I. Lim, M. J. Schadt, D. Mott, J. Luo, X. Wang, and C.-J. Zhong, "Core@shell nanomaterials: gold-coated magnetic oxide nanoparticles," *J. Mater. Chem.*, vol. 18, no. 23, pp. 2629–2635, 2008.

[24] J. H. Kim, H. W. Chung, and T. R. Lee, "Preparation and characterization of palladium shells with gold and silica cores," *Chem. Mater.*, vol. 18, no. 26, pp. 4115–4120, 2006.

[25] B. S. Behrens, H. Bönnemann, and N. Matoussevitch, "Air-stable Co- , Fe- , and Fe / Co-Nanoparticles and Ferrofluids," *Z. Phys. Chem*, vol. 220, pp. 3–40, 2006.

[26] T. Zhang, J. L. Stilwell, D. Gerion, L. Ding, O. Elboudwarej, P. A. Cooke, J. W. Gray, A. P. Alivisatos, and F. F. Chen, "Cellular Effect of High Doses of Silica-Coated Quantum Dot Profiled with High Throughput Gene Expression Analysis and High Content Cellomics Measurements," *Nano Lett.*, vol. 6, no. 4, pp. 800–808, 2006.

[27] N. Matoussevitch, A. Gorschinski, W. Habicht, J. Bolle, E. Dinjus, H. Bönnemann, and S. Behrens, "Surface modification of metallic Co nanoparticles," *J. Magn. Magn. Mater.*, vol. 311, no. 1, pp. 92–96, 2007.

[28] X.-B. Zhang, J.-M. Yan, S. Han, H. Shioyama, and Q. Xu, "Magnetically Recyclable Fe@Pt Core−Shell Nanoparticles and Their Use as Electrocatalysts for Ammonia Borane Oxidation: The Role of Crystallinity of the Core," *J. Am. Chem. Soc.*, vol. 131, no. 8, pp. 2778–2779, 2009.

[29] S. H. Joo, J. Y. Park, C.-K. Tsung, Y. Yamada, P. Yang, and G. A. Somorjai, "Thermally stable Pt/mesoporous silica core-shell nanocatalysts for high-temperature reactions," *Nat Mater*, vol. 8, no. 2, pp. 126–131, 2009.

[30] J. Zhai, M. Huang, and S. Dong, "Electrochemical Designing of Au/Pt Core Shell Nanoparticles as Nanostructured Catalyst with Tunable

Activity for Oxygen Reduction," *Electroanalysis*, vol. 19, no. 4, pp. 506–509, 2007.

[31] C. M. Sweeney, W. Hasan, C. L. Nehl, and T. W. Odom, "Optical Properties of Anisotropic Core−Shell Pyramidal Particles," *J. Phys. Chem. A*, vol. 113, no. 16, pp. 4265–4268, 2009.

[32] P. Reiss, M. Protière, and L. Li, "Core/Shell Semiconductor Nanocrystals," *Small*, vol. 5, no. 2, pp. 154–168, 2009.

[33] E. D. Smolensky, M. C. Neary, Y. Zhou, T. S. Berquo, and V. C. Pierre, "Fe 3O4@organic@Au: core–shell nanocomposites with high saturation magnetisation as magnetoplasmonic MRI contrast agents," *Chem. Commun.*, vol. 47, no. 7, pp. 2149–2151, 2011.

[34] A. H. Latham and M. E. Williams, "Controlling Transport and Chemical Functionality of Magnetic Nanoparticles," *Acc. Chem. Res.*, vol. 41, no. 3, pp. 411–420, 2008.

[35] G. F. Schneider, V. Subr, K. Ulbrich, and G. Decher, "Multifunctional Cytotoxic Stealth Nanoparticles. A Model Approach with Potential for Cancer Therapy," *Nano Lett.*, vol. 9, no. 2, pp. 636–642, 2009.

[36] S. Sengupta, D. Eavarone, I. Capila, G. Zhao, N. Watson, T. Kiziltepe, and R. Sasisekharan, "Temporal targeting of tumour cells and neovasculature with a nanoscale delivery system," *Nature*, vol. 436, no. 7050, pp. 568–572, Jul. 2005.

[37] H. Freichels, V. Pourcelle, R. Auzély-Velty, J. Marchand-Brynaert, and C. Jérôme, "Synthesis of Poly(lactide-co-glycolide-co-ε-caprolactone)-graft-mannosylated Poly(ethylene oxide) Copolymers by Combination of 'Clip' and 'Click' Chemistries," *Biomacromolecules*, vol. 13, no. 3, pp. 760–768, 2012.

[38] S. Brocchini, A. Godwin, S. Balan, J. Choi, M. Zloh, and S. Shaunak, "Disulfide bridge based {PEGylation} of proteins," *Adv. Drug Deliv. Rev.*, vol. 60, no. 1, pp. 3–12, 2008.

[39] K. Wang, X. He, X. Yang, and H. Shi, "Functionalized Silica Nanoparticles: A Platform for Fluorescence Imaging at the Cell and Small Animal Levels," *Acc. Chem. Res.*, vol. 46, no. 7, pp. 1367–1376, 2013.

[40] H. Kumar, T. Kawai, and S. Akira, "Pathogen recognition in the innate immune response," *Biochem. J.*, vol. 420, no. 1, pp. 1–16, 2009.

[41] M. Liong, J. Lu, M. Kovochich, T. Xia, S. G. Ruehm, A. E. Nel, F. Tamanoi, and J. I. Zink, "Multifunctional inorganic nanoparticles for imaging, targeting, and drug delivery.," *ACS Nano*, vol. 2, no. 5, pp. 889–96, 2008.

[42] Z. Fan, M. Shelton, A. K. Singh, D. Senapati, S. A. Khan, and P. C. Ray, "Multifunctional plasmonic shell-magnetic core nanoparticles for targeted diagnostics, isolation, and photothermal destruction of tumor cells," *ACS Nano*, vol. 6, no. 2, pp. 1065–1073, 2012.

[43] E. Aznar, M. D. Marcos, R. Martínez-Máñez, F. Sancenón, J. Soto, P. Amorós, and C. Guillem, "pH- and photo-switched release of guest molecules from mesoporous silica supports.," *J. Am. Chem. Soc.*, vol. 131, no. 19, pp. 6833–43, 2009.

[44] J. T. Wilson, S. Keller, M. J. Manganiello, C. Cheng, C.-C. Lee, C. Opara, A. Convertine, and P. S. Stayton, "pH-Responsive Nanoparticle Vaccines for Dual-Delivery of Antigens and Immunostimulatory Oligonucleotides," *ACS Nano*, vol. 7, no. 5, pp. 3912–3925, 2013.

[45] P. S. Tofts, "Optimal detection of blood-brain barrier defects with Gd-DTPA MRI—The influences of delayed imaging and optimised repetition time," *Magn. Reson. Imaging*, vol. 14, no. 4, pp. 373–380, 1996.

[46] R. Weissleder, A. Moore, U. Mahmood, R. Bhorade, H. Benveniste, E. A. Chiocca, and J. P. Basilion, "In vivo magnetic resonance imaging of transgene expression," *Nat Med*, vol. 6, no. 3, pp. 351–354, Mar. 2000.

[47] H. Nakamura, N. Ito, F. Kotake, Y. Mizokami, and T. Matsuoka, "Tumor-detecting capacity and clinical usefulness of SPIO-MRI in patients with hepatocellular carcinoma," *J. Gastroenterol.*, vol. 35, no. 11, pp. 849–855, 2000.

[48] R. M. Taylor, D. L. Huber, T. C. Monson, A.-M. S. Ali, M. Bisoffi, and L. O. Sillerud, "Multifunctional iron platinum stealth immunomicelles: targeted detection of human prostate cancer cells using both fluorescence and magnetic resonance imaging," *J. Nanoparticle Res.*, vol. 13, no. 10, pp. 4717–4729, 2011.

[49] J. P. Vogel and R. R. Isberg, "Cell biology of Legionella pneumophila," *Curr. Opin. Microbiol.*, vol. 2, no. 1, pp. 30–34, 1999.

[50] M. Bloemen, C. Denis, M. Peeters, L. De Meester, A. Gils, N. Geukens, and T. Verbiest, "Antibody-modified iron oxide nanoparticles for efficient

magnetic isolation and flow cytometric determination of L. pneumophila," *Microchim. Acta*, vol. 182, no. 7–8, pp. 1439–1446, 2015.

[51] G. Van Loo, X. Saelens, and M. V. G. M. Macfarlane, "The role of mitochondrial factors in apoptosis : a Russian roulette with more than one bullet," *Cell Death Differ.*, vol. 9, pp. 1031–1042, 2002.

[52] T. T. Luong, S. Knoppe, M. Bloemen, W. Brullot, R. Strobbe, J. Locquet, and T. Verbiest, "Magnetothermal release of payload from iron oxide / silica drug delivery Agents," *J. Magn. Magn. Mater.*, vol. 416, no. 15, pp. 194–199, 2016.

[53] A. Wang and S. Li, "Hydroxycamptothecin-loaded nanoparticles enhance target drug delivery and anticancer effect," vol. 7, pp. 1–7, 2008.

[54] S. Li, A. Wang, W. Jiang, and Z. Guan, "Pharmacokinetic characteristics and anticancer effects of 5-Fluorouracil loaded nanoparticles," *BMC Cancer*, vol. 8, p. 103 (9pp), 2008.

[55] H.-Y. Hwang, I.-S. Kim, I. C. Kwon, and Y.-H. Kim, "Tumor targetability and antitumor effect of docetaxel-loaded hydrophobically modified glycol chitosan nanoparticles," *J. Control. Release*, vol. 128, no. 1, pp. 23–31, 2008.

[56] C. R. Patra, R. Bhattacharya, E. Wang, A. Katarya, J. S. Lau, S. Dutta, M. Muders, S. Wang, S. A. Buhrow, S. L. Safgren, M. J. Yaszemski, J. M. Reid, M. M. Ames, P. Mukherjee, and D. Mukhopadhyay, "Targeted Delivery of Gemcitabine to Pancreatic Adenocarcinoma Using Cetuximab as a Targeting Agent," *Cancer Res.*, vol. 68, no. 6, pp. 1970–1978, 2008.

[57] I. I. Slowing, B. G. Trewyn, S. Giri, and V. S.-Y. Lin, "Mesoporous Silica Nanoparticles for Drug Delivery and Biosensing Applications," *Adv. Funct. Mater.*, vol. 17, no. 8, pp. 1225–1236, 2007.

[58] S. S. Kelkar and T. M. Reineke, "Theranostics: Combining Imaging and Therapy," *Bioconjug. Chem.*, vol. 22, no. 10, pp. 1879–1903, 2011.

[59] J. T. Cole and N. B. Holland, "Multifunctional nanoparticles for use in theranostic applications," *Drug Deliv. Transl. Res.*, vol. 5, no. 3, pp. 295–309, 2015.

[60] J. Stöhr and H. C. Siegmann, *Magnetism From Fundamentals to Nanoscale Dynamics*. Springer-Verlag Berlin Heidelberg, 2006.

[61] B. Ward, “Development , synthesis and characterization of multifunctional nanomaterials,” KU Leuven, 2014.

[62] A.-H. Lu, E. L. Salabas, and F. Schüth, “Magnetic Nanoparticles: Synthesis, Protection, Functionalization, and Application,” *Angew. Chemie Int. Ed.*, vol. 46, no. 8, pp. 1222–1244, 2007.

[63] W. Brullot, N. K. Reddy, J. Wouters, V. K. Valev, B. Goderis, J. Vermant, and T. Verbiest, “Versatile ferrofluids based on polyethylene glycol coated iron oxide nanoparticles,” *J. Magn. Magn. Mater.*, vol. 324, no. 11, pp. 1919–1925, 2012.

[64] J. Estelrich, E. Escribano, J. Queralt, and M. Busquets, “Iron Oxide Nanoparticles for Magnetically-Guided and Magnetically-Responsive Drug Delivery,” *Int. J. Mol. Sci.*, vol. 16, no. 4, pp. 8070–8101, 2015.

[65] S. Laurent, D. Forge, M. Port, A. Roch, C. Robic, L. Vander Elst, and R. N. Muller, “Magnetic Iron Oxide Nanoparticles: Synthesis, Stabilization, Vectorization, Physicochemical Characterizations, and Biological Applications,” *Chem. Rev.*, vol. 108, no. 6, pp. 2064–2110, 2008.

[66] H. K. Sajja, M. P. East, H. Mao, andrew Y. Wang, S. Nie, L. Yang, Y. A. Wang, S. Nie, L. Yang, andrew Y. Wang, S. Nie, and L. Yang, “Development of Multifunctional Nanopaticles for Targeted Drug Delivery and Non-invasive Imaging of Therapeutic Effect,” *Curr. drug Discov. Technol.*, vol. 6, no. 1, pp. 43–51, 2009.

[67] M. Bloemen, C. Denis, M. Peeters, and L. De Meester, “Antibody-modified iron oxide nanoparticles for efficient magnetic isolation and flow cytometric determination of L . pneumophila,” *Microchim. Acta*, vol. 182, no. 7–8, pp. 1439–1446, 2015.

[68] H. Chen, M. C. Roco, X. Li, and Y. Lin, “Trends in nanotechnology patents,” *Nat Nano*, vol. 3, no. 3, pp. 123–125, 2008.

[69] W. Brullot, “Synthesis and Characterization of Stable ferrofluids,” University of Leuven, 2009.

[70] B. Issa, I. M. Obaidat, B. A. Albiss, and Y. Haik, “Magnetic Nanoparticles : Surface Effects and Properties Related to Biomedicine Applications,” *Int. J. Mol. Sci.*, vol. 14, pp. 21266–21305, 2013.

[71] M. Houshiar, F. Zebhi, Z. J. Razi, A. Alidoust, and Z. Askari, “Synthesis of cobalt ferrite (CoFe2O4) nanoparticles using combustion, coprecipitation, and precipitation methods: A comparison study of size,

structural, and magnetic properties," *J. Magn. Magn. Mater.*, vol. 371, pp. 43–48, 2014.

[72] R. M. Cornell and U. Schwertmann, "Crystal Structure," in *The Iron Oxides*, Wiley-VCH Verlag GmbH & Co. KGaA, 2003, pp. 9–38.

[73] M. A. Willard, L. K. Kurihara, E. E. Carpenter, S. Calvin, and V. G. Harris, "Chemically prepared magnetic nanoparticles," *Int. Mater. Rev.*, vol. 49, no. 3–4, pp. 125–170, Jun. 2004.

[74] J.-P. Jolivet, C. Chaneac, and E. Tronc, "Iron oxide chemistry. From molecular clusters to extended solid networks," *Chem. Commun.*, no. 5, pp. 481–483, 2004.

[75] M. Bloemen, W. Brullot, T. T. Luong, N. Geukens, A. Gils, and T. Verbiest, "Improved functionalization of oleic acid-coated iron oxide nanoparticles for biomedical applications.," *J. Nanopart. Res.*, vol. 14, no. 9, pp. 1100–1109, 2012.

[76] J.-G. J. J.-H. Park, K. An, Y. Hwang, J.-G. J. J.-H. Park, H.-J. Noh, J.-Y. Kim, J.-G. J. J.-H. Park, N.-M. Hwang, and T. Hyeon, "Ultra-large-scale syntheses of monodisperse nanocrystals," *Nat. Mater.*, vol. 3, no. 12, pp. 891–895, 2004.

[77] V. Yathindranath, L. Rebbouh, D. F. Moore, D. W. Miller, J. Van Lierop, and T. Hegmann, "A versatile method for the reductive, one-pot synthesis of bare, hydrophilic and hydrophobic magnetite nanoparticles," *Adv. Funct. Mater.*, vol. 21, pp. 1457–1464, 2011.

[78] J. Park, E. Lee, N.-M. Hwang, M. Kang, S. C. Kim, Y. Hwang, J.-G. Park, H.-J. Noh, J.-Y. Kim, J.-H. Park, and T. Hyeon, "One-Nanometer-Scale Size-Controlled Synthesis of Monodisperse Magnetic Iron Oxide Nanoparticles," *Angew. Chemie Int. Ed.*, vol. 44, no. 19, pp. 2872–2877, 2005.

[79] J. Park, K. An, Y. Hwang, J. Park, J. I. N. Noh, J. A. E. Y. Kim, J. Park, and N. Hwang, "Ultra-large scale syntheses of monodisperse nanocrystals via a simple and inexpensive route," *Nature*, vol. 3, no. 12, pp. 1–13, 2004.

[80] N. T. K. Thanh, N. Maclean, and S. Mahiddine, "Mechanisms of Nucleation and Growth of Nanoparticles in Solution," *Chem. Rev.*, vol. 114, no. 15, pp. 7610–7630, 2014.

[81] N. Perez, F. Lopez-Calahorra, A. Labarta, and X. Batlle, "Reduction of iron by decarboxylation in the formation of magnetite nanoparticles," *Phys. Chem. Chem. Phys.*, vol. 13, no. 43, pp. 19485–19489, 2011.

[82] W. Cai and J. Wan, "Facile synthesis of superparamagnetic magnetite nanoparticles in liquid polyols," *J. Colloid Interface Sci.*, vol. 305, no. 2, pp. 366–370, 2007.

[83] J. K. Lim, S. A. Majetich, and R. D. Tilton, "Stabilization of Superparamagnetic Iron Oxide Core-Gold Shell Nanoparticles in High Ionic Strength Media," *Langmuir*, vol. 25, no. 23, pp. 13384–13393, 2009.

[84] S. Laurent, S. Dutz, U. O. Häfeli, and M. Mahmoudi, "Magnetic fluid hyperthermia: Focus on superparamagnetic iron oxide nanoparticles," *Adv. Colloid Interface Sci.*, vol. 166, no. 1–2, pp. 8–23, 2011.

[85] E. D. Smolensky, H.-Y. E. Park, T. S. Berquó, and V. C. Pierre, "Surface functionalization of magnetic iron oxide nanoparticles for MRI applications - effect of anchoring group and ligand exchange protocol," *Contrast Media Mol. Imaging*, vol. 6, pp. 189–199, 2010.

[86] Y. Sahoo, A. Goodarzi, M. T. Swihart, T. Y. Ohulchanskyy, N. Kaur, E. P. Furlani, and P. N. Prasad, "Aqueous ferrofluid of magnetite nanoparticles: Fluorescence labeling and magnetophoretic control.," *J. Phys. Chem. B*, vol. 109, no. 9, pp. 3879–85, 2005.

[87] Y. Liu, Z. Chen, N. Gu, and J. Wang, "Effects of DMSA-coated Fe3O4 magnetic nanoparticles on global gene expression of mouse macrophage RAW264.7 cells," *Toxicol. Lett.*, vol. 205, no. 2, pp. 130–139, 2011.

[88] Z. P. Chen, Y. Zhang, S. Zhang, J. G. Xia, J. W. Liu, K. Xu, and N. Gu, "Preparation and characterization of water-soluble monodisperse magnetic iron oxide nanoparticles via surface double-exchange with DMSA," *Colloids Surfaces A Physicochem. Eng. Asp.*, vol. 316, no. 1–3, pp. 210–216, 2008.

[89] Y. Sahoo, H. Pizem, T. Fried, D. Golodnitsky, L. Burstein, C. N. Sukenik, and G. Markovich, "Alkyl Phosphonate / Phosphate Coating on Magnetite Nanoparticles : A Comparison with Fatty Acids Alkyl Phosphonate / Phosphate Coating on Magnetite Nanoparticles : A Comparison with Fatty Acids," *Langmuir*, vol. 17, no. 23, pp. 7907–7911, 2001.

[90] C. Tudisco, V. Oliveri, M. Cantarella, G. Vecchio, and G. G. Condorelli, "Cyclodextrin anchoring on magnetic Fe3O4 nanoparticles modified with

phosphonic linkers," *Eur. J. Inorg. Chem.*, vol. 2012, no. 32, pp. 5323–5331, 2012.

[91] S. Mohapatra and P. Pramanik, "Synthesis and stability of functionalized iron oxide nanoparticles using organophosphorus coupling agents," *Colloids Surfaces A Physicochem. Eng. Asp.*, vol. 339, pp. 35–42, 2009.

[92] C. Xu, K. Xu, H. Gu, R. Zheng, H. Liu, X. Zhang, Z. Guo, and B. Xu, "Dopamine as a robust anchor to immobilize functional molecules on the iron oxide shell of magnetic nanoparticles," *J. Am. Chem. Soc.*, vol. 126, no. 32, pp. 9938–9939, 2004.

[93] S. F. Chin, K. S. Iyer, and C. L. Raston, "Facile and Green Approach To Fabricate Gold and Silver Coated Superparamagnetic Nanoparticles," *Cryst. Growth Des.*, vol. 9, no. 6, pp. 2685–2689, 2009.

[94] D. K. Nagesha, B. D. Plouffe, M. Phan, L. H. Lewis, S. Sridhar, and S. K. Murthy, "Functionalization-induced improvement in magnetic properties of Fe3O4 nanoparticles for biomedical applications," *J. Appl. Phys.*, vol. 105, no. 7, pp. 07B317(1–3), 2009.

[95] I. J. Bruce and T. Sen, "Surface modification of magnetic nanoparticles with alkoxysilanes and their application in magnetic bioseparations," *Langmuir*, vol. 21, no. 15, pp. 7029–7035, 2005.

[96] W. J. Rieter, J. S. Kim, K. M. L. Taylor, H. An, W. Lin, T. Tarrant, and W. Lin, "Hybrid Silica Nanoparticles for Multimodal Imaging," *Angew. Chemie Int. Ed.*, vol. 46, no. 20, pp. 3680–3682, 2007.

[97] J. Park, J. Joo, S. G. Kwon, Y. Jang, and T. Hyeon, "Synthese monodisperser sphärischer Nanokristalle," *Angew. Chemie*, vol. 119, no. 25, pp. 4714–4745, 2007.

[98] N. Ž. Knežević, I. I. Slowing, and V. S.-Y. Lin, "Tuning the Release of Anticancer Drugs from Magnetic Iron Oxide/Mesoporous Silica Core/Shell Nanoparticles," *Chempluschem*, vol. 77, no. 1, pp. 48–55, 2012.

[99] N. Z. Knezevic and V. S. Y. Lin, "A magnetic mesoporous silica nanoparticle-based drug delivery system for photosensitive cooperative treatment of cancer with a mesopore-capping agent and mesopore-loaded drug," *Nanoscale*, vol. 5, no. 4, pp. 1544–1551, 2013.

[100] B. E. Brinson, J. B. Lassiter, C. S. Levin, R. Bardhan, N. Mirin, and N. J. Halas, "Nanoshells made easy: improving Au layer growth on nanoparticle surfaces," *Langmuir*, vol. 24, no. 24, pp. 14166–14171, 2008.

[101] C. S. Levin, C. Hofmann, T. A. Ali, A. T. Kelly, E. Morosan, P. Nordlander, K. H. Whitmire, and N. J. Halas, "Magnetic−Plasmonic Core−Shell Nanoparticles," *ACS Nano*, vol. 3, no. 6, pp. 1379–1388, 2009.

[102] K. C.-F. Leung, S. Xuan, X. Zhu, D. Wang, C.-P. Chak, S.-F. Lee, W. K.-W. Ho, and B. C.-T. Chung, "Gold and iron oxide hybrid nanocomposite materials," *Chem. Soc. Rev.*, vol. 41, no. 5, pp. 1911–1928, 2012.

[103] W. Stöber, A. Fink, and E. Bohn, "Controlled growth of monodisperse silica spheres in the micron size range," *J. Colloid Interface Sci.*, vol. 26, no. 1, pp. 62–69, 1968.

[104] K. Suzuki, K. Ikari, and H. Imai, "Synthesis of Silica Nanoparticles Having a Well-Ordered Mesostructure Using a Double Surfactant System," *J. Am. Chem. Soc.*, vol. 126, no. 2, pp. 462–463, 2004.

[105] K. M. L. Taylor, J. S. Kim, W. J. Rieter, H. An, W. Lin, and W. Lin, "Mesoporous silica nanospheres as highly efficient MRI contrast agents," *J. Am. Chem. Soc.*, vol. 130, no. 7, pp. 2154–2155, 2008.

[106] A. B. D. Nandiyanto, S.-G. Kim, F. Iskandar, and K. Okuyama, "Synthesis of spherical mesoporous silica nanoparticles with nanometer-size controllable pores and outer diameters," *Microporous Mesoporous Mater.*, vol. 120, no. 3, pp. 447–453, 2009.

[107] A. Katiyar, S. Yadav, P. G. Smirniotis, and N. G. Pinto, "Synthesis of ordered large pore SBA-15 spherical particles for adsorption of biomolecules," *J. Chromatogr. A*, vol. 1122, no. 1–2, pp. 13–20, 2006.

[108] D. Zhao, J. Feng, Q. Huo, N. Melosh, G. H. Fredrickson, B. F. Chmelka, and G. D. Stucky, "Triblock Copolymer Syntheses of Mesoporous Silica with Periodic 50 to 300 Angstrom Pores," *Science (80-.).*, vol. 279, no. 5350, pp. 548–552, 1998.

[109] B. G. Trewyn, J. A. Nieweg, Y. Zhao, and V. S.-Y. Lin, "Biocompatible mesoporous silica nanoparticles with different morphologies for animal cell membrane penetration," *Chem. Eng. J.*, vol. 137, no. 1, pp. 23–29, 2008.

[110] R. Mellaerts, C. A. Aerts, J. Van Humbeeck, P. Augustijns, G. Van den Mooter, and J. A. Martens, "Enhanced release of itraconazole from ordered mesoporous SBA-15 silica materials," *Chem. Commun.*, no. 13, pp. 1375–1377, 2007.

[111] T. Heikkilä, J. Salonen, J. Tuura, M. S. Hamdy, G. Mul, N. Kumar, T. Salmi, D. Y. Murzin, L. Laitinen, A. M. Kaukonen, J. Hirvonen, and V.-P. Lehto, "Mesoporous silica material TUD-1 as a drug delivery system," *Int. J. Pharm.*, vol. 331, no. 1, pp. 133–138, 2007.

[112] Y. Tozuka, A. Wongmekiat, K. Kimura, K. Moribe, S. Yamamura, and K. Yamamoto, "Effect of Pore Size of FSM-16 on the Entrapment of Flurbiprofen in Mesoporous Structures," *Chem. Pharm. Bull.*, vol. 53, no. 8, pp. 974–977, 2005.

[113] R. Mellaerts, R. Mols, P. Kayaert, P. Annaert, J. Van Humbeeck, G. Van den Mooter, J. A. Martens, and P. Augustijns, "Ordered mesoporous silica induces pH-independent supersaturation of the basic low solubility compound itraconazole resulting in enhanced transepithelial transport," *Int. J. Pharm.*, vol. 357, no. 1–2, pp. 169–179, 2008.

[114] R. Mellaerts, R. Mols, J. A. G. Jammaer, C. A. Aerts, P. Annaert, J. Van Humbeeck, G. Van den Mooter, P. Augustijns, and J. A. Martens, "Increasing the oral bioavailability of the poorly water soluble drug itraconazole with ordered mesoporous silica," *Eur. J. Pharm. Biopharm.*, vol. 69, no. 1, pp. 223–230, 2008.

[115] B. Vincent, J. Edwards, S. Emmett, and A. Jones, "Depletion flocculation in dispersions of sterically-stabilised particles ('soft spheres')," *Colloids and Surfaces*, vol. 18, no. 2, pp. 261–281, 1986.

[116] G. Fritz, V. Schädler, N. Willenbacher, and N. J. Wagner, "Electrosteric Stabilization of Colloidal Dispersions," *Langmuir*, vol. 18, no. 16, pp. 6381–6390, 2002.

[117] D. H. Napper, "Flocculation studies of sterically stabilized dispersions," *J. Colloid Interface Sci.*, vol. 32, no. 1, pp. 106–114, 1970.

[118] M. Kobayashi, M. Skarba, P. Galletto, D. Cakara, and M. Borkovec, "Effects of heat treatment on the aggregation and charging of Stöber-type silica," *J. Colloid Interface Sci.*, vol. 292, no. 1, pp. 139–147, 2005.

[119] R. Xu, *Particle Characterization: Light Scattering Methods*. Kluwer Academic Publishers, 2001.

[120] C. J. Murphy, A. M. Gole, S. E. Hunyadi, J. W. Stone, P. N. Sisco, A. Alkilany, B. E. Kinard, and P. Hankins, "Chemical sensing and imaging with metallic nanorods," *Chem. Commun.*, no. 5, pp. 544–557, 2008.

[121] X. Huang and M. A. El-Sayed, "Gold nanoparticles: Optical properties and implementations in cancer diagnosis and photothermal therapy," *J. Adv. Res.*, vol. 1, no. 1, pp. 13–28, 2010.

[122] G. Mie, "Beiträge zur Optik trüber Medien, speziell kolloidaler Metallösungen," *Ann. Phys.*, vol. 330, no. 3, pp. 377–445, 1908.

[123] G. C. Papavassiliou, "Optical properties of small inorganic and organic metal particles," *Prog. Solid State Chem.*, vol. 12, no. 3, pp. 185–271, 1979.

[124] A. J. Haes, D. A. Stuart, S. Nie, and R. P. Van Duyne, "Using Solution-Phase Nanoparticles , Surface-Confined Nanoparticle Arrays and Single Nanoparticles as Biological Sensing Platforms," *J. Fluoresc.*, vol. 14, no. 4, pp. 355–367, 2004.

[125] M. Faraday, "The Bakerian Lecture: Experimental Relations of Gold (and Other Metals) to Light," *Philos. Trans. R. Soc. London*, vol. 147, pp. 145–181, 1857.

[126] J. A. Creighton and D. G. Eadon, "Ultraviolet-visible absorption spectra of the colloidal metallic elements," *J. Chem. Soc. Faraday Trans.*, vol. 87, no. 24, pp. 3881–3891, 1991.

[127] S. Link and M. A. El-Sayed, "Size and Temperature Dependence of the Plasmon Absorption of Colloidal Gold Nanoparticles," *J. Phys. Chem. B*, vol. 103, no. 21, pp. 4212–4217, May 1999.

[128] "Notre Dame de Paris." [Online]. Available: https://en.wikipedia.org/wiki/Notre_Dame_de_Paris. [Accessed: 11-Aug-2016].

[129] M. Hu, J. Chen, Z. Li, L. Au, G. V Hartland, X. Li, M. Marquez, and Y. Xia, "Gold nanostructures : engineering their plasmonic properties for biomedical applications," *Chem. Soc. Rev.*, vol. 35, pp. 1084–1094, 2006.

[130] A. C. Templeton, J. J. Pietron, R. W. Murray, P. Mulvaney, K. Laboratories, V. Uni, C. Hill, and N. Carolina, "Solvent Refractive Index and Core Charge Influences on the Surface Plasmon Absorbance of Alkanethiolate Monolayer-Protected Gold Clusters," *J. Phys. Chem. B*, vol. 104, no. 3, pp. 564–570, 2000.

[131] A. J. Haes, S. Zou, G. C. Schatz, and R. P. Van Duyne, "A Nanoscale Optical Biosensor: The Long Range Distance Dependence of the Localized Surface Plasmon Resonance of Noble Metal Nanoparticles," *J. Phys. Chem. B*, vol. 108, no. 1, pp. 109–116, Jan. 2004.

[132] E. Hutter and J. H. Fendler, "Exploitation of Localized Surface Plasmon Resonance," *Adv. Mater.*, vol. 16, no. 19, pp. 1685–1706, 2004.

[133] M. J. Hostetler, J. E. Wingate, C. Zhong, J. E. Harris, R. W. Vachet, M. R. Clark, J. D. Londono, S. J. Green, J. J. Stokes, G. D. Wignall, G. L. Glish, M. D. Porter, N. D. Evans, and R. W. Murray, "Alkanethiolate Gold Cluster Molecules with Core Diameters from 1.5 to 5.2 nm: Core and Monolayer Properties as a Function of Core Size," *Langmuir*, vol. 14, no. 1, pp. 17–30, 1998.

[134] J. R. Cole, N. A. Mirin, M. W. Knight, G. P. Goodrich, and N. J. Halas, "Photothermal Efficiencies of Nanoshells and Nanorods for Clinical Therapeutic Applications," *J. Phys. Chem. C*, vol. 113, no. 28, pp. 12090–12094, 2009.

[135] S. E. Skrabalak, J. Chen, Y. Sun, X. Lu, L. Au, C. M. Cobley, and Y. Xia, "Gold Nanocages: Synthesis, Properties, and Applications," *Acc. Chem. Res.*, vol. 41, no. 12, pp. 1587–1595, Dec. 2008.

[136] H. Wang, D. W. Brandl, F. Le, P. Nordlander, and N. J. Halas, "Nanorice: A hybrid plasmonic nanostructure," *Nano Lett.*, vol. 6, no. 4, pp. 827–832, 2006.

[137] S. Van Cleuvenbergen, "Octopolar materials for second-order nonlinear optic," KU Leuven, 2012.

[138] H. H. Yang, S. Q. Zhang, X. L. Chen, Z. X. Zhuang, J. G. Xu, and X. R. Wang, "Magnetite-Containing Spherical Silica Nanoparticles for Biocatalysis and Bioseparations," *Anal. Chem.*, vol. 76, no. 5, pp. 1316–1321, 2004.

[139] J. P. Chen and D. R. Su, "Latex particles with thermo-flocculation and magnetic properties for immobilization of ??-chymotrypsin," *Biotechnol. Prog.*, vol. 17, no. 2, pp. 369–375, 2001.

[140] H. Yu, J. W. Raymonda, T. M. McMahon, and A. A. Campagnari, "Detection of biological threat agents by immunomagnetic microsphere-based solid phase fluorogenic- and electro-chemiluminescence," *Biosens. Bioelectron.*, vol. 14, pp. 829–840, 2000.

[141] X.-D. Tong, B. Xue, and Y. Sun, "A novel magnetic affinity support for protein adsorption and purification.," *Biotechnol. Prog.*, vol. 17, no. 1, pp. 134–139, 2001.

[142] E. Paleček, R. Kizek, L. Havran, S. Billova, and M. Fojta, "Electrochemical enzyme-linked immunoassay in a DNA hybridization sensor," *Anal. Chim. Acta*, vol. 469, pp. 73–83, 2002.

[143] S. Nayar, A. Mir, A. Ashok, A. Guha, and V. Sharma, "Bovine Serum Albumin Binding and Drug Delivery Studies with PVA-Ferrofluid," *J. Bionic Eng.*, vol. 7, no. 1, pp. 29–34, 2010.

[144] E. H. Kim, H. S. Lee, B. K. Kwak, and B.-K. Kim, "Synthesis of ferrofluid with magnetic nanoparticles by sonochemical method for MRI contrast agent," *J. Magn. Magn. Mater.*, vol. 289, pp. 328–330, 2005.

[145] N. A. Brusentsov, L. V Nikitin, T. N. Brusentsova, A. A. Kuznetsov, F. S. Bayburtskiy, L. I. Shumakov, and N. Y. Jurchenko, "Magnetic fluid hyperthermia of the mouse experimental tumor," *J. Magn. Magn. Mater.*, vol. 252, pp. 378–380, 2002.

[146] T. T. Luong, T. P. Ha, L. D. Tran, M. H. Do, T. T. Mai, N. H. Pham, H. B. T. Phan, G. H. T. Pham, N. M. T. Hoang, Q. T. Nguyen, and P. X. Nguyen, "Design of carboxylated Fe3O4/poly(styrene-co-acrylic acid) ferrofluids with highly efficient magnetic heating effect," *Colloids Surfaces A Physicochem. Eng. Asp.*, vol. 384, no. 1–3, pp. 23–30, 2011.

[147] C. Barrera, A. P. Herrera, and C. Rinaldi, "Colloidal dispersions of monodisperse magnetite nanoparticles modified with poly(ethylene glycol)," *J. Colloid Interface Sci.*, vol. 329, no. 1, pp. 107–113, 2009.

[148] S. Liang, Y. Wang, C. Zhang, and X. Liu, "Synthesis of amino-modified magnetite nanoparticles coated with Hepama-1 and radiolabeled with 188Re for bio-magnetically targeted radiotherapy," *J. Radioanal. Nucl. Chem.*, vol. 269, no. 1, pp. 3–7, 2006.

[149] B. Pan, F. Gao, and H. Gu, "Dendrimer modified magnetite nanoparticles for protein immobilization," *J. Colloid Interface Sci.*, vol. 284, no. 1, pp. 1–6, 2005.

[150] D. Dupont, W. Brullot, M. Bloemen, T. Verbiest, and K. Binnemans, "Selective uptake of rare earths from aqueous solutions by EDTA-functionalized magnetic and nonmagnetic nanoparticles.," *ACS Appl. Mater. Interfaces*, vol. 6, no. 7, pp. 4980–8, 2014.

[151] H. Xu, Z. P. Aguilar, L. Yang, M. Kuang, H. Duan, Y. Xiong, H. Wei, and A. Wang, "Antibody conjugated magnetic iron oxide nanoparticles for cancer cell separation in fresh whole blood," *Biomaterials*, vol. 32, no. 36, pp. 9758–9765, 2011.

[152] M. J. E. Fischer, "Amine Coupling Through EDC/NHS: A Practical Approach," in *Surface Plasmon Resonance: Methods and Protocols*, J. N. Mol and E. M. J. Fischer, Eds. Totowa, NJ: Humana Press, 2010, pp. 55–73.

[153] M. Bradford, "A Rapid and Sensitive Method for the Quantitation of Microgram Quantities of Protein Utilizing the Principle of Protein-Dye Binding," *Anal. Biochem.*, vol. 254, pp. 248–254, 1976.

[154] S. J. Compton and C. G. Jones, "Mechanism of dye response and interference in the Bradford protein assay.," *Anal. Biochem.*, vol. 151, no. 2, pp. 369–374, 1985.

[155] I. Nedkov, T. Merodiiska, L. Slavov, R. E. Vandenberghe, Y. Kusano, and J. Takada, "Surface oxidation, size and shape of nano-sized magnetite obtained by co-precipitation," *J. Magn. Magn. Mater.*, vol. 300, no. 2, pp. 358–367, 2006.

[156] B. D. Cullity and C. D. Graham, *Introduction to Magnetic Materials*, Second edi. John Wiley And Sons Ltd, 2008.

[157] C. D. Georgiou, K. Grintzalis, G. Zervoudakis, and I. Papapostolou, "Mechanism of Coomassie brilliant blue G-250 binding to proteins: a hydrophobic assay for nanogram quantities of proteins," *Anal. Bioanal. Chem.*, vol. 391, no. 1, pp. 391–403, 2008.

[158] M. Gonzales-Weimuller, M. Zeisberger, and K. M. Krishnan, "Size-dependant heating rates of iron oxide nanoparticles for magnetic fluid hyperthermia," *J. Magn. Magn. Mater.*, vol. 321, no. 13, pp. 1947–1950, 2009.

[159] A. Tomitaka, K. Ueda, T. Yamada, and Y. Takemura, "Heat dissipation and magnetic properties of surface-coated Fe3O4 nanoparticles for biomedical applications," *J. Magn. Magn. Mater.*, vol. 324, no. 21, pp. 3437–3442, 2012.

[160] S.-H. H. Hu, T.-Y. Y. Liu, H.-Y. Y. Huang, D.-M. M. Liu, and S.-Y. Y. Chen, "Magnetic-Sensitive Silica Nanospheres for Controlled Drug Release," *Langmuir*, vol. 24, no. 1, pp. 239–244, 2008.

[161] J. E. Lee, N. Lee, H. Kim, J. Kim, S. H. Choi, J. H. Kim, T. Kim, I. C. Song, and S. P. Park, "Uniform Mesoporous Dye-Doped Silica Nanoparticles Decorated with Multiple Magnetite Nanocrystals for Simultaneous Enhanced Magnetic Resonance Imaging , Fluorescence Imaging , and Drug Delivery," pp. 552–557, 2010.

[162] D. L. Tran, V. H. Le, H. L. Pham, T. M. N. Hoang, T. Q. Nguyen, T. T. Luong, P. T. Ha, and X. P. Nguyen, "Biomedical and environmental applications of magnetic nanoparticles," *Adv. Nat. Sci. Nanosci. Nanotechnol.*, vol. 1, no. 4, p. 045013 (5pp), 2010.

[163] Z. Liao, H. Wang, R. Lv, P. Zhao, X. Sun, S. Wang, W. Su, R. Niu, and J. Chang, "Polymeric liposomes-coated superparamagnetic iron oxide nanoparticles as contrast agent for targeted magnetic resonance imaging of cancer cells," *Langmuir*, vol. 27, no. 6, pp. 3100–3105, 2011.

[164] J. Croissant and J. I. Zink, "Nanovalve-controlled cargo release activated by plasmonic heating," *J. Am. Chem. Soc.*, vol. 134, no. 18, pp. 7628–7631, 2012.

[165] E. Boisselier and D. Astruc, "Gold nanoparticles in nanomedicine: preparations, imaging, diagnostics, therapies and toxicity," *Chem. Soc. Rev.*, vol. 38, no. 6, p. 1759, 2009.

[166] C. Loo, A. Lowery, N. J. Halas, J. West, and R. Drezek, "Immunotargeted nanoshells for integrated cancer imaging and therapy.," *Nano Lett.*, vol. 5, no. 4, pp. 709–11, 2005.

[167] S. Bhattacharyya, R. A. Kudgus, R. Bhattacharya, and P. Mukherjee, "Inorganic nanoparticles in cancer therapy," *Pharm. Res.*, vol. 28, no. 2, pp. 237–259, 2011.

[168] L. R. Hirsch, J. B. Jackson, A. Lee, N. J. Halas, and J. L. West, "A whole blood immunoassay using gold nanoshells," *Anal. Chem.*, vol. 75, no. 10, pp. 2377–2381, 2003.

[169] M. C. Daniel and D. Astruc, "Gold Nanoparticles: Assembly, Supramolecular Chemistry, Quantum-Size-Related Properties, and Applications Toward Biology, Catalysis, and Nanotechnology," *Chem. Rev.*, vol. 104, no. 1, pp. 293–346, 2004.

[170] T. A. Larson, J. Bankson, J. Aaron, and K. Sokolov, "Hybrid plasmonic magnetic nanoparticles as molecular specific agents for MRI/optical

imaging and photothermal therapy of cancer cells," *Nanotechnology*, vol. 18, no. 32, p. 325101 (8pp), 2007.

[171] S. Y. Han, Q. H. Guo, M. M. Xu, Y. X. Yuan, L. M. Shen, J. L. Yao, W. Liu, and R. A. Gu, "Tunable fabrication on iron oxide/Au/Ag nanostructures for surface enhanced Raman spectroscopy and magnetic enrichment," *J. Colloid Interface Sci.*, vol. 378, no. 1, pp. 51–57, 2012.

[172] J. Ye, P. Van Dorpe, W. Van Roy, K. Lodewijks, I. De Vlaminck, G. Maes, G. Borghs, P. Van Dorpe, W. Van Roy, K. Lodewijks, I. De Vlaminck, G. Maes, and G. Borghs, "Fabrication and Optical Properties of Gold Semishells," *J. Phys. Chem. C*, vol. 113, no. 8, pp. 3110–3115, 2009.

[173] W. Chen, N. Xu, L. Xu, L. Wang, Z. Li, W. Ma, Y. Zhu, C. Xu, and N. A. Kotov, "Multifunctional magnetoplasmonic nanoparticle assemblies for cancer therapy and diagnostics (Theranostics)," *Macromol. Rapid Commun.*, vol. 31, no. 2, pp. 228–236, Jan. 2010.

[174] S. I. Stoeva, F. Huo, J. S. Lee, and C. A. . Mirkin, "Three-layer composite magnetic nanoparticle probes for DNA," *J. Am. Chem. Soc.*, vol. 127, no. 44, pp. 15362–15363, 2005.

[175] C. Xu, J. Xie, D. Ho, C. Wang, N. Kohler, E. G. Walsh, J. R. Morgan, Y. E. Chin, and S. Sun, "Au–Fe3O4 Dumbbell Nanoparticles as Dual-Functional Probes," *Angew. Chemie Int. Ed.*, vol. 47, no. 1, pp. 173–176, 2008.

[176] W. Brullot, R. Strobbe, M. Bynens, M. Bloemen, P. J. Demeyer, W. Vanderlinden, S. De Feyter, V. K. Valev, and T. Verbiest, "Layer-by-Layer synthesis and tunable optical properties of hybrid magnetic-plasmonic nanocomposites using short bifunctional molecular linkers," *Mater. Lett.*, vol. 118, pp. 99–102, 2014.

[177] S. Xuan, Y.-X. J. Wang, J. C. Yu, and K. C.-F. Leung, "Preparation, Characterization, and Catalytic Activity of Core/Shell Fe 3 O 4 @Polyaniline@Au Nanocomposites," *Langmuir*, vol. 25, no. 19, pp. 11835–11843, 2009.

[178] Y. Jin, "Multifunctional compact hybrid Au nanoshells: A new generation of nanoplasmonic probes for biosensing, imaging, and controlled release," *Acc. Chem. Res.*, vol. 47, no. 1, pp. 138–148, 2014.

[179] G. Liang, S. Cai, P. Zhang, Y. Peng, H. Chen, S. Zhang, and J. Kong, "Magnetic relaxation switch and colorimetric detection of thrombin using

aptamer-functionalized gold-coated iron oxide nanoparticles," *Anal. Chim. Acta*, vol. 689, no. 2, pp. 243–249, 2011.

[180] J. Lim, R. D. Tilton, A. Eggeman, and S. A. Majetich, "Design and synthesis of plasmonic magnetic nanoparticles," *J. Magn. Magn. Mater.*, vol. 311, pp. 78–83, 2007.

[181] J. Kim, H. H. S. Kim, N. Lee, T. Kim, H. H. S. Kim, T. Yu, I. C. Song, W. K. Moon, and T. Hyeon, "Multifunctional Uniform Nanoparticles Composed of a Magnetite Nanocrystal Core and a Mesoporous Silica Shell for Magnetic Resonance and Fluorescence Imaging and for Drug Delivery," *Angew. Chemie Int. Ed.*, vol. 47, no. 44, pp. 8438–8441, 2008.

[182] D. Caruntu, B. L. Cushing, G. Caruntu, and C. J. O'Connor, "Attachment of gold nanograins onto colloidal magnetite nanocrystals," *Chem. Mater.*, vol. 17, no. 13, pp. 3398–3402, 2005.

[183] W. Brullot, V. K. Valev, and T. Verbiest, "Magnetic-plasmonic nanoparticles for the life sciences: Calculated optical properties of hybrid structures," *Nanomedicine Nanotechnology, Biol. Med.*, vol. 8, no. 5, pp. 559–568, 2012.

[184] L. Wang, J. Luo, M. M. Maye, Q. Fan, Q. Rendeng, M. H. Engelhard, C. Wang, Y. Lin, and C.-J. Zhong, "Iron oxide–gold core–shell nanoparticles and thin film assembly," *J. Mater. Chem.*, vol. 15, no. 18, p. 1821, 2005.

[185] L. Wang, J. Luo, Q. Fan, M. Suzuki, I. S. Suzuki, M. H. Engelhard, Y. Lin, N. Kim, J. Q. Wang, and C. Zhong, "Monodispersed Core-Shell Fe3O4@ Au Nanoparticles," *J. Phys. Chem. B*, pp. 21593–21601, 2005.

[186] A. M. Gobin, M. H. Lee, N. J. Halas, W. D. James, R. A. Drezek, and J. L. West, "Near-infrared resonant nanoshells for combined optical imaging and photothermal cancer therapy," *Nano Lett.*, vol. 7, no. 7, pp. 1929–1934, 2007.

[187] X. Ji, R. Shao, A. M. Elliott, R. Jason Stafford, E. Esparza-Coss, J. A. Bankson, G. Liang, Z. P. Luo, K. Park, J. T. Markert, and C. Li, "Bifunctional Gold Nanoshells with a Superparamagnetic Iron Oxide-Silica Core Suitable for Both MR Imaging and Photothermal Therapy," *J. Phys. Chem. C*, vol. 111, no. 17, pp. 6245–6251, 2007.

[188] W. G. Zijlstra and A. Buursma, "Spectrophotometry of Hemoglobin: Absorption Spectra of Bovine Oxyhemoglobin, Deoxyhemoglobin,

Carboxyhemoglobin, and Methemoglobin," *Comp. Biochem. Physiol.*, vol. 118B, no. 4, pp. 743–749, Dec. 1997.

[189] Q. H. Lu, K. L. Yao, D. Xi, Z. L. Liu, X. P. Luo, and Q. Ning, "Synthesis and characterization of composite nanoparticles comprised of gold shell and magnetic core/cores," *J. Magn. Magn. Mater.*, vol. 301, no. 1, pp. 44–49, 2006.

[190] T. T. Hien Pham, C. Cao, and S. J. Sim, "Application of citrate-stabilized gold-coated ferric oxide composite nanoparticles for biological separations," *J. Magn. Magn. Mater.*, vol. 320, no. 15, pp. 2049–2055, 2008.

[191] Y. Jin, C. Jia, S.-W. Huang, M. O'Donnell, and X. Gao, "Multifunctional nanoparticles as coupled contrast agents.," *Nat. Commun.*, vol. 1, no. 4, p. 41, 2010.

[192] W. Wu, Q. He, H. Chen, J. Tang, and L. Nie, "Sonochemical synthesis, structure and magnetic properties of air-stable Fe_3O_4 / Au nanoparticles," *Nanotechnology*, vol. 18, no. 14, p. 145609, 2007.

[193] D. G. Duff, A. Baiker, and P. P. Edwards, "A New Hydrosol of Gold Clusters. 1. Formation and Particle Size Variation," *Langmuir*, vol. 9, no. 16, pp. 2301–2309, 1993.

[194] S. L. Westcott, S. J. Oldenburg, T. R. Lee, and N. J. Halas, "Formation and Adsorption of Clusters of Gold Nanoparticles onto Functionalized Silica Nanoparticle Surfaces," *Langmuir*, vol. 14, no. 12, pp. 5396–5401, 1998.

[195] S. J. Oldenburg, R. D. Averitt, S. L. Westcott, and N. J. Halas, "Nanoengineering of optical resonances," *Chem. Phys. Lett.*, vol. 288, no. 2–4, pp. 243–247, 1998.

[196] M. Garcia, J. de la Venta, P. Crespo, J. LLopis, S. Penadés, A. Fernández, and A. Hernando, "Surface plasmon resonance of capped Au nanoparticles," *Phys. Rev. B*, vol. 72, no. 24, p. 241403(R), 2005.

[197] Sigma-Aldrich, "Gold Nanoparticles: Properties and Applications." [Online]. Available: http://www.sigmaaldrich.com/materials-science/nanomaterials/gold-nanoparticles.html. [Accessed: 15-Aug-2016].

[198] Cytodiagnostics, "Gold Nanoparticle Properties." [Online]. Available: http://www.cytodiagnostics.com/store/pc/Gold-Nanoparticle-Properties-d2.htm. [Accessed: 15-Aug-2016].

[199] M. Bloemen, D. Debruyne, P.-J. Demeyer, K. Clays, A. Gils, N. Geukens, C. Bartic, and T. Verbiest, "Catechols as ligands for CdSe–ZnS quantum dots," *RSC Adv.*, vol. 4, no. 20, pp. 10208–10211, 2014.

[200] A. Postma, Y. Yan, Y. Wang, A. N. Zelikin, E. Tjipto, and F. Caruso, "Self-Polymerization of Dopamine as a Versatile and Robust Technique to Prepare Polymer Capsules," *Chem. Mater.*, vol. 21, no. 8, pp. 3042–3044, 2009.

[201] W. Zheng, H. Fan, L. Wang, and Z. Jin, "Oxidative Self-Polymerization of Dopamine in an Acidic Environment," *Langmuir*, vol. 31, pp. 11671–11677, 2015.

[202] M. D'Ischia, A. Napolitano, A. Pezzella, P. Meredith, and T. Sarna, "Chemical and structural diversity in eumelanins: Unexplored bio-optoelectronic materials," *Angew. Chemie - Int. Ed.*, vol. 48, no. 22, pp. 3914–3921, 2009.

[203] K. C. Grabar, K. J. Allison, B. E. Baker, R. M. Bright, K. R. Brown, R. G. Freeman, A. P. Fox, C. D. Keating, M. D. Musick, and M. J. Natan, "Two-dimensional arrays of colloidal gold particles: A flexible approach to macroscopic metal surfaces," *Langmuir*, vol. 12, no. 10, pp. 2353–2361, 1996.

[204] M. R. Rasch, K. V. Sokolov, and B. A. Korgel, "Limitations on the Optical Tunability of Small Diameter Gold Nanoshells," *Langmuir*, vol. 25, no. 19, pp. 11777–11785, 2009.

[205] H. Cong, R. Toftegaard, J. Arnbjerg, and P. R. Ogilby, "Silica-coated gold nanorods with a gold overcoat: Controlling optical properties by controlling the dimensions of a gold-silica-gold layered nanoparticle," *Langmuir*, vol. 26, no. 6, pp. 4188–4195, 2010.

[206] Y. Wu, T. Zhang, Z. Zheng, X. Ding, and Y. Peng, "A facile approach to Fe3O4@Au nanoparticles with magnetic recyclable catalytic properties," *Mater. Res. Bull.*, vol. 45, no. 4, pp. 513–517, 2010.

[207] H. Yu, M. Chen, P. M. Rice, S. X. Wang, R. L. White, and S. Sun, "Dumbbell-like Bifunctional Au−Fe3O4 Nanoparticles," *Nano Lett.*, vol. 5, no. 2, pp. 379–382, 2005.

[208] G. Cheng and A. R. Hight Walker, "Synthesis and characterization of cobalt/gold bimetallic nanoparticles," *J. Magn. Magn. Mater.*, vol. 311, no. 1, pp. 31–35, 2007.

[209] C. D. Keating, M. D. Musick, M. H. Keefe, and M. J. Natan, "Kinetics and Thermodynamics of Au Colloid Monolayer Self-Assembly: Undergraduate Experiments in Surface and Nanomaterials Chemistry," *J. Chem. Educ.*, vol. 76, no. 7, pp. 949–955, 1999.

[210] J. Park, K. An, Y. Hwang, J.-G. Park, H.-J. Noh, J.-Y. Kim, J.-H. Park, N.-M. Hwang, and H. Taeghwan, "Ultra-large-scale syntheses of monodisperse nanocrystals," *Nat. Mater.*, vol. 3, no. 12, pp. 891–895, 2004.

[211] D. Shahbazi-gahrouei, M. Abdolahi, S. H. Zarkesh-esfahani, S. Laurent, C. Sermeus, and C. Gruettner, "Functionalized Magnetic Nanoparticles for the Detection and Quantitative Analysis of Cell Surface Antigen," *Biomed Res. Int.*, vol. 2013, pp. 1–9, 2013.

[212] S. Bedanta and W. Kleemann, "Supermagnetism," *J. Phys. D. Appl. Phys.*, vol. 42, no. 1, p. 013001, 2009.

[213] E. Mahon, A. Salvati, F. Baldelli Bombelli, I. Lynch, and K. A. Dawson, "Designing the nanoparticle-biomolecule interface for 'targeting and therapeutic delivery,'" *Journal of Controlled Release*, vol. 161, no. 2. pp. 164–174, 2012.

[214] L. Lartigue, C. Innocenti, T. Kalaivani, A. Awwad, M. D. M. Sanchez Duque, Y. Guari, J. Larionova, C. Gueírin, J. L. G. Montero, V. Barragan-Montero, P. Arosio, A. Lascialfari, D. Gatteschi, and C. Sangregorio, "Water-dispersible sugar-coated iron oxide nanoparticles. An evaluation of their relaxometric and magnetic hyperthermia properties," *J. Am. Chem. Soc.*, vol. 133, no. 27, pp. 10459–10472, 2011.

[215] M. E. F. Brollo, J. M. Orozco-Henao, R. López-Ruiz, D. Muraca, C. S. B. Dias, K. R. Pirota, and M. Knobel, "Magnetic hyperthermia in brick-like Ag@Fe3O4 core–shell nanoparticles," *J. Magn. Magn. Mater.*, vol. 397, pp. 20–27, Jan. 2016.

[216] A. E. Deatsch and B. A. Evans, "Heating efficiency in magnetic nanoparticle hyperthermia," *Journal of Magnetism and Magnetic Materials*, vol. 354. pp. 163–172, 2014.

[217] S. H. Hu, T. Y. Liu, H. Y. Huang, D. M. Liu, and S. Y. Chen, "Magnetic-sensitive silica nanospheres for controlled drug release," *Langmuir*, vol. 24, pp. 239–244, 2008.

[218] E. Bringas, Ö. Köysüren, D. V. Quach, M. Mahmoudi, E. Aznar, J. D. Roehling, M. D. Marcos, R. Martínez-Máñez, and P. Stroeve, "Triggered release in lipid bilayer-capped mesoporous silica nanoparticles containing SPION using an alternating magnetic field," *Chem. Commun.*, vol. 48, no. 45, pp. 5647–5649, 2012.

[219] P.-J. Chen, S.-H. Hu, C.-S. Hsiao, Y.-Y. Chen, D.-M. Liu, and S.-Y. Chen, "Multifunctional magnetically removable nanogated lids of Fe3O4–capped mesoporous silica nanoparticles for intracellular controlled release and MR imaging," *J. Mater. Chem.*, vol. 21, pp. 2535–2543, 2011.

[220] P. Nadrah, O. Planinšek, and M. Gaberšček, "Stimulus-responsive mesoporous silica particles," *J. Mater. Sci.*, vol. 49, no. 2, pp. 481–495, 2013.

[221] K. C. Souza, N. D. S. Mohallem, and E. M. B. Sousa, "Mesoporous silica-magnetite nanocomposite: Facile synthesis route for application in hyperthermia," *J. Sol-Gel Sci. Technol.*, vol. 53, no. 2, pp. 418–427, 2010.

[222] Y. S. Lin, S. H. Wu, Y. Hung, Y. H. Chou, C. Chang, M. L. Lin, C. P. Tsai, and C. Y. Mou, "Multifunctional composite nanoparticles: Magnetic, luminescent, and mesoporous," *Chem. Mater.*, vol. 18, no. 22, pp. 5170–5172, 2006.

[223] E. Yamamoto, M. Kitahara, T. Tsumura, and K. Kuroda, "Preparation of Size-Controlled Monodisperse Colloidal Mesoporous Silica Nanoparticles and Fabrication of Colloidal Crystals," *Chem. Mater.*, vol. 26, no. 9, pp. 2927–2933, May 2014.

[224] M. Vallet-Regí, F. Balas, and D. Arcos, "Mesoporous Materials for Drug Delivery," *Angew. Chemie Int. Ed.*, vol. 46, no. 40, pp. 7548–7558, 2007.

[225] J. Andersson, J. Rosenholm, S. Areva, and M. Lindén, "Influences of Material Characteristics on Ibuprofen Drug Loading and Release Profiles from Ordered Micro- and Mesoporous Silica Matrices," *Chem. Mater.*, vol. 16, no. 21, pp. 4160–4167, Oct. 2004.

[226] B. Srinivasan and X. Huang, "Functionalization of magnetic nanoparticles with organic molecules: Loading level determination and evaluation of linker length effect on immobilization," *Chirality*, vol. 20, no. 3–4, pp. 265–277, 2008.

[227] J. E. Lee, N. Lee, H. Kim, J. Kim, S. H. Choi, J. H. Kim, T. Kim, I. C. Song, S. P. Park, W. K. Moon, and T. Hyeon, "Uniform Mesoporous Dye-

Doped Silica Nanoparticles Decorated with Multiple Magnetite Nanocrystals for Simultaneous Enhanced Magnetic Resonance Imaging, Fluorescence Imaging, and Drug Delivery," *J. Am. Chem. Soc.*, vol. 132, no. 2, pp. 552–557, 2010.

[228] M. Bloemen, B. Sutens, W. Brullot, A. Gils, N. Geukens, and T. Verbiest, "Two-Step Directional Surface Modification of Iron Oxide Nanoparticles with Protected Siloxanes," *Chempluschem*, pp. 50–53, 2014.

[229] Y. A. Cengel, *Heat Transfer: A Practical Approach*, Second edi. New York: McGraw-Hill, 2002.

[230] R. T. Sanderson, *Chemical bonds and bond energy*, Second edi. New York: New York : Academic Press, 1976.

[231] N. Hao, H. Liu, L. Li, D. Chen, L. Li, and F. Tang, "<I>In Vitro</I> Degradation Behavior of Silica Nanoparticles Under Physiological Conditions," *J. Nanosci. Nanotechnol.*, vol. 12, no. 8, pp. 6346–6354, 2012.

[232] G. Gu, P. P. Ong, and C. Chu, "Thermal stability of mesoporous silica molecular sieve," *Journal of Physics and Chemistry of Solids*, vol. 60, no. 7. pp. 943–947, 1999.

[233] C. Chen, H. Li, and M. E. Davis, "Studies on mesoporous materials I . Synthesis and characterization of MCM-41," *Microporous Mater.*, vol. 2, pp. 17–26, 1993.

[234] J. M. Kim and R. Ryoo, "Disintegration of mesoporous structures of MCM-41 and MCM-48 in water," *Bulletin of the Korean Chemical Society*, vol. 17, no. 1. pp. 66–68, 1996.

[235] D. E. J. G. J. Dolmans, D. Fukumura, and R. K. Jain, "Photodynamic therapy for cancer," *Nat. Rev. Cancer*, vol. 3, no. 5, pp. 380–387, 2003.

[236] J. L. Vivero-Escoto, R. C. Huxford-Phillips, and W. Lin, "Silica-based nanoprobes for biomedical imaging and theranostic applications," *Chem. Soc. Rev.*, vol. 41, no. 7, p. 2673, 2012.

[237] D.-E. Lee, H. Koo, I.-C. Sun, J. H. Ryu, K. Kim, and I. C. Kwon, "Multifunctional nanoparticles for multimodal imaging and theragnosis," *Chem. Soc. Rev.*, vol. 41, no. 7, pp. 2656–2672, 2012.

[238] H. K. Sajja, M. P. East, H. Mao, andrew Y. Wang, S. Nie, and L. Yang, "Development of Multifunctional Nanopaticles for Targeted Drug

Delivery and Non-invasive Imaging of Therapeutic Effect," *Curr. drug Discov. Technol.*, vol. 6, no. 1, pp. 43–51, 2009.

[239] Y. Wang, L. Dou, and H. He, "Multifunctional Nanoparticles as Nanocarrier for Vincristine Sulfate Delivery To Overcome Tumor Multidrug Resistance," *Mol. Pharm.*, vol. 11, no. 3, pp. 885–894, 2014.

[240] S. A. Corr, Y. P. Rakovich, and Y. K. Gun'ko, "Multifunctional Magnetic-fluorescent Nanocomposites for Biomedical Applications," *Nanoscale Res. Lett.*, vol. 3, no. 3, pp. 87–104, 2008.

[241] O. Chen, L. Riedemann, F. Etoc, H. Herrmann, M. Coppey, M. Barch, C. T. Farrar, J. Zhao, O. T. Bruns, H. Wei, P. Guo, J. Cui, R. Jensen, Y. Chen, D. K. Harris, J. M. Cordero, Z. Wang, A. Jasanoff, D. Fukumura, R. Reimer, M. Dahan, R. K. Jain, and M. G. Bawendi, "Magneto-Fluorescent Core-Shell Supernanoparticles," *Nat Commun*, vol. 5, no. 5093, pp. 1–16, 2012.

[242] G. Wang, X. Zhang, Y. Liu, Z. Hu, X. Mei, and K. Uvdal, "Magneto-fluorescent nanoparticles with high-intensity NIR emission, T_1 - and T_2 - weighted MR for multimodal specific tumor imaging," *J. Mater. Chem. B*, vol. 3, no. 15, pp. 3072–3080, 2015.

[243] M. Gogoi and P. Deb, "Magneto-fluorescent hybrid of dye and SPION with ordered and radially distributed porous structures," *Appl. Surf. Sci.*, vol. 298, pp. 130–136, 2014.

[244] H. M. Kim, H. Lee, K. S. Hong, M. Y. Cho, M. Sung, H. Poo, and Y. T. Lim, "Synthesis and High Performance of Magneto fluorescent Polyelectrolyte Nanocomposites as MR / Near-Infrared Multimodal Cellular Imaging," *ACS Nano*, vol. 5, no. 10, pp. 8230–8240, 2011.

[245] S. Van Cleuvenbergen, G. Hennrich, P. Willot, G. Koeckelberghs, K. Clays, T. Verbiest, and M. A. van der Veen, "All Optical Determination of Microscopic and Macroscopic Structure of Chiral, Polar Microcrystals from Achiral, Nonpolar Molecules," *J. Phys. Chem. C*, vol. 116, no. 22, pp. 12219–12225, Jun. 2012.

[246] F. Helmchen and W. Denk, "Deep tissue two-photon microscopy," *Nat. Methods*, vol. 2, no. 12, pp. 932–940, 2005.

[247] R. C. Johnson, J. Li, J. T. Hupp, and G. C. Schatz, "Hyper-Rayleigh scattering studies of silver, copper, and platinum nanoparticle suspensions," *Chem. Phys. Lett.*, vol. 356, no. 5–6, pp. 534–540, 2002.

[248] F. W. Vance, B. I. Lemon, and J. T. Hupp, “Enormous Hyper-Rayleigh Scattering from Nanocrystalline Gold Particle Suspensions,” *J. Phys. Chem. B*, vol. 102, no. 50, pp. 10091–10093, 1998.

[249] S. Knoppe, M. Vanbel, S. van Cleuvenbergen, L. Vanpraet, T. Bürgi, and T. Verbiest, “Nonlinear Optical Properties of Thiolate-Protected Gold Clusters,” *J. Phys. Chem. C*, vol. 119, no. 11, pp. 6221–6226, 2015.

[250] A. Horneber, K. Braun, J. Rogalski, P. Leiderer, A. J. Meixner, and D. Zhang, “Nonlinear optical imaging of single plasmonic nanoparticles with 30 nm resolution,” *Phys. Chem. Chem. Phys.*, vol. 17, no. 33, pp. 21288–21293, 2015.

[251] Y. El Harfouch, E. Benichou, F. Bertorelle, I. Russier-Antoine, C. Jonin, N. Lascoux, and P.-F. Brevet, “Hyper-Rayleigh Scattering from Gold Nanorods,” *J. Phys. Chem. C*, vol. 118, no. 1, pp. 609–616, 2014.

[252] K. Das, A. Uppal, R. K. Saini, G. K. Varshney, P. Mondal, and P. K. Gupta, “Hyper-Rayleigh scattering from gold nanoparticles: effect of size and shape.,” *Spectrochim. Acta. A. Mol. Biomol. Spectrosc.*, vol. 128, pp. 398–402, 2014.

[253] K. Sanusi, J. M. Stone, and T. Nyokong, “Nonlinear optical behaviour of indium-phthalocyanine tethered to magnetite or silica nanoparticles,” *New J. Chem.*, vol. 39, pp. 1665–1677, 2015.

[254] R. F. Kubin and A. N. Fletcher, “Fluorescence quantum yields of some rhodamine dyes,” *J. Lumin.*, vol. 27, no. 4, pp. 455–462, 1982.

[255] A. Manciulea, A. Baker, and J. R. Lead, “A fluorescence quenching study of the interaction of Suwannee River fulvic acid with iron oxide nanoparticles,” *Chemosphere*, vol. 76, no. 8, pp. 1023–1027, 2009.

[256] C. J. Yu, S. M. Wu, and W. L. Tseng, “Magnetite nanoparticle-induced fluorescence quenching of adenosine triphosphate - BODIPY conjugates: Application to adenosine triphosphate and pyrophosphate sensing,” *Anal. Chem.*, vol. 85, pp. 8559–8565, 2013.

[257] K. Sathiyamoorthy, C. Vijayan, and S. Varma, “Nonlinear Optical Response of Chloroaluminiumphthalocyanine Encapsulated by Silica Core−Shell Particles,” *Langmuir*, vol. 24, no. 14, pp. 7485–7491, 2008.

[258] E. Hendrickx, K. Clays, and A. Persoons, “Hyper-Rayleigh Scattering in Isotropic Solution,” *Acc. Chem. Res.*, vol. 31, no. 10, pp. 675–683, 1998.

[259] K. Clays and A. Persoons, “Hyper-Rayleigh scattering in solution,” *Phys. Rev. Lett.*, vol. 66, no. 23, pp. 2980–2983, 1991.

[260] P. C. Ray and P. K. Das, “Ka Values of Weak Organic Acids in Protic Solvents Obtained from Their First Hyperpolarizabilities in Solution,” *J. Phys. Chem.*, vol. 99, no. 51, pp. 17891–17895, 1995.

[261] C. R. Moylan, R. J. Twieg, V. Y. Lee, S. A. Swanson, K. M. Betterton, and R. D. Miller, “Nonlinear optical chromophores with large hyperpolarizabilities and enhanced thermal stabilities,” *J. Am. Chem. Soc.*, vol. 115, no. 26, pp. 12599–12600, 1993.

[262] S. Barlow and S. R. Marder, “Nonlinear Optical Properties of Organic Materials: Syntheses, Strategies and Applications,” in *Functional Organic Materials*, T. J. J. Mller and U. H. F. Bunz, Eds. Weinheim, Germany: Wiley-VCH Verlag GmbH & Co. KGaA, 2006, pp. 393–437.

[263] H. Ma, S. Liu, J. Luo, S. Suresh, L. Liu, S. H. Kang, M. Haller, T. Sassa, L. R. Dalton, and A. K.-Y. Jen, “Highly efficient and thermally stable electro-optical dendrimers for photonics,” *Adv. Funct. Mater.*, vol. 12, no. 9, pp. 565–574, 2002.

[264] F. Kajzar and J. Messier, “Third-harmonic generation in liquids,” *Phys. Rev. A*, vol. 32, no. 4, pp. 2352–2363, 1985.

[265] S. R. Marder, W. E. Torruellas, M. Blanchard-Desce, V. Ricci, G. I. Stegeman, S. Gilmour, J. L. Brédas, J. Li, G. U. Bublitz, and S. G. Boxer, “Large molecular third-order optical nonlinearities in polarized carotenoids,” *Science*, vol. 276, no. 5316, pp. 1233–1236, 1997.

[266] Y. Matsuzaki, M. Nakano, K. Yamaguch, K. Tanaka, and T. Yamabe, “Second hyperpolarizabilities of π-conjugated silicon-ring polymers,” *Synth. Met.*, vol. 71, pp. 1737–1738, 1995.

[267] T. Jafari, A. Simchi, and N. Khakpash, “Synthesis and cytotoxicity assessment of superparamagnetic iron-gold core-shell nanoparticles coated with polyglycerol,” *J. Colloid Interface Sci.*, vol. 345, no. 1, pp. 64–71, 2010.

Health, safety and environment

Regarding the experiments related to this dissertation, all health and safety guidelines and regulations from the HSE department of the KU Leuven were obeyed. All personal protection (gloves, (laser) safety goggles, lab coat,…) are mandatory. Risk analyses and proper waste management were evaluated before every experiment and were submitted to the appropriate channels.

It is highly recommended to follow MSDS (material safety data sheet) before setting up any lab experiment. All unattended experiments were considered carefully and needed to be approved by HSE department beforehand.

Following HSE department, there are 4 risk types of danger: E4 (very dangerous), E3 (dangerous), E2 (moderately dangerous) and E1.

There are some toxic solvents used in the experiments, such as CHCl3 (E4), toluene, ethanol, ethyl acetate (E3). Besides, most of substances are classified as E2 (THPC, TEOS) and there is only $HAuCl_4.3H_2O$ that is classified as E3. $HAuCl_4.3H_2O$ may cause severe skin burns and eye damage and may cause an allergic skin reaction.

About the toxicity of NPs, although there are some studies about the toxicity of particular NPs reported, the studies are not complete [165], [267]. Moreover, the toxicity of NPs also depends on their functionalization. However, in general, iron oxide, gold and silica NPs are considered as less toxic and biocompatible. For the storage, the particles were kept in suspension to minimize exposure.

List of publications

Articles in internationally reviewed academic journal

2. **T.T. Luong**, S. Knoppe, M. Bloemen, W. Brullot, R. Strobbe, J. Locquet, et al., Magnetothermal release of payload from iron oxide / silica drug delivery Agents, J. Magn. Magn. Mater. Vol. 416 (2016) 194-199. vol. 345, no. 1, pp. 6

   doi:10.1016/j.jmmm.2016.04.081.

1. M. Bloemen, W. Brullot, **T.T. Luong**, N. Geukens, A. Gils, T. Verbiest, Improved functionalization of oleic acid-coated iron oxide nanoparticles for biomedical applications, J. Nanopart. Res. 14 (2012) 1100-1109.

   doi:10.1007/s11051-012-1100-5.

Meeting abstracts, presented at international scientific conferences and symposia, published or not published in proceedings or journals

1. **T.T. Luong**, M. Bloemen, S. Knoppe and T. Verbiest, Synthesis of multifunctional Fe_3O_4-mesoporous SiO_2-Au core-shell nanoparticles, in 5^{th} International conference on Advanced Nanomaterials (ANM2014), (Aveiro, Portugal) (2014)